Experimental Studies of Damping in Microresonators using Laser Doppler Vibrometry

Ottoleo Kuter-Arnebeck

Department of Mechanical Engineering

McGill University, Montreal

August 2015

A thesis submitted to McGill University in partial fulfillment of the requirements of the degree of Doctor of Philosophy

Dedication

The thesis is dedicated to numerous people and places and things. Each, as an individual, has contributed inspiration, motivation, advice, energy, and friendship. Added all together, they have brightened and warmed my spirit and body like the sun shines on earth.

Of the places and things, I am grateful to be living on an island in a clean and beautiful river where we can swim in the summer and skate in the winter and, at any other time, simply sit and listen. A big thank you to the city around the little mountain, with all of its ice rinks, where I learned how to play hockey again. Nothing makes you feel alive and very much like Canada itself as passing the puck around when it is thirty below and dark out already at five o'clock.

Of the people, first I must thank my parents, specifically, for their continued support and encouragement and food and love. I also thank Marlee Parsons for more of the same and for teaching me about Canada and taking me to the Maritimes and Newfoundland. And an immense thank you to Lowry Burgess who has encouraged and inspired me to think nano and interstellar and to Prof. McGaughey, also at CMU, who gave me the first opportunity to immerse myself in the sub-continuum workings of the world. My other nearest and dearest friends, you know who you are, and thank you too; all the good folks from the classic FDA015; Nabil Shalabi, my lunch partner at Atti; Surabhi Joshi, who kept me company through tedious experiments and helped with the arithmetic and analysis of noise; Mathieu is a pro at translation, thanks a million; Sankha Mukherjee, who was there for some fatiguing long days in the microfab. Speaking of which, the staff at the McGill Nanotools Microfab, Don Berry and John Li, provided me with excellent advice and opportunities to learn the practical nuances of microfabrication that are written in no book. Finally, a very special thank you is due to Prof. Vengallatore, who has generously offered me an opportunity to pursue an education at McGill University. Most importantly, Prof. Vengallatore has given his professional guidance with a remarkable patience and clarity. My experience with his tutelage has grown me into a critical thinker. Thank you.

Thank you all!

PERPETUA

the system lags behind
itself a victim of time
too many degrees of freedom
hold up in microscopic fleeting
heating in concert a rhythm
shaking the entire prism

Acknowledgements

Here I acknowledge, in no particular order, the assistance that I have received from colleagues and institutions.

Nabil Shalabi designed and constructed, for his Masters degree, the electrostatic-excitation system that is used to study the temperature dependence of damping in microcantilever beam resonators. He installed the system and assisted in the temperature calibration.

Guru Sosale designed the microcantilever beams that are used in this study as part of his PhD research. More importantly, he designed and built the first system to measure damping, which is referred to in his thesis as the base-excitation system.

Kaushik Das, for his PhD research, constructed a set of microcantilever beam resonators that I used to characterize the measurement of damping from the thermomechanical noise in Chapter 5. Additionally, his measurements of the damping for this set of specimens are used as a comparison to the damping I measured from the thermomechanical noise.

Surabhi Joshi assisted in making the measurements of thermomechanical noise and helped to analyze and sort the data.

Aleks Labuda wrote the MATLAB code to calculate the power spectral density using the Daniell method.

Sankha Mukherjee and I jointly fabricated a set of single-crystal silicon microcantilever beam resonators in the McGill Nanotools Microfab and he participated in the measurement of the initial damping of this set of cantilevers using the base excitation system.

Professor Luc Mongeau and Professor Damiano Pasini have loaned the OFV-5000 laser Doppler vibrometer.

Additionally, I acknowledge the financial support of Professor Srikar Vengallatore, McGill University, and the NSERC program of Canada.

Abstract

Damping is a fundamental property of vibrating mechanical systems. To enhance the performance limits and refine the characteristics of resonant micromechanical sensors and actuators, the engineering of a low-damped system is ideal. Despite efforts to measure damping mechanisms and processes, many open questions remain. The thesis contributes to the practical knowledge of damping behavior and the experimental methods of damping measurement. This thesis addresses two openings in the literature: (1) a calibrated measurement of the effect of temperature on the material damping of microcantilever beam resonators and (2) the characterization of the measurement of damping in microcantilever beams and thin film nano-membranes using the thermomechanical noise (TMN). Both of these objectives are accomplished by measuring the dynamics of the microresonator using laser Doppler vibrometry, a non-contact high precision interrogation tool.

A methodology to calibrate measurements of material damping to the fundamental thermoelastic damping (TED) limit has been established in previous research and used to measure the effect of microstructure and operating frequency on the material damping of aluminum, gold, and silver using a single-crystal silicon microcantilever beam substrate. In this thesis, that methodology is extended to elevated temperatures (20 ˚C to 150 ˚C) and implemented to study the temperature dependence of the material damping in single-crystal silicon and in ~48 nm thick nanocrystalline aluminum films. First, the temperature dependent material properties of single-crystal silicon are collected from the literature and are used to calibrate the measured damping of single-crystal silicon microcantilever beams to the TED limit. The results reveal that the damping of single-crystal silicon increases proportionally to the TED limit from room temperature up to 150 ˚C. Then, two specimens are coated with ~48 nm of aluminum by e-beam deposition. The damping of the bi-layer beam is compared to the bare silicon beam to measure the material damping of the aluminum film. As the temperature increases, the material damping of the aluminum increases, peaks at ~100 ˚C, and then starts to decrease.

Next, the thesis characterizes the method by which the damping is measured from the TMN. The use of TMN to measure the resonance frequency and stiffness of the microcantilever beams is well established, but the accuracy and precision of measurements of the damping from

the noise has not been evaluated. To address this open question, a systematic experimental and analysis protocol is presented to measure the TMN and extract the damping. The methodology is applied to a set of silicon-based microcantilever beams and the results are compared to the damping measured by the established free-decay technique. The comparison shows that the damping measured from the TMN suffers from precision errors as great as 25% for low-damped resonators ($Q > 10^5$). Finally, the established experimental protocols are extended to measure the damping of a 200 nm thick bi-layer membrane of aluminum and silicon-dioxide at room temperature and atmospheric pressure. This experiment demonstrates that the TMN can be used to measure the damping for the lower mode number resonance peaks of the nano-membrane resonator.

The contributions of this thesis establish practical guidelines to measure damping from the TMN at room temperature and up to 150 ˚C using the logarithmic decrement of free-decay. The thesis also contributes calibrated measurements of material damping in silicon and nanocrystalline aluminum thin films at elevated temperatures. These methods and measurements are readily applied to further studies as they are based on well-characterized microcantilever beam resonators, a model resonator system with many commercial and research applications.

Sommaire

L’amortissement est une propriété fondamentale des systèmes vibratoires. Comme l’amortissement est lié aux limites de performances et aux caractéristiques des capteurs micromécaniques résonants et des actuateurs, le développement de systèmes à faible amortissement est idéal. Malgré de vastes efforts pour mesurer les mécanismes et les procédés d’amortissement, de nombreuses questions restent ouvertes. La motivation principale de cette thèse est de contribuer à la connaissance pratique du comportement d'amortissement et les méthodes expérimentales de mesure d'amortissement. Cette thèse adresse deux ouvertures dans la littérature : (1) une mesure calibrée de d’effet de la température sur l’amortissement du matériau de résonateurs en poutre en porte-à-faux, et (2) la caractérisation de la mesure d’amortissement dans des poutres en porte-à-faux et dans des couches minces de membranes nanométriques, en utilisant le bruit thermomécanique (BTM). L’ensemble de ces objectifs sont réalisés en mesurant la dynamique de micro-résonateurs, grâce à la vibrométrie laser à Doppler, un équipement interrogatif sans contact de haute précision.

Dans des recherches précédentes, une méthodologie pour calibrer les mesures d'amortissement des matériaux à la limite fondamentale d'amortissement thermoélastique (ATE) a été mise en place, et est utilisée pour mesurer l'effet de la microstructure et de la fréquence de fonctionnement de matériaux d'amortissement tels que l'aluminium, l'or et l'argent en utilisant une micro-poutre en porte-à-faux avec un substrat en silicium monocristallin. Dans cette thèse, que la méthodologie est prolongée à des températures élevées (de 20 ° C à 150 ° C) et utilisée pour étudier la dépendance de la température des matériaux d'amortissement en silicium monocristallin et de films d'aluminium nanocristallin d’une épaisseur de ~ 48 nm. Tout d'abord, les propriétés du matériau dépendantes de la température du silicium monocristallin sont collectées de la littérature et sont utilisées pour calibrer la mesure d'amortissement de micro-poutre en porte-à-faux en silicium monocristallin jusqu'à la limite d’ATE. Les résultats révèlent que l'amortissement du silicium monocristallin augmente proportionnellement à la limite d’ATE de la température ambiante jusqu'à 150 ° C. Ensuite, deux échantillons sont revêtus d’une couche mince de ~ 48 nm d'aluminium grâce à la déposition par faisceau d'électrons. L'amortissement de la poutre à deux couches est comparé à la poutre de silicium seul pour mesurer l'amortissement

du film d'aluminium. Lorsque la température augmente, l'amortissement de l'aluminium croît, atteint un maximum à ~ 100 ˚C, puis on commence à diminuer.

Ensuite, la thèse caractérise la méthode par laquelle l'amortissement est mesuré à partir du BTM. L'utilisation du BTM pour mesurer la fréquence de résonance et la rigidité des micro-poutres en porte-à-faux est bien établie, mais l'exactitude et la précision des mesures d'amortissement à partir du bruit n'ont pas été évalués. Pour répondre à cette question ouverte, un protocole expérimental et d'analyse systématique est présenté pour mesurer le BTM et extraire l'amortissement. Cette méthodologie est appliquée à un ensemble de micro-poutres en porte-à-faux à base de silicium et les résultats sont comparés à l'amortissement mesuré par la technique de décomposition libre déjà établie. La comparaison montre que l'amortissement mesuré à partir du BTM souffre d'erreurs de précision aussi grande que 25% pour des résonateurs à faible amortissement ($Q > 10^5$). Enfin, les protocoles expérimentaux déjà établis sont étendus pour mesurer l'amortissement d'une membrane bicouche en aluminium et dioxyde de silicium d'une épaisseur de 200 nm à température et pression ambiante. Cette expérience démontre que le BTM peut être utilisé pour mesurer l'amortissement des pics de résonance pour le mode le plus faible du résonateur nano-membranaire.

Les contributions de cette thèse établissent des lignes directrices pratiques pour mesurer l'amortissement à partir du BTM de la température ambiante à 150 ° C en utilisant le décrément logarithmique de la méthode de décomposition-libre. Cette thèse contribue également à des mesures calibrées de matériaux d'amortissement en silicium et aluminium nanocristallin couches minces à hautes températures. Ces méthodes et ces mesures sont facilement applicables à d'autres études car elles sont basées sur des résonateurs de micro-poutres en porte-à-faux bien définis, ces systèmes modèles de résonateurs ont de nombreuses applications commerciales et de recherche.

List of abbreviations and symbols

Abbreviations

MEMS	Micro/nano electro-mechanical systems
AFM	Atomic force microscope
BC	Bragg cell
BES	Base excitation system
BOX	Buried oxide
BS	Beam splitter
CDS	Capacitive displacement sensor
CSO	Carrier signal oscillator
CVD	Chemical vapor deposition
DC	Direct current
DI	De-ionized
DSP	Digital signal processing
DRIE	Deep reactive ion etching
EDA	Exploratory data analysis
EES	Electrostatic excitation system
HFB	High-frequency microcantilever beam
HMDS	Hexamethyldisilazane
IF	Intermediate frequency
L	Lens
LDV	Laser Doppler vibrometer
LFB	Low-frequency microcantilever beam

M	Mirror
OB	Objective beam
PBS	Polarized beam splitter
PD	Photo-detector
PSD	Power spectral density
QWP	Quarter-wave plate
RB	Reference beam
RIE	Reactive ion etching
SOI	Silicon-on-insulator
TED	Thermoelastic damping
TMAH	Tetra methyl ammonium hydroxide
TMN	Thermomechanical noise
UV	Ultraviolet

Latin Symbols

a	Integer representing multiples of $\lambda/4$
A	Cross-section area
A_1, B_1,	Fitting parameter for the white-noise baseline
A_2, B_2,	Fitting parameter for the peak amplitude of a Lorentzian curve
B_n	Euler-Bernoulli beam mode shape function
c	Damping
C_v	Specific heat per unit volume
d	Distance between the microcantilever beam and the counterelectrode plate
E	Young's modulus

f	Frequency in Hz
f_{alias}	Aliased frequency
f_c	Carrier frequency
f_{DM}	Down-mixed frequency
f_n	Resonance frequency in units of Hertz
f_o	Initial frequency
f_R	Reference frequency
f_s	Sampling frequency
f_T	True value of the resonance frequency
f_{vib}	Target vibration frequency
$f_{1,\delta}$	First mode resonance frequency measured from the logarithmic decrement
$f_{2,\delta}$	Second mode resonance frequency measured from the logarithmic decrement
F_{th}	Thermal force
$G(f)$	Mechanical admittance
H	Normalized electrostatic load
h	Thickness
h_b	Thickness of the microcantilever support
I	Area moment of inertia
J	Linear slope
k	Thermal conductivity
k_B	Boltzmann constant
K	Spring constant
K^*	Complex spring stiffness

L	Length
m,n	Membrane mode shape indices
M	Mass
N	Integer
P	Electrostatic force
Q	Quality factor
Q_T	True value of the quality factor
$\Re$	Real part of a complex function
r	Number of cycles
SD	Standard deviation
$S_y(f)$	Power spectral density of the displacement
$S_v(f)$	Power spectral density of the velocity
t	Time
$\mathcal{T}$	Measurement duration
T_o	Equilibrium temperature
u_c	Heterodyne Doppler signal as the photodetector current
U_c	Amplitude of the heterodyne Doppler signal as the photodetector current
u_i	In-phase quadrature signal
U_i	Magnitude of the in-phase quadrature signal
u_q	Quadrature signal
U_q	Magnitude of the quadrature signal
V_{AC}	Alternating current voltage
V_{LDV}	Velocity in units of volts

V_{PI}	Pull-in voltage
v_s	Speed of sound
$v(t)$	Velocity as a function of time
W	Stored elastic energy per cycle of vibration
w	Width
x	Axial position
$Y(f)$	Fourier transform of the displacement
$y(t)$	Displacement as a function of time
Y_x	Deflection of the cantilever as a function of axial position

Greek symbols

α	Coefficient of linear thermal expansion
β_n	Euler-Bernoulli beam mode shape constant
γ	Grüneisen parameter
Δ	Normalized deflection at the tip of a microcantilever beam
Δf	Frequency modulation
ΔH	Activation energy
$\Delta\phi$	Phase modulation
ΔW	Energy lost per cycle of vibration
δ	Logarithmic decrement
δ_c	Logarithmic decrement of a the bi-layer microcantilever beam
$\delta_{residual}$	Logarithmic decrement due to the background damping
δ_s	Logarithmic decrement of a single-crystal silicon resonator
$\delta_{s,1}$	Logarithmic decrement of a single-crystal silicon resonator measured at the first mode

$\delta_{s,2}$	Logarithmic decrement of a single-crystal silicon resonator measured at the second mode
δ_{TED}	Logarithmic decrement due to thermoelastic damping
ε_{me}	Measurement error
ε_o	Vacuum permittivity
ε_r	Dielectric constant
ε_{xx}	Longitudinal strain
$\varepsilon_{xx\ max}$	Maximum longitudinal strain
ζ	Damping ratio
η	Loss factor
Θ	Conversion factor of volts to velocity for the OFV-5000
Λ	Averaging factor
λ	Wave length
λ_n	Euler-Bernoulli beam mode shape constant
λ_1	Euler-Bernoulli beam mode shape constant, first mode resonance
λ_2	Euler-Bernoulli beam mode shape constant, second mode resonance
ν	Poisson ratio
Ξ	Relaxation strength
ρ	Density
σ	Longitudinal stress
τ	Relaxation time
ϕ	Phase
ϕ_m	Phase modulated by the Doppler signal
ϕ_w	Wrapped phase

φ	Loss angle
φ_n	Euler-Bernoulli beam mode shape function
Ψ	Specific damping capacity
ψ	Euler-Bernoulli beam mode shape constant
Ω	Normalized frequency
ω	Angular frequency
ω_d	Damped resonance frequency
ω_n	Resonance frequency

Table of Contents

List of Tables

List of Figures

CHAPTER 1

Introduction to damping in micro/nanomechanical resonators

This chapter introduces the role of damping in the performance of instruments based on micromechanical resonators and identifies open areas of research. Then a review of damping mechanisms is followed with the measures and measurement methods of damping. The chapter closes with an outline of the rest of the thesis.

1.1 Introduction to micro/nanomechanical resonators and the role of damping

Since the invention of the transistor and the rise of the computer, the drive to increase the density of electrical elements for computer chips has led to the rapid development of new micro and nano machining techniques. The turnover of fabrication methods and tools for the production of integrated circuits has resulted in the migration of surplus technology from industrial micro/nano-fabrication facilities to university laboratories. Access to state-of-the art microfabrication technologies is feeding a new industrial revolution. The capacity for a small research group to develop new devices and concepts to exploit unique physical phenomena at the micro/nano scale is spurring scientific inquiry as well as industrial innovation [1, 2].

Still in its nascence, the applications and functionality of micro/nano-electromechanical systems (MEMS) are expanding. In particular, the use of resonant MEMS devices for sensing and detecting applications is receiving considerable attention and development [3, 4]. Their capacity to extend the perceptible range of forces to unprecedented levels are enabling new discoveries and capabilities in fields as diverse as biology, chemistry, quantum mechanics, and navigation [5-8].

One of the most significant resonant MEMS based tools to-date is the atomic force microscope (AFM). The AFM consists of a micromachined silicon cantilever with a sharp tip on the end, a laser, and a photodiode sensor. The dynamics of the microcantilever beam are detected by the reflection of a laser aimed at the end of the cantilever and collected in the photodiode array. The microcantilever is driven at its fundamental resonance frequency and the

tip of the microcantilever is rastered over the surface of the specimen. The interaction between the surface and the sharp tip shifts the frequency of the vibration [9]. The frequency shift is then transduced into a topographic image of the surface.

The AFM operates on the principle of force detection. The ultimate performance limit is the signal-to-noise ratio that is determined by the mechanical noise floor and the detection signal noise [10-13]. The mechanical noise floor is defined by the thermomechanical noise (TMN), which is a stochastic vibration that is caused by ambient thermal energy and, paradoxically, the vibration energy dissipation [9, 14, 15]. The detection signal noise is generated in the optics configuration and may be caused by weak signal intensity or detection errors due to light scattering on an imperfect surface [16]. Unlike the mechanical noise, the optical noise can be easily improved; it is not uncommon to add a thin film of metal (aluminum, silver, gold, chrome) to improve reflectivity [17]. However, the addition of a metal coating increases the dissipation by as much as an order of magnitude [18-21]. The increase in energy dissipation affects the measurement resolution of the frequency shifts and also amplifies the TMN floor [9, 13, 22]. Achieving a state of minimal dissipation, then, is critical for the basic performance of the tool. Energy dissipation is important from the perspective of precision measurements; the magnitude of the damping, a measurement of the dissipation, must be known in order to quote the accuracy and resolution of the measurement.

However, an estimate of the damping goes beyond an initial calibration. In many applications, resonators are operated in non-ideal conditions where temperature fluctuations are common. For instance, the AFM has been re-engineered as a nanolithography tool where the cantilever stylus is heated and is used to burn nano lines into the lithography resist while simultaneously imaging the surface [22-25]. The changes in temperature alter the dissipation, which affects the cantilever amplitude response [26]. Furthermore, the resonance frequency is a function of the dissipation and the temperature [27, 28]. Thus it is not just the imaging resolution that is affected, but also the control of the dynamics [29]. Compensating for these deleterious effects can be achieved by in-situ measurement of the damping. One simple method to achieve this measurement is to exploit the link between the dissipation and the TMN, a technique that is often used to calibrate the damping and frequency of microcantilever beams for the AFM [30, 31].

Consequently, there are open questions that pertain not just to the damping mechanisms but to the techniques of damping measurement. Specifically, two questions are brought to attention: (1) what is the temperature dependence on the mechanisms of material damping and (2) what is the accuracy and precision of the damping measured from the TMN. These issues are also relevant for many other resonance based micromechanical systems such as radio frequency transducers and filters, accelerometers, and nano-scale mass balances where the measurement precision and temperature stability are important [5, 12, 32-34]. Answering the open questions will help refine and expand the capabilities and roles of resonant MEMS based sensors, detectors, actuators, and energy harvesters. The aim of the thesis is to contribute practical knowledge of certain damping mechanisms and measurement techniques to the existing body of knowledge.

Damping has been studied extensively for many decades with the goal of building a catalog of experimentally proven theoretical models and methods to control damping. However, experts in this pursuit acknowledge that an all encompassing description of energy loss is not currently available [35-37]. Segregating the many damping mechanisms for a systematic experimental analysis is difficult [38]. Numerous variables, such as the operating frequency, vibration mode, and amplitude; the geometry, chemistry, material properties, and material defects; the operating environment and structure of the device boundaries, are significant for multiple damping mechanisms [36]. Furthermore, the variability of resonator configurations, materials, vibration modes, and the experimental methods employed in the study of damping make it difficult to quantitatively compare reported results [38]. The study of damping calls for a systematic methodology where each of the mechanisms is minimized by careful design. To implement this properly, a working knowledge of the various sources of damping is necessary.

1.2 Mechanisms of damping

The damping that affects MEMS resonators can be classified into three categories: *material damping, fluid-structure interactions,* and *boundary damping*. Table 1-1 lists the mechanisms that apply to each category and the relevant literature that discuss each mechanism.

Table 1-1: Classification of damping mechanisms and relevant literature from Joshi *et al*. [36].

Boundary damping		**Fluid-structure interactions**		**Material damping**	
Elastic wave radiation	[39-58]	Viscous damping	[59-61]	Thermoelastic damping	[62-77]
Microsliding	[78-81]	Squeeze-film damping	[82, 83]	Phonon-phonon interactions	[84-86]
Viscoelasticity	[87]	Acoustic radiation	[88]	Phonon-electron interactions	[86, 89]
		Internal flow	[90, 91]	Internal friction	[92-105]

The most relevant mechanisms are discussed in the following sub-sections in terms of their effects on flexural beam resonators, though they apply to most configurations of flexural mode resonators. Then in Section 1.3, the methodology to measure the contribution of individual damping mechanisms is explained.

1.2.1 Boundary damping

Boundary damping is also known as anchor loss and, as the name implies, originates from the mounting conditions of the resonator. The main contribution to damping from the boundary conditions of the microcantilever specimens has two sources: support loss and microsliding [36]. Support loss has been well studied and theoretical models proposed [106]. On the other hand, microsliding, more commonly referred to as clamping loss has not been well characterized.

Clamping loss is a source of damping relevant for resonators that are attached to a supporting structure via a vice-like clamping arrangement, which is typically used for cantilever beams. This type of loss is a combination of static and dynamic friction. At the microscale, the surfaces of the beam and the clamp are rough. The roughness coupled with the pressure applied by the clamp exerts an amount of static friction on the beam [79]. When the beam oscillates, the strain field at the clamped surfaces of the beam must overcome the adherence of the static

friction. Once this adherence is broken, the tangential friction continues to sap energy and generate heat [79]. The two stages of the clamping loss give rise to the name "slip-stick" friction or microsliding. A theoretical description of microsliding is elusive due to the variety of custom clamping arrangements [17].

The other mechanism of boundary damping, support loss, has been studied by numerical methods and simulations to develop analytical models. Two phenomena have been identified that contribute to support loss: (1) the generation and radiation of elastic waves at the junction of the resonator to the larger supporting structure [39-42, 45, 106] and (2) the ballistic transport of phonons from the resonator into the support [56-58]. The damping due to the radiation of elastic waves is determined by the ratio of the thickness of the supporting structure and the length of the resonator to the width and the thickness of the resonator [106]. The damping of the latter mechanism is a function of the elastic modulus, density, and resonance frequency of the resonator and the stress generated at the junction to the support [57, 58].

From the description of these two avenues of anchor loss, the practical strategy to control boundary damping is evident. To reduce the clamping loss, the movement of the resonator at the clamped surfaces should be minimized. In the case of a cantilever, this involves moving the oscillating strain field away from the clamped portion of the beam [79]. Various geometries have been experimentally shown to accomplish this, including tuning fork cantilevers [78], notched beams [107], tapered beams [108], and featuring a filleted transition from the beam to the clamped portion [11, 109, 110]. To reduce the support loss, the approach is to maximize the size of the base with respect to the beam portion of the cantilever. For a vice-like clamping arrangement, the clamp is considered to extend the area of the cantilever base and further reduces support loss. Alternatively, a supporting arrangements that holds the beam at the nodes, called "free-free support," significantly reduces the boundary damping [46, 58]. Other attachment configurations such as phononic crystal strips, [54, 55, 111], and abrupt junctions, [51], have been demonstrated to reduce the radiation of elastic waves to the support.

1.2.2 Fluid-structure interactions

Fluid-structure interactions can be a significant source of damping for all flexural mode resonators [112]. The fluid medium damps the vibration in several ways. Energy is lost to the environment when the elastic energy is converted to acoustic radiation [88, 113]. Another source of loss is the drag force exerted by the fluid medium on the resonator [59]. Finally, squeeze-film damping can affect flexural resonators that are operated within close proximity to a solid surface [112]. In this case, the film of air that is trapped between the resonator and the surface causes inertial and viscous forces to dampen the vibration [82]. Loss due to fluid-structure interactions can be eliminated by operating in a reduced pressure environment.

1.2.3 Material damping

Material damping sets the minimum energy dissipation levels for flexural mode resonators. With regards to this, understanding the mechanisms is crucial so that appropriate designs can be implemented to minimize their impact. The major sources are internal friction, thermoelastic damping (TED), and Akhiezer damping. Each will be discussed in turn.

Internal Friction

Internal friction is a relaxation mechanism that originates within the microstructure of the material. Most notably, the internal friction is induced by material defects, such as point defects and friction at microcrystal grain boundaries [94, 114, 115]. Internal friction may also be caused by doping, a common practice of adding interstitial atoms, usually boron or antimony, to alter the electrical properties of semi-conductor materials [116]. In thin metal films, internal friction has been shown to have an anelastic behavior [93]. In this case, the internal friction processes is temperature and frequency dependent [114]. Separating the specific mechanisms of internal friction has proved to be a difficult process. Reducing the impact of defect induced internal friction is accomplished by using high-purity single-crystal materials for the construction of low-damping microresonators [17].

Thermoelastic damping

Thermoelastic damping is a specific form of internal friction that arises from the application of cyclical stress gradients [117]. When a beam is bent, the thermoelastic effect generates a temperature gradient across the thickness [65]. This temperature gradient will cause irreversible heat conduction, entropy generation, and energy dissipation [64, 67]. The magnitude of TED is frequency dependent and has a characteristic Debye peak defined by the relaxation time and resonance frequency of the resonator [63]. Poly-crystalline materials exhibit two TED damping peaks due to intracrystalline relaxation [72]. Thus, TED can be reduced by using high-purity materials and appropriately designing the resonance frequency with respect to the relaxation time. Another method to reduce the TED is to interrupt the transverse heat conduction with slots or channels [73, 74, 118].

Akhiezer damping

Akhiezer damping is a fundamental damping mechanism originating in the transport of thermal energy via phonons. The stress field of a transversely vibrating beam modulates the frequency of the thermal phonons, which is measured by the Grüneisen parameter, γ [84, 119]. The temperature differences between different phonon modes then cause an intramode heat flow and entropy generation [85]. The frequency dependence of Akhiezer damping is of a similar form as TED, and thus can be reduced by engineering the dimensions of the microresonator appropriately [17, 67, 69, 74, 84].

1.3 Measurement of damping

The process by which kinetic and potential mechanical energy is converted to disordered thermal energy in a structure that is subject to a vibration is referred to as dissipation. Dissipation is quantified by the specific damping capacity, $\Psi = (\Delta W/W)$, and the loss factor, $\eta = (\Delta W/2\pi W)$, where ΔW is the energy lost per cycle of vibration and W is the stored elastic energy. However, dissipation cannot be measured directly. The magnitude of the energy loss is quantified by the effect of dissipation on the dynamics; the *damping* of vibrations due to the dissipation is used to quantify the energy that is lost. Various methods have been implemented to measure the damping and, thus, there are different measures of damping [120]. These

measures and measurement techniques for the analysis of damping are discussed in the following sub-sections.

1.3.1 Measures of damping

There are three models for linear damping: (1) the viscous damping model, (2) the complex spring model, and (3) the standard anelastic solid [36]. The viscous damping model assumes that the damping force is proportional to the velocity of the oscillation [121]. The complex spring model assumes that the damping has no frequency dependence and is determined by the material properties [122]. The standard anelastic solid has a linear stress-strain relationship where there exists an equilibrium strain for each stress state and the equilibrium response is delayed and exhibits a frequency dependence [94, 122].

The parameter for the viscous damping is the damping ratio, ζ, and the complex spring and standard anelastic solid damping may be described by the loss angle, φ. The experimental methods to obtain these measures of damping have introduced other measures of the energy loss that do not necessarily signify a particular form of damping. For instance, the steady state response of an oscillating system is analyzed to measure the loss angle, the loss factor, and also the inverse quality factor, Q^{-1} , while the transient response yields the damping ratio and the logarithmic decrement, δ [121, 122].

The relationship between these measures of damping is given by [121, 123]

$$\tan\varphi = \eta = Q^{-1} = 2\zeta = \frac{\delta}{\pi} = \frac{\Delta W}{2\pi W} = \frac{\Psi}{2\pi}. \tag{1.2}$$

This relationship is only approximate for linear damping and in the case of low-damping values with $\varphi < 0.01$ [94]. The equivalence of the damping terms allow the experimentally measured damping to be compared for a variety of measurement techniques.

1.3.2 Damping measurement techniques

Damping is measured by closely monitoring the dynamics of the resonator in the frequency or time domain [36]. Frequency domain analysis is applied to a system under steady state harmonic conditions while time domain analysis is made from a measurement of the transient response. From the harmonic response, the damping is measured by the hysteresis loop method, the magnification-factor method, and the bandwidth method [121]. The damping is measured from the transient response by the logarithmic decrement method and the step-response method [121]. Each of these damping measurement techniques will be described in turn.

Frequency domain analysis

The hysteresis loop is generated by the steady state response to an applied cyclic load [121]. The plot of the force against the response creates a characteristic elliptical shape which is analyzed to extract η. The frequency of the applied load can be shifted to observe the change in damping that would occur for certain forms of damping [122].

The magnification factor is also a measure of the steady state harmonic response. This damping measurement is made by plotting the frequency-response function of the system, which is the ratio of the frequency dependent response amplitude to the input force divided by the spring constant [121, 122]. The graph of the magnitude of the frequency response function plotted against the excitation frequency is analyzed to extract the damping in terms of the quality factor or damping ratio.

Similar to the magnification factor, the bandwidth method is a spectral analysis of the steady state response to a harmonic input. The response amplitude is plotted as a function of the excitation frequency and the damping is calculated from the ratio of the resonance frequency to the half-power bandwidth [121]. The damping measured by this method is quantified in terms of the quality factor, Q.

Transient response analysis (time domain)

The time domain analysis of damping is obtained from the response to an initial excitation. The step-response method measures the lag of the system response to a unit step input [121]. The time at which the peak response occurs is used to calculate the damping ratio [112]. Another method is to excite the resonator to some initial amplitude and let the vibration freely decay. The logarithmic decrement is measured from the rate of the decay [27, 123, 124].

1.3.3 Instrumentation

The measurement of damping requires a method of actuation and detection. Actuation may be applied by electrostatic excitation, dielectric excitation, piezoelectric excitation, magnetic excitation, or differential heating [24]. The vibration can be measured by capacitance, dielectric, magnetic, piezo, or optical detection [24]. The selection of the actuator and detection system is dependent on the method of damping measurement.

It is more critical to have a precise actuation system for the harmonic analysis damping measurements than for the transient response measurements. Applying a linear force over the broad range of operating frequencies that micromechanical resonators typically operate at can be challenging. Noise or non-linear excitation may cause systematic errors of the detection of the maximum response amplitude for harmonic analysis, especially for low-damping ($Q > 10^3$) [125]. Time domain analysis generates more data than harmonic analysis, thus the impact of excitation and measurement noise is less critical and may be filtered out [125]. Additionally, the damping is measured from the raw time-series data and does not require any mathematical transformations that analysis in the frequency domain requires. For these reason, the logarithmic decrement method is typically the method of choice for precision damping measurements of low-damped resonators.

Since the logarithmic decrement is measured from the free-decay of the vibration amplitude, accuracy and precision is more critical for the interrogation system than it is for the excitation system. Capacitance detection, dielectric detection, magnetic detection, and piezoelectric based detection are attractive because they can be manufactured in parallel with the resonator, thus reducing the size of the experimental system. However, these detection methods

are sensitive to the configuration of the resonator and vibration amplitude and are prone to amplitude non-linearity [126]. Optical detection techniques such as interferometers or angular position determination can achieve sub-nanometer displacement resolution over a broad frequency and amplitude range [16]. Of particular utility for the metrology of MEMS devices is high-precision laser Doppler vibrometry (LDV).

Laser Doppler vibrometry

The LDV is used to measure vibrations, either in the frequency domain or in absolute units of displacement and velocity, and in its utmost limits, this tool is capable of highly accurate measurements of oscillations with sub picometer resolution over a vibration bandwidth of many megahertz [127]. Additionally, the time series measurements are available in real time. Compared to other vibration measurement techniques, such as accelerometers, fiber-optic sensors, or capacitance based detection, the LDV typically has a greater linear range, accuracy, and precision.

Further distinguishing the LDV is the non-contact nature of the measurement. This allows for the interrogation of isolated structures such as the tops of bridges and micro/nano resonators [128]. In fact, this feature of the LDV was one of the main reasons for its development by Yeh and Cummins in 1964, where the initial application of the LDV was to measure local velocities in fluid flow [16, 129]. The power of the tool was then recognized for making high-precision vibration measurements on small and fragile structures. Since the 1980s, the demands of the ever evolving micro/nano industry have pushed the development of LDV technology to improve the resolution, accuracy, and capabilities.

Due to its non-contact interrogation with microscopic laser spot sizes and the linear, large measurement bandwidth, the LDV is a proven interrogation instrument for the measurement of damping in micromechanical resonators. The relevant literature can be categorized according to the measurement method and type of resonator.

- Harmonic Analysis
    - Forced Excitation
        - Flexural mode resonators: [38, 41, 52, 58, 81, 130-136]

        - Membrane resonators: [44, 137-139]
    - Thermomechanical Noise
        - Flexural mode resonators: [103, 134, 140, 141]
- Free-decay analysis, flexural mode resonators
    - Room Temperature: [10, 58, 81, 102, 113, 131, 142-144]
    - Temperature Dependence: [21, 22, 96, 145]

This thesis aims to use the LDV to study the dynamics of silicon based resonators and further, in Chapter 5, evaluate the use of the LDV as a standalone platform to directly measure the damping from measurements of the noise. In this application, the accuracy, precision, and low-noise of the LDV is essential.

1.4 Open questions

Significant progress has been made over the past three decades on the measurement and analysis of damping in miniaturized mechanical resonators. Nevertheless, many important and interesting questions remain largely unexplored. In this thesis, the focus is on the following two questions:

- What are the effects of temperature on material damping in micro/nano resonators?

The measurement of material damping is challenging because all other sources of dissipation (boundary damping and fluid structure interactions) have to be eliminated. In previous work by my colleagues at the Laboratory for Micro/Nano Systems at McGill University, an approach has been developed to tackle this problem by using the fundamental limit of TED to calibrate the measurement of material damping [18, 97, 98, 146, 147]. This methodology has been implemented to measure the frequency dependence of material damping in silicon, gold, aluminum, and silver at room temperature. However, the extension of this approach to elevated temperatures (20 ˚C to 150 ˚C) has not yet been attained.

- Can thermomechanical noise be used for precision measurement of damping in micro and nanomechanical resonators?

In the introduction, the importance of damping was illustrated in terms of the mechanical noise floor, which is defined by the TMN [148]. The link between the two may be exploited to measure the damping from an observation of the mechanical noise. Thermomechanical noise has been explored experimentally [30, 31, 140, 149-156] and theoretically [9, 12, 14, 15, 157-161] for some decades. Focus has been centered on creating working models for low-noise design in sensing applications and for finding the stiffness of microcantilever resonators by the thermal tuning method [30, 152-155, 160, 162, 163]. In the thermal tuning process, a model is fit to the experimentally measured TMN, and the area under the resonance peak is applied to calculate the cantilever stiffness [159]. While the damping is not the main interest for this application, it has been extracted from this methodology in the process [30, 31, 150, 151, 162, 164]. However, the accuracy and precision of the damping extracted from a measurement of the TMN has not yet been thoroughly characterized.

1.5 Objectives of the thesis

The study of material damping at elevated temperatures:

- Establish experimental techniques and protocols for measuring the temperature dependence of material damping in microcantilever beam resonators.
- Apply the techniques to measure material damping in two model systems (namely, single-crystal silicon and nanocrystalline aluminum thin films) at temperatures ranging from 20 ˚C to 150 ˚C.

The measurement of damping from the thermomechanical noise:

- Establish experimental techniques and protocols for measuring damping using thermomechanical noise.
- Determine the accuracy and precision of this method of damping measurement with respect to an independent well-established technique.
- Demonstrate the utility of the established methodology by measuring damping in single-crystal silicon microcantilever beams in vacuum and silicon nitride nanomembranes at atmospheric pressure.

1.6 Organization of the thesis

This chapter introduced micromechanical resonators and the importance of damping in terms of device performance and dynamics. Then the applicable damping mechanisms were discussed and the methods of measurement described. Finally, the open questions and objectives of the thesis were introduced. The next chapters describe the aspects of the damping measurement system and its implementation to measure damping in single-crystal silicon microcantilevers, the internal friction of thin aluminum films, and thin-film membrane resonators.

In Chapter 2, the functions and characteristics of the LDV for the interrogation of the resonator specimens are discussed. In Chapter 3, the instrumentation of the system to measure damping of microcantilever resonators by a measurement of the free-decay of vibration is presented. The performance of this system is characterized and validated according to theoretical limits and measurements of damping obtained on a second, well-characterized damping measurement system. In Chapter 4, this damping measurement system is used to study the effect of temperature on the material damping of single-crystal microcantilevers and the internal friction of thin aluminum films. In Chapter 5, a subset of silicon-based microcantilevers is used to introduce and characterize the damping extracted from a measurement of the TMN. In Chapter 6, the TMN analysis tools are extended to measure the damping of a thin-film membrane resonator. Finally, in Chapter 7, the conclusions are framed and expanded to formulate suggested research opportunities based on the findings and observations of the thesis.

CHAPTER 2

Review of laser Doppler vibrometry

The objective of this chapter is to introduce the concepts of laser Doppler vibrometry from the perspective of measurement accuracy and precision. The detailed implementation of the interferometer and the signal decoder will be discussed in the following sections. Then the theoretical performance will be compared to the experimentally measured resolution for two commercially sourced LDV units. In terms of the actual performance of a commercially available LDV, its use for the measurement of noise and damping of resonant microcantilever beams will be demonstrated in the next chapters

2.1 Principle of operation

The basic configuration of a modern LDV system has two components: (1) the optics section and (2) the signal processing section. The optics section has changed little since the advent of the heterodyne interferometer in the 1960s. In this part of the LDV, a coherent light source is beamed at the target specimen and the reflection is imbued with a frequency shift (the Doppler effect), which is then combined with a reference beam. The interference pattern of the two beams contains the frequency and phase information of the oscillation. The Doppler signal is then demodulated in the signal processing chain to obtain the velocity or displacement in real time.

2.2 Implementation of the LDV

The LDV is comprised of an optics section and a signal processing section. The optics section includes the interferometer, the interrogated object, and any intervening mediums. The signal processing section is composed of the decoders and post-processing units.

2.2.1 The interferometer

The principle of the interferometer element of the LDV is to measure the vibration of some object using a focused laser beam. The velocity and displacement, $v(t)$ and $y(t)$, of the

target imbues the reflected light with a frequency and phase modulation, Δf and $\Delta\phi$ respectively, the Doppler effect,

$$\Delta f(t) = \frac{2v(t)}{\lambda} \tag{2.1}$$

and

$$\Delta\phi(t) = \frac{4\pi y(t)}{\lambda} \tag{2.2}$$

where λ is the wave length of the light. The signal cannot be demodulated directly because the frequency of light is very high with respect to the modulation [165]. Thus, the reflected wave front is combined with a reference beam of pure light and the interference reveals the Doppler signal. This is why the technique is known as interferometry.

Two types of interferometers are commonly used in vibrometry: the homodyne and the heterodyne interferometer. The homodyne interferometer, advantageously, directly supplies the Doppler signal in a quadrature format, which is a pre-requisite for digital signal processing (DSP) [165]. However, it can suffer from off-set and amplitude errors due to imperfect target reflectivity and has no direct-current (DC) component, which affects the accuracy of the demodulation of the Doppler signal [165]. In the heterodyne interferometer, the information content is defined by the phase modulation and does not depend on the amplitude of the signal [165]. Thus, it is the preferred interferometer for modern LDVs.

The laser source is the first component in the layout, in Figure 2.1, of the heterodyne interferometer. The wavelength and intensity of the laser light is chosen according to the measurement conditions, such as the target's scattering efficiency and the position and focal length of the optics [166]. The laser is passed through a polarized beam splitter (PBS1) and then takes two different paths. The object beam (OB) continues towards the target passing through another polarized beam splitter (PBS2), the objective lens (L) and a quarter-wave plate (QWP) before impinging on the target. The scattered light is then rotated 90 ° by the QWP and directed to the photo-detector (PD) by PBS2.

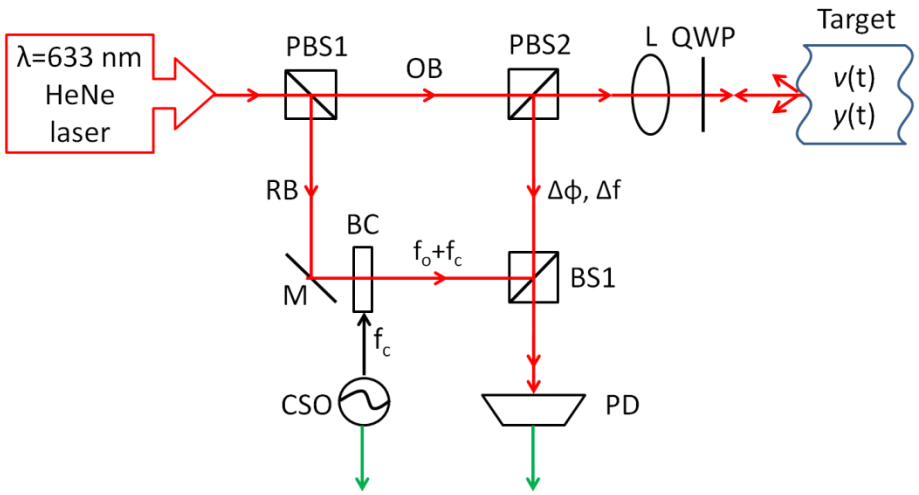

Figure 2.1: The layout of a Mach-Zehnder heterodyne interferometer. PBS1 and PBS2 are polarized beam splitters. The objective beam and reference beam are respectively labeled as OB and RB. M is a mirror, BC is a Bragg cell, L is a lens, QWP is a quarter wave plate, BS1 is a beam splitter, PD is a photodetector, and CSO is a carrier signal oscillator supplying the carrier signal f_c to the Bragg cell. Real implementations of this schema are varied [166].

While the OB is completing this circuit, the reference beam (RB) has been directed to a Bragg cell (BC) by a mirror (M). The BC is an acousto-optical component that shifts the initial frequency of the reference beam, f_o, by f_c, which is supplied by a digital carrier signal oscillator (CSO) [167]. The frequency shift is achieved by splitting the light with the acoustic waves in a crystal in a process analogous to using a rotating diffraction grating to split and shift the frequency of light by the Doppler effect [166]. The frequency of the BC must be greater than the bandwidth of the heterodyne signal, $f_{vib} + \Delta f$. Thus, the carrier frequency also determines the maximum measurable heterodyne frequency and the velocity range [168, 169].

The shifted reference beam is then recombined with the measurement beam at a beam splitter (BS1) and collected by the photo detector. The signal intensity is converted to voltage and the current of the photodetector output is expressed as

$$u_c = U_c cos[2\pi f_c t + \phi_m(t)], \tag{2.3}$$

where U_c is the magnitude of the current and ϕ_m is the modulated phase. If there is no motion of the target, then the signal is purely the BC carrier frequency. To extract the velocity and displacement of the target, the heterodyne signal is demodulated in the signal processing section of the LDV.

2.2.2 Decoding and signal processing

Analog decoding is achieved by phase locked loop, pulse density, or delay line demodulators to convert the Doppler frequency to a voltage that is proportional to the velocity [165]. The advantages of analog decoding are instantaneous readout and measurement bandwidth in the tens of megahertz and the disadvantages are the sensitivity to thermal drift, non-linearity, thermal noise, and ageing effects of the electrical circuitry [16]. These limitations and the availability of high-speed analog-to-digital converters have lead to the adoption of DSP.

The most simple DSP technique is fringe counting [167]. This technique obtains the displacement from the phase of the Doppler signal by counting the phase shift 2π periods, also known as zero crossings [165]. Fringe counting has been replaced by quadrature demodulation, a numerical method that is now feasible due to improvements in computational power [166, 167].

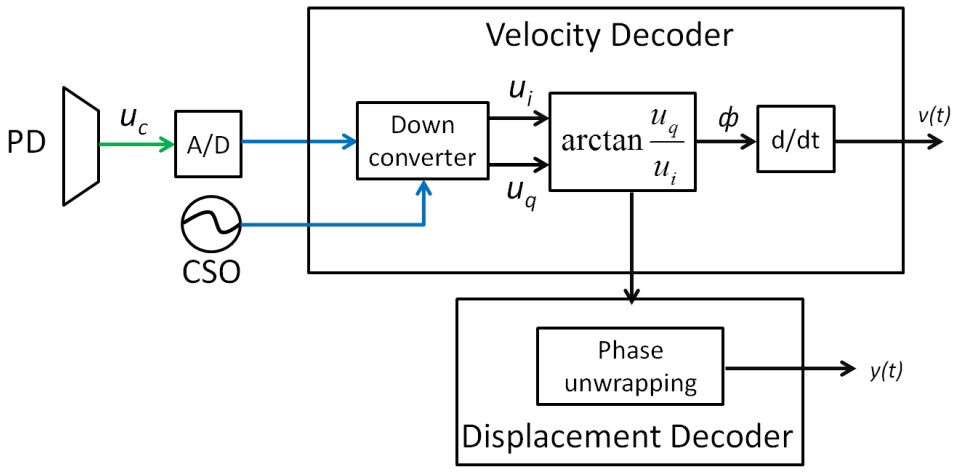

Figure 2.2: The DSP demodulation process of the analog heterodyne Doppler signal of the photodetector current, u_c. The in phase and quadrature signal pair are u_i and u_q, respectively.

The first step of the quadrature demodulation process, in Figure 2.2, is to convert the analog heterodyne voltage signal generated at the photodetector to a digital signal. Then the signal is passed to the decoders. Extracting the vibration velocity and displacement from the modulated signal has three parts [16]:

1. The heterodyne signal is converted to a quadrature, sine/cosine signal pair.
2. Phase calculation and unwrapping to determine the directionality of the displacement.
3. Calculation of the velocity from the phase by numerical integration.

The second and third part are independent of each other; the velocity may be calculated without unwrapping the phase. The displacement may also be calculated without phase unwrapping, but the directionality would be unknown.

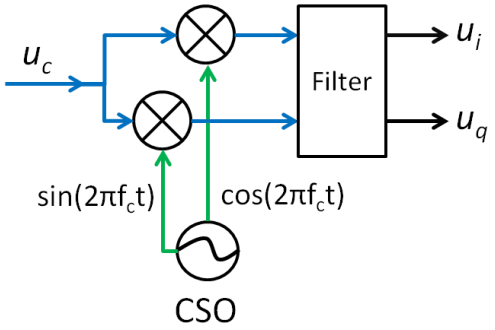

Figure 2.3: The down conversion of the heterodyne signal, u_c, to the quadrature signal pair u_i and u_q.

The first step of the conversion of the heterodyne signal to the quadrature base band, Figure 2.3, is to split the signal and pass it to two multipliers. There, the signal is mixed with the reference signal in quadrature format. This reference signal has the same carrier frequency that is provided to the BC, thus the signal is superimposed by $2f_c$ [165]. Then the pair is brought to the base-band by suppressing the carrier frequencies with a frequency filter [16]. Down-conversion may be performed as an analog process before conversion to a digital signal or in the DSP decoder block.

An alternative method to down conversion of the heterodyne signal in the digital domain is to down-mix the heterodyne signal to an intermediate frequency (IF) signal before generation of the quadrature signal pair [165]. Down-mixing is achieved by mixing the heterodyne signal with a reference frequency, f_R, that is less than the carrier frequency and then filtering to obtain a new signal with a frequency $f_{DM} = f_c - f_R$ [166]. The IF signal is then multiplied with a quadrature reference signal that is supplied by the CSO at the frequency f_{DM} and then brought to the base-band by filtering.

By either method, the base-band quadrature signal pair consists of the in-phase,

$$u_i(t) = U_i \cos\phi(t), \tag{2.4}$$

and quadrature,

$$u_q(t) = U_q \sin\phi(t), \tag{2.5}$$

components [167]. The wrapped phase is then known from the relationship [165, 167, 169, 170]

$$\phi_w(t) = \arctan\frac{u_q}{u_i}. \tag{2.6}$$

At this point, as per Figure 2.2, the phase may be differentiated to obtain the frequency shift, and thus the velocity, but the displacement cannot be known because the phase has no directionality.

The arctangent calculation is ambiguous at multiples of 2π, such that [16, 171]

$$\phi_m(t) = \phi_w(t) + a2\pi \tag{2.7}$$

where the integer a represents multiples of $\lambda/4$. Phase directionality is determined by "phase unwrapping". The phase is unwrapped by a polar co-ordinate transformation and an incremental period count by detecting the 2π phase jumps [167]. The displacement of the target is then known by [165]

$$y(t) = \frac{\lambda}{4\pi}\phi_m(t). \tag{2.8}$$

The accuracy of the demodulation is determined from an experimental calibration of the measured displacement and velocity made with a highly linear oscillator [172]. However, the full measurement bandwidth of the LDV cannot be characterized because the frequency range of high-precision mechanical oscillators is low with respect to the ultimate measurement bandwidth [16]. Therefore, the calibration of the DSP is achieved by analyzing an electronically synthesized Doppler signal [170]. The reported accuracy of the DSP decoding of the displacement and velocity are in the 0.1 % range [170].

Such measurements give an idea of the accuracy assuming that the heterodyne signal is itself error free. In reality, the error for LDV measurements arises from multiple sources in the signal processing chain, in the optics section, and from spurious noises. Noise and other factors affecting the LDV will be discussed in the next section.

2.3 Resolution and accuracy

In terms of the performance limits and the sources of error, the configuration of the optics section sets the lower limit of the resolution of a vibration measurement. This is mainly a function of the nature of light and the signal-to-noise ratio of the return beam, or rather the reflectivity of the target. In the case of an ideal optics section, the resolution limit is defined by the data acquisition and digital-to-analog data conversion. Measurement accuracy is affected by the signal preconditioning in the signal processing chain [16]. The sources of noise and other errors in the optics, the signal processing, and the greater electrical system will be discussed.

2.3.1 Noise and measurement errors in the optics section

The noise in the optical system arises from three-wave interference, high numerical aperture of optical focusing elements, target reflectivity and back-scattered light, and the speckle nature of light. Each of these problems affects the signal-to-noise ratio, and thus the measurement resolution. Some of them can be mitigated and some are intrinsic to the LDV.

Three-wave interference

Consider that the interrogated specimen may be in a vacuum chamber and the laser must pass through a glass lid. The glass will reflect some light back to the photodetector. The collection of an extra interference signal creates a ripple distortion in the measurement signal [170, 173]. The distortions become more significant with increasing power of the spurious reflections with respect to the object beam, which is inversely proportional to the distance from the glass to the target [173]. The problem is pronounced for vibrations where the amplitude is smaller than the laser wavelength and the power of the extra signal is comparable to the target signal intensity [174].

Three-wave interference effects can be reduced by moving any reflective apertures closer to the interferometer, tilting them, and with anti-reflective coatings. However, the three-wave interference effect can also be produced by the collection of back-scattered light from optically rough targets or light reflected from behind semi-transparent surfaces such as thin film nanomembranes or structures that are smaller than the laser spot size. In this case, distortion can be reduced by amplitude locked loop filters or low-pass filters [173].

Laser Speckle

Laser speckle causes a phase noise in the system. The imperfections of the target surface de-phase the reflected laser beam and cause interference patterns that create a speckled intensity on the photodetector [175]. Furthermore, the motion of the target causes the speckle patterns to produce a multitude of spurious signals with the same frequency but random phase [16]. For optically rough surfaces where the RMS roughness is larger than half the wavelength of the light, the phase is not coherent over the entire surface and demodulation of the Doppler signal is not possible [16].

Error due to the numerical aperture of the optics

The fringe spacing of the phase shifted measurement beam increases as a function of the numerical aperture of the optic lenses that project the laser beam [170]. This causes an amplitude error through diffraction and oblique incidence of the light [174]. The error is not

more than 1% for objectives less than 20X, but can become significant for higher objectives [170].

Target reflectivity and back-scattered light

Naturally, the optical reflectivity of the targeted specimen is important. A poor reflection reduces the power of the measurement beam relative to the reference beam, reducing the signal-to-noise ratio. It also increases the overall noise because back-scattered light from other sources becomes significant [170].

2.3.2 Noise and errors in the signal processing chain

The signal processing chain is subject to a variety of noise sources that affect resolution and errors that affect accuracy. These include, shot noise and thermal noise in the photodetector, signal conditioning, and decoding errors. Each will be discussed in turn.

Shot noise

Shot noise is an intrinsic white noise source that affects the photodetector current, u_c [166]. The shot noise represents the fundamental physical resolution limit of the LDV [169]. It arises because the illumination of the light is not perfectly steady, thus the current of the photodetector pulses and fluctuates [16]. The magnitude is determined by the detection bandwidth, the quantum properties of light, and the total optical power incident on the photodetector [169].

Thermal noise

Thermal noise, also known as Johnson noise, is another intrinsic noise in the photodetector current. The magnitude depends on the detector load resistance and bandwidth. This noise source can be controlled by tuning the bandwidth via the power of the reference beam and measurement beam [169]. However, the beam power also affects the shot noise and consequently the thermal noise is typically less than the shot noise.

Signal conditioning errors and decoding errors

The conversion of the heterodyne signal into the digital domain introduces errors due to the discretization of an analog signal [169]. Non-ideal digital filtering may cause amplitude errors, also [170]. The DSP demodulation of the Doppler signal is subject to computational errors, which cause an uncertainty in the 0.1% range [170].

Spurious noise

Finally, spurious noise peaks due to electrical cross-talk can affect any part of the LDV except the optics section [16]. Electromagnetic interference and electrical ground noises can also enter the system. These two sources of spurious noise peaks can be avoided by careful set up of the experimental system and trial-and-error shielding of electrical components [176].

2.4 Commercial laser Doppler vibrometers

In this section, two commercially sourced LDVs, the OFV-5000 and the UHF-120, which are used in this thesis to interrogate microresonator systems, are described. Both of the LDV systems are manufactured by Polytec Inc.

2.4.1 Polytec OFV-5000 laser Doppler vibrometer

The OFV-5000 is an LDV demodulation unit that interacts with the OFV-534 fiber coupled sensor head. The OFV-534 is a modified Mach-Zehnder heterodyne interferometer with a 633 nm HeNe laser and a built-in camera [177]. The laser is a class 2 with a power less than 1 mW. The focal length of the interferometer is ~30 cm with a 40 μm spot size and focusing lens attachments can bring the spot size down to 1.5 μm with a corresponding reduction in focal length. This is a single-point measurement system where alignment and laser focusing are manually set.

The OFV-5000 is equipped with a velocity (VD-09) and displacement decoder (DD-900). Both the digital decoders operate according to the theory outlined in Section 2.2.2; the velocity is measured from the un-wrapped phase of the heterodyne quadrature Doppler signal to save

calculation time and the unwrapped phase is passed to the displacement decoder [178]. The analog outputs can be post-processed with high-pass or low-pass filters.

The VD-09 digital broadband decoder has a maximum frequency range of 2.5 MHz and low-frequency limit of 0 Hz with a maximum measureable velocity of 10 m/s [178]. The DD-900 measurement capabilities depend on the selected measurement range of the VD-09 since it is passed the un-wrapped phase from the velocity decoder. The measurement range is the same as the VD-09 with a displacement resolution of less than 1 pm [178]. The maximum measureable displacement is a function of the frequency of the interrogated oscillation and the maximum measureable velocity of the VD-09.

At the best settings, the noise-limited resolution of the VD-09 increases from 0.01 $\mu m/s/Hz^{1/2}$ to 0.04 $\mu m/s/Hz^{1/2}$ over the 100 kHz measurement bandwidth [178]. The reduction in the resolution is due to the frequency dependence of the velocity noise [169]. Noise limited resolution is determined by a measurement of the noise on 3M Scotchlite tape and is defined as the signal amplitude at which the signal-to-noise ratio is 0dB with 1Hz spectral resolution [178]. The calibration error due to temperature fluctuations is ±1 % and the linearity error is 0.5 %. Linearity error is determined from the amplitude-dependent deviation of the scaling factor when subjected to a 1 kHz sinusoidal vibration at an amplitude 70% of the full scale measurement range of the decoder [178].

The ultimate resolution of the DD-900 is defined by the 0.4 mV quantization of the analog output and is at best 0.015 nm [178]. The noise-limited resolution of the DD-900 is 0.5 $pm/Hz^{1/2}$ [178]. The phase noise is flat as a function of frequency [169].

Due to the relationship between the velocity and displacement, the velocity decoder has a greater signal to noise ratio [178]. Thus, for low-frequency measurements, the displacement decoder has a low amplitude ceiling and can be overloaded easily. To obtain high precision displacements of low-frequency vibrations, it is best to integrate the velocity data rather than use the displacement decoder directly [178].

2.4.2 Polytec UHF-120 laser Doppler vibrometer

The UHF-120 is a scanning vibrometer where a field of measurements on the surface of a resonator can be referenced to the phase of a driving frequency to animate the mode shapes [16]. Scanning is achieved by rastering the interrogated specimen underneath the interferometer objective lens with a precision nano-positioning stage. The spatial resolution of the scanning measurement depends on the laser spot size, which is greater than the positioning stage resolution [168]. The laser spot size for a 5x, 10x, and 20x objective lens is 10 μm, 4.5 μm, and 2.5 μm respectively. This scanning feature is only applicable for stationary vibrations where the power spectrum does not change over time. Each of the scanning points, though, is essentially a single point measurement and the principle of operation is the same as the OFV-5000 decoder.

The UHF-I-120 interferometer measures the vibrations with a solid state 3R class laser with a power less than 5 mW and a 532 nm wavelength. A Bragg cell carrier frequency of 620 MHz allows for direct acquisition of velocities up to 150 m/s and vibration frequencies up to 600 MHz [168]. Mathematical bandwidth extension brings the frequency range up to 1.2 GHz.

The quadrature heterodyne Doppler signal is digitally demodulated and the displacement is calculated by the arctangent method. The displacement resolution is 2 picometers or 30 $fm/Hz^{1/2}$. The displacement resolution defines the velocity measurement resolution because the velocity is calculated by differentiating the displacement [168].

2.5 Experimental measurement of LDV noise and resolution.

The practical resolution limits of the OFV-5000 and the UHF-120 LDVs are experimentally determined. These measurements are made on 3M Scotchlite tape and representative microcantilever beams using acquisition settings that reflect typical measurement conditions.

2.5.1 The experimentally measured noise of the OFV-5000

The resolution of the OFV-5000 LDV is experimentally determined by a measurement of the noise using five microcantilever specimens and 3M Scotchlite tape. These specimens are

featured in Chapter 5 and the details regarding their dimensions and characteristics can be found there. At this point, they are only considered to be representative of actual resonators that are used in the thesis.

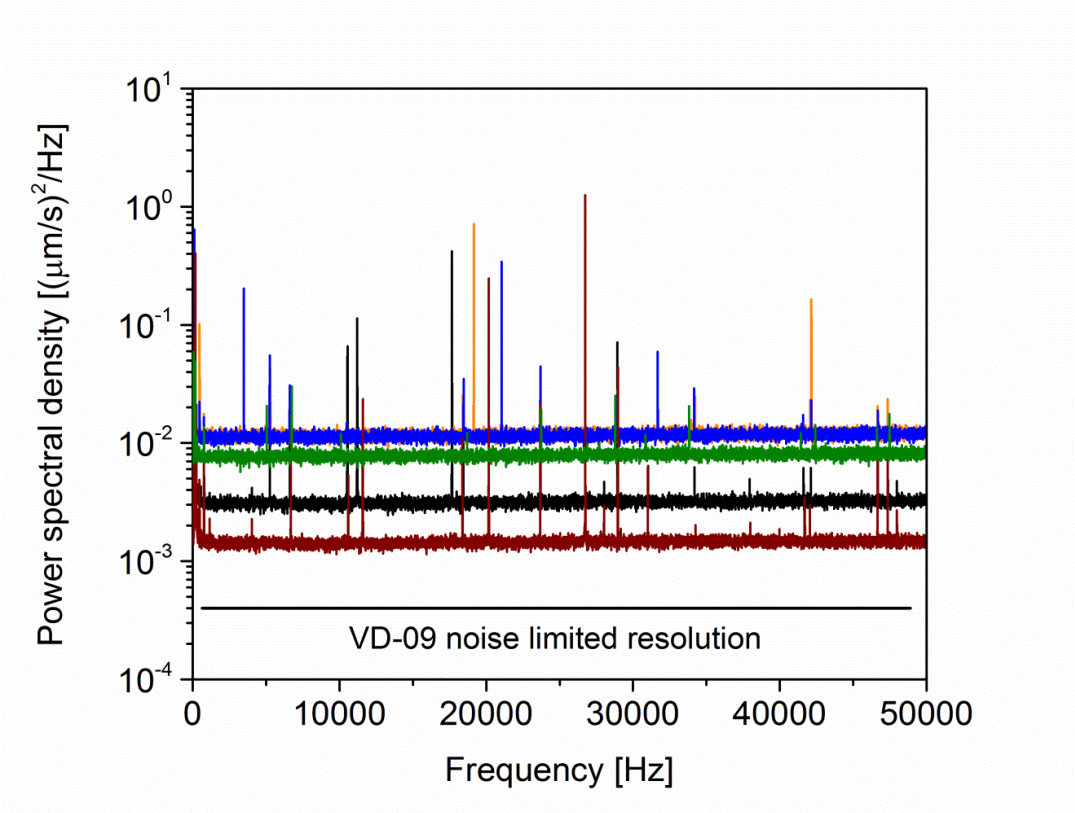

Figure 2.4: The PSD of the system noise using the VD-09 decoder with a sensitivity of 5 mm/s/V and a 100 kHz sampling frequency. The solid black line is the factory specified noise limited resolution and the other plots are the PSD of the velocity time series measured on the surface of silicon microcantilever beam specimens. The brown is Specimen 1, the blue is Specimen 2, the orange is Specimen 3, the black is Specimen 4, and the green line is a measurement on 3M reflective tape.

The noise is measured using the VD-09 velocity decoder at the best sensitivity of 5 mm/s/V for 90s at a sampling frequency of 100 kHz. The power spectral density (PSD) of the velocity time series of the noise is calculated and plotted in Figure 2.4. At 10 kHz, 20 kHz and 30 kHz, one thousand data points are binned and averaged to define the mean noise. The frequency dependence of the noise floor for the VD-09 velocity decoder is given in Table 2-1.

Table 2-1: The experimentally measured noise limited resolution at three frequencies in the measured frequency spectrum using the VD-09 velocity decoder. The noise is measured on four silicon microcantilever beam specimens and 3M reflective tape.

Specimen	Noise floor (μm/s)/Hz$^{1/2}$		
	10 kHz	20 kHz	30 kHz
1	0.038	0.039	0.038
2	0.108	0.108	0.108
3	0.107	0.108	0.109
4	0.056	0.056	0.057
3M tape	0.089	0.089	0.091

The experimentally measured noise floor shows that the measurement resolution is in reality greater than the factory specified mean resolution of 0.02 (μm/s)/Hz$^{1/2}$. The resolution floor is dependent on the interrogated specimen. This suggests that optical noise from light scattering limits the system and highlights the importance of laser beam alignment, surface preparation, and sample reflectivity.

2.5.2 The experimentally measured noise of the UHF-120

The resolution limit of the UHF-120 is obtained from a measurement of the noise measured on 3M reflective tape using a 5x objective lens. The noise is recorded for 6.4 ms at a 4 MHz sampling rate for a frequency resolution of 156.25 Hz. The measured noise, plotted in Figure 2.5, has a 1/f component that decays to the optical noise floor at ~475 kHz. The experimentally measured noise floor is 84 pm for a single-shot measurement with no data averaging. This noise floor is more than an order of magnitude greater than the minimum resolution according to factory specifications.

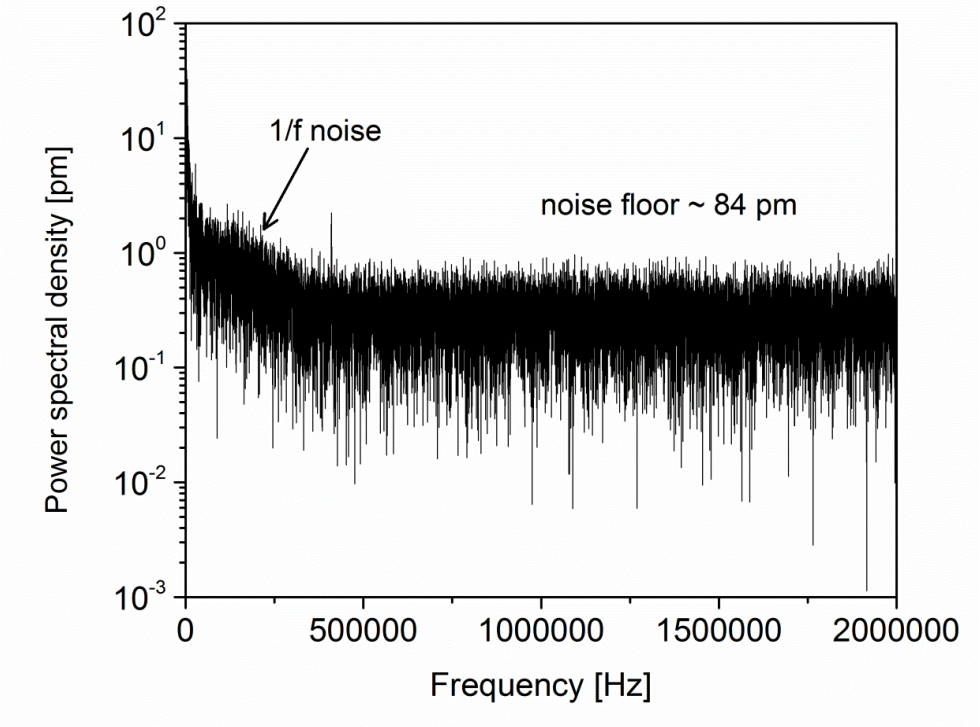

Figure 2.5: The PSD of the measured noise of the UHF-120 LDV on 3M reflective tape. The recording of the noise was 6.4 ms in duration at a sampling rate of 4 MHz.

2.6 Summary

This chapter has discussed the working principles of laser Doppler vibrometry and explained sources of error that arise from the interferometry and signal decoding. The characteristics of two commercial LDVs (OFV-5000 and UHF-120) have been described and the noise limited measurement resolution has been experimentally determined. The resolution of the OFV-5000 LDV is shown to be limited by the optical noise from the target reflectivity. The next chapter describes the damping measurement system where the LDV is used to measure the dynamics of single-crystal silicon microcantilever beams.

CHAPTER 3

Apparatus for measuring material damping as a function of temperature (20˚C to 150˚C)

This chapter describes schematics and protocols for the instrumentation (pumps, function generator, clamps and excitation elements) and the fabrication of the microcantilever beam specimens. Then the principles of electrostatic excitation and the method of controlling the resonator dynamics are discussed. This is followed by the procedure to measure and analyze the logarithmic decrement of free-decay with a linearity and bias check. The analysis methods are implemented to measure the damping in a set of microcantilever beams using a vice-like clamp and electrostatic actuator. The damping measured with this system is calibrated to the damping measured using a well-documented clamp and base-excitation actuator.

3.1 The experimental instrumentation for measuring the free-decay

The measurement of damping in microcantilever beam resonators is performed using two experimental platforms: (1) a system using base-excitation designed by Sosale [17] and (2) a system, capable of heating, using electrostatic excitation designed by Shalabi [124]. The former platform will be referred to as the base excitation system (BES) and the latter as the electrostatic excitation system (EES). The performance of the BES has been well documented and used extensively to study the frequency dependence of the material damping of thin metal films and nano-wires [17, 18, 97, 98, 146, 147]. On the other hand, the work in this thesis represents the debut of the EES. Both of these platforms use the same microcantilever beam resonators, the same experimental infrastructure, and the experimental methodology is essentially the same. Thus, the performance characteristics and capabilities of the EES can be calibrated, at room temperature, to damping measurements made with the BES, in addition to calibration to the TED limit.

The experimental platform has seven core components:

1. A vacuum chamber and pumps.
2. A clamp for the microcantilever resonator.

3. A function generator.
4. An actuation system for the microcantilever resonator.
5. A thermostat (relevant for the EES).
6. A laser Doppler vibrometer to measure the vibration of the resonator.

The components can be categorized as instrumentation (LDV), appliances (vacuum chamber and pumps), controllers (function generator, thermostat), and devices (clamp, actuator, microcantilever). The configuration of these components, except the microcantilever, support and actuator, and the LDV decoder, are demonstrated in Figure 3.1. The central element of the system is the microcantilever beam which is operated inside of a vacuum chamber. The specific configuration and operation of each of the components will be presented in the following sections.

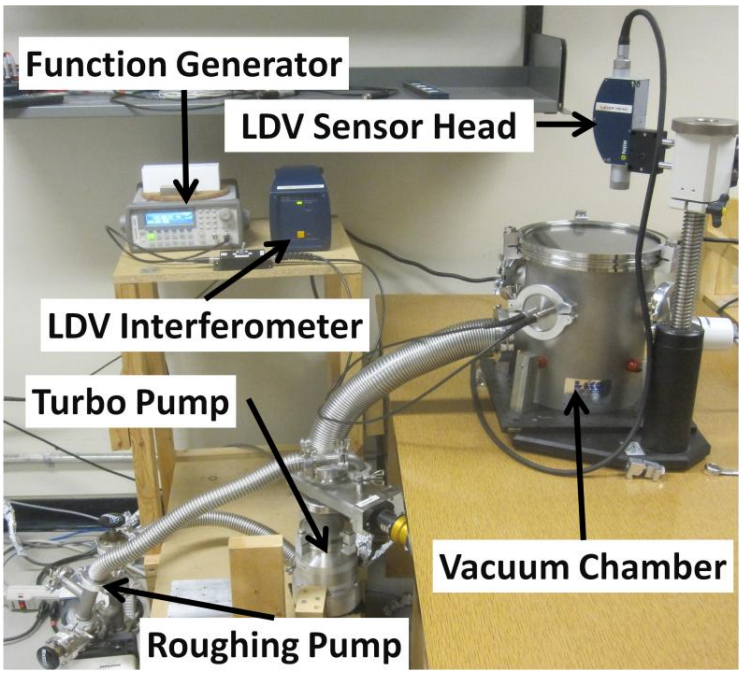

Figure 3.1: The experimental platform to measure the damping consists of the turbo and roughing pump, the vacuum chamber, the function generator, and the LDV interferometer and sensor head. The LDV decoder and the clamp are not pictured here.

3.1.1 The function generator

The function generator (33220A, Agilent Technologies, USA) is used to control the actuation of the microcantilever. The function generator can supply up to a 10 V peak-to-peak AC signal with a maximum 10 V DC offset. This instrument is capable of generating broadband white noise or signals carried on a pure frequency. For a pure frequency, the resolution is 1×10^{-5} Hz with a maximum frequency of 1 MHz. This ceiling exceeds the maximum sampling rate, 125 kHz, of the data-acquisition card (NI USB-6211, National Instruments Corp., USA) that is used to collect the analog voltage signal supplied by the LDV.

3.1.2 The vacuum chamber and pumps

The vacuum chamber shown in Figure 3.1 is custom manufactured (LACO Technologies, USA). This stainless steel vacuum chamber is 10 inches tall and has an eight inch diameter. In addition to the glass viewing port on the top of the vacuum chamber, there are six access ports that are sealed with KF kwik-flange connectors, viton rubber gaskets and Dow Corning high vacuum grease. These ports allow for electrical feeds, evacuation, and pressure gauging. The pressure is monitored with a Pirani Gauge (Alcatel Vacuum Inc, Canada).

The vacuum chamber is connected to the pumping appliances by stainless steel bellows. A turbo-molecular pump (Adixen ATP80 turbo pump, Alcatel Vacuum Inc, Canada) and a low vacuum roughing pump (Alcatel Pascal 2005SD, Alcatel Vacuum Inc, Canada) provide enough power to reach a maximum low-pressure of 3×10^{-6} mbar.

3.1.3 The clamp and actuator

The use of a set of interchangeable beams with a dedicated clamp for the mechanical spectroscopy of damping is a historical precedent set by the work of Berry and Pritchet [93]. The advantage of this method is that the anchor loss will be consistent for all tests and structures [17]. Another advantage is that the fabrication of the microcantilever beams can be simplified if the actuation and supporting arrangements do not need to be designed and fabricated in parallel. This also makes it simpler to post-process the resonators using standard microfabrication methods.

Based on this concept, Sosale designed a vice-like clamp that is interfaced with a piezoelectric actuation element. The detailed design process and schematics can be found in Sosale's PhD thesis [17]. The excitation of the beam is achieved by vibrating the entire clamp. The arrangement of this system does not allow for the incorporation of extra features, such as heating and cooling elements due to excitation mechanics and the low weight loading limit of the piezoelectric actuator. To extend the measurement of damping to higher temperatures, Shalabi designed a clamping system with an integrated heating element [124]. The actuation of the microcantilever is achieved with electrostatic excitation, which also increases the operating frequency range. However, the electrostatic force is very sensitive to the distance between the resonator and the electrode [179]. The details of both of these clamps and actuator platforms are described in turn.

The base-excitation system (BES)

Piezoelectric actuators are widely employed for positioning specimens in microscopy and as a consequence are commercially available. The BES uses the Nano-OP 65 (Mad City Labs, Wisconsin, USA), a single-axis piezoelectric nano-positioning stage with a capacitive displacement sensor (CDS) for feedback. When supplied with a sinusoidal AC voltage, the positioning stage effectively becomes an oscillator. This system, Figure 3.2, offers precise control of the excitation frequency and the beam vibration amplitude is maintained by in-situ monitoring and termination of the excitation force. The dynamics of the shaker measured with the CDS have been corroborated by the LDV and the displacement is linear for all normal excitation amplitudes [17]. The CDS shows that the response of the system stops instantly when the driving voltage is cut. The CDS signal also indicates if the clamp has been excited by an external energy source, which would invalidate the recorded free-decay of the microcantilever beam.

The piezoelectric shaker is powered by a 150 V amplifier (Nanodrive85). The piezoelectric shaker has a 65 μm displacement range and an acceleration of up to 5 m/s^2 with a 1% precision. A 175 g stainless steel clamp is bolted to the shaker face. The clamp is precision machined for flatness and parallelism where the base of the microcantilever beam is in contact with the surfaces of the clamp. The smoothness of the clamping surfaces and clamping pressure

are critical to prevent slip-stick friction [79]. The beam is held securely on the clamp by a plate that is guided by pins and tightened down with six screws. The protocol for the operation of the BES is:

1. The microcantilever specimen is centered in the clamp with the base of the beam slightly overhanging the edge.
2. The top of the clamp is tightened with six screws. They are tightened in a left-to-right pattern in 1.0 lb-in increments from 6.5 lb-in to 9.5 lb-in.
3. The clamp is loaded onto the shaker backing plate and the four screws are tightened in a clockwise direction in 1.0 lb-in increments from 6.5 lb-in to 9.5 lb-in.
4. The entire rig is placed into the vacuum chamber and pump down is initiated. When the pressure is less than 1×10^{-4} mbar, the beam may be actuated.
5. A sinusoidal voltage signal (0.5 V) is sent to the shaker by the function generator at the beam's resonance frequency
6. When the amplitude of the microcantilever beam is maximized, the voltage to the shaker is terminated. At this point, the free-decay of the microcantilever is recorded.

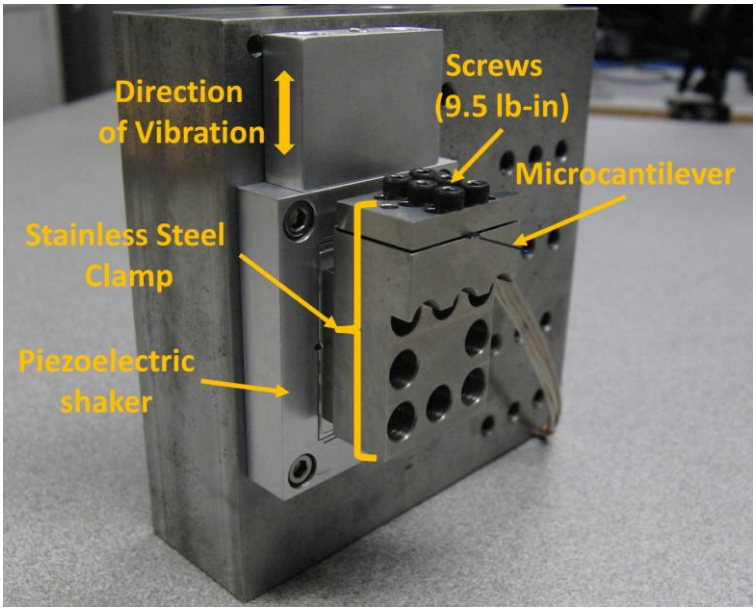

Figure 3.2: The base-excitation system is pictured with the main components labeled. Note that the piezoelectric shaker is attached to a much larger steel block, which serves as a handle and an inertial mass.

The electrostatic-excitation system (EES)

The EES, Figure 3.3, is machined from stainless steel and a low conductive, zero out-gassing Macor ceramic [180]. The EES has been designed to integrate an electrical resistance heater cartridge (CSS-20270/120, Omega Engineering Inc.) and thermocouples. The clamping section of the EES is essentially a vice, precision machined for flatness and parallelism between the bottom and the clamping plate. The screw on top of the vice clamp is tightened with a torque wrench to secure the beam. The tightening routine is the same as the BES. The clamped beam is shown in the inset of Figure 3.3 and the separation of the beam from the counterelectrode is perceptible as a slight shadow. The Macor ceramic that separates the clamping section from the counterelectrode is for electrical isolation. The bottom of the EES is made of the Macor ceramic to minimize heat loss into the environment through conduction.

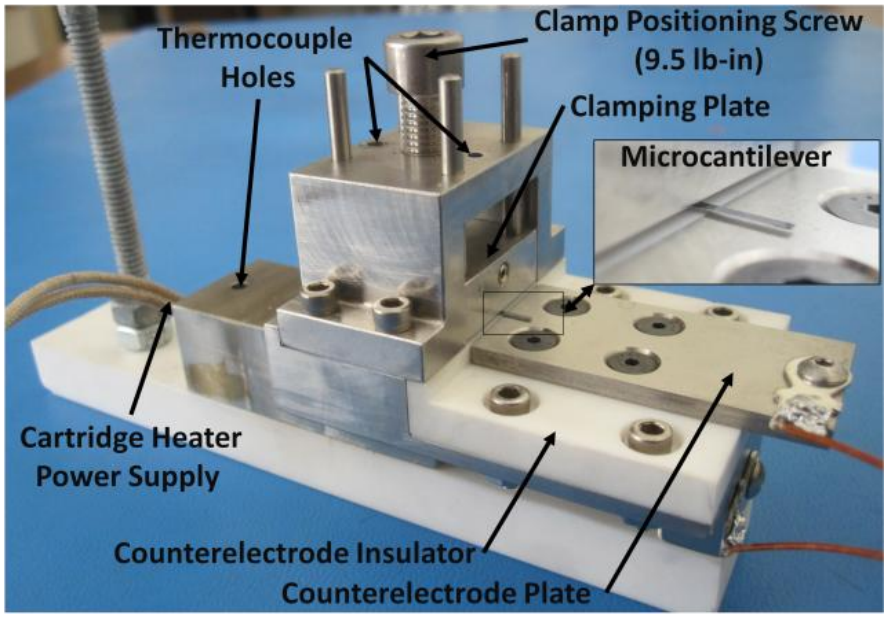

Figure 3.3: The electrostatic excitation system is pictured with an inset showing the beam portion of the microcantilever emerging from the clamp.

Not visible in Figure 3.3, the cartridge heater is located in the back of the rig where the power supply wires emerge and reaches under where the microcantilever beam is clamped. The cartridge heater is approximately 2 inches long and 3/8 inches in diameter and has a maximum output of 70 W when supplied with 120 V and a maximum temperature of 677 ˚C. A coiled

resister is wound through a ceramic core with a stainless steel sheath, giving it a 35 W/in^2 watt density. Thermal grease is used to improve the conduction to the housing. Experimental trials indicate that the thermal grease outgases significantly and hardens, preventing the removal of the cartridge heater and slowly changing the heating regime.

In vacuum, J-type thermocouples (XDH-30-R-12, Omega Engineering Inc.) are used to measure the temperature at the heater, at the base of the microcantilever beam, and at the clamping plate. The thermocouples can measure temperatures up to 300 ˚C with an accuracy of ±1 ˚C, calibrated with boiling water. The thermocouples and the cartridge heater are connected to a thermal controller (CN616TC1, Omega Engineering Inc.) that provides a DC output to a solid state relay (SSR330DC10, Omega Engineering Inc.) to control the power supply with an on-off thermostat. The power supplied to the heater is manually controlled with a variable transistor.

The operational protocol to use the EES system is similar to the protocol for the BES. The nuances of electrostatic excitation are described in Section 3.3 and the heating protocol is described in Chapter 4.

3.2 The design and fabrication of microcantilever beams

Two designs of microcantilever beams were developed by Sosale to cover different frequency ranges while preserving the resolution [17]. One design will be referred to as the low frequency beam (LFB) and the other will be referred to as the high frequency beam (HFB). The LFB design covers a frequency range of 40 Hz – 2 kHz and the HFB design covers a range from 1.5 kHz to 70 kHz. Both of the microcantilever design types were manufactured in the McGill Nanotools Microfab using recipes developed by Sosale. The specific steps and designs are described in the next sections

3.2.1 Microfabrication process for the low-frequency microcantilever beam (LFB)

The LFB microcantilever beams are constructed from a 6” single-side polished, 550 μm thick (100)-oriented commercial grade single-crystal silicon wafer. The wafer has a low concentration (~10^{15} cm^{-3}) of boron doping. First the wafer is prepared with a solvent cleaning

step (isopropyl alcohol, Acetone, de-ionized (DI) water) and a Piranha etch (4:1, H_2SO_4 : H_2O_2). Then the wafers are oxidized at 1100 ˚C for 26 minutes to grow a 500 nm thick SiO_2 film on both sides in a wet chemical vapor deposition (CVD) process in an oxidation furnace (Tylan). The oxide layer is patterned using a standard photolithographic process. The pattern is to delineate a section of the wafer with and without oxide.

For the patterning step, a 1.4 μm thick layer of S1813 positive photoresist (Microposit) is spin-coated onto the surface, baked at 115 ˚C for 60 seconds, and exposed to ultraviolet (UV) light at a dose of 70 mJ/cm^2 using the EVG620 photomask aligner (EV Group). Then the exposed wafer is developed in MF-319 (Microposit) for 45 seconds, and rinsed in DI water. After this, the wafer is hard-baked at 90 ˚C for 90 seconds. The patterned photoresist on the top side of the wafer is used as a masking layer to dry etch the oxide on the top side of the wafer. The dry etching of the exposed oxide is performed in a reactive ion etcher (RIE) (Applied Materials P5000). The wafer is exposed to multi-gas plasma at 100 mTorr pressure for 100 seconds. The gas plasma is composed of CHF_3, Ar, and CF_4 at a flow rate of 45 sccm, 70 sccm, and 7 sccm, respectively. After the oxide layer is etched, any residue resist layer is removed using oxygen plasma for 300 seconds at 45 sccm and 150 mTorr of pressure.

After both sides of the wafer have been patterned, the wafer is diced in the direction parallel to the [110] plane into 2.5 mm wide strips. Then these strips are dipped in a buffered hydrofluoric acid bath to remove the native oxide and are then placed in a tetra methyl ammonium hydroxide (TMAH) bath. The TMAH is heated to 90 ˚C and is diluted to 27 % with DI water for an average etch rate of 20 μm/hour for single-crystal silicon. Since it is nearly impervious to the TMAH, the oxide layer serves as a mask to define the base section of the microcantilever beam. The TMAH anisotropically etches the single-crystal silicon along preferential crystal planes, resulting in a 54.74˚ angle step from the base to the microcantilever beam. The thickness of the microcantilever beams is defined by the etching time. The length of the beam is defined by cutting the beam with a diamond scribe.

3.2.2 Microfabrication process for the high-frequency microcantilever beam (HFB)

The HFB microcantilever beams are constructed from a 6" diameter double-side polished (100)-oriented commercial grade silicon-on-insulator (SOI) wafer with a low concentration (~10^{15} cm^{-3}) of boron doping. The SOI wafers have three layers: a thin device layer, a very thin oxide layer, and a thick handle layer. The device layers that are available for these wafers are 7.5-24 μm thick. The buried oxide (BOX) layer is 600 nm and the handle layer is 530 μm thick. Using SOI wafers allows for the precise control of the microcantilever beam thickness because the BOX layer can be used as an etch stop for TMAH so the device layer defines the beam thickness.

The first manufacturing step is a solvent clean and a Piranha etch. Then the wafers are oxidized at 1100 ˚C for 26 minutes to grow a 500 nm thick SiO_2 film on both sides in a wet thermal CVD process. Then a standard photolithographic process is completed on the top side of the wafer to pattern the outline of the microcantilever beams. The RIE etching of the exposed oxide uses the procedure established for the LDV construction.

After the oxide has been patterned on the top side of the wafer a monolayer of hexamethyldisilazane (HMDS) is applied to improve the adhesion of photoresist and prolong its life in the next dry etching step. Next, a 10 μm layer of positive AZ9245 photoresist (AZ Electronic Materials) is spin coated on the top-side of the wafer and is soft-baked at 115 ˚C for 150 seconds. The mask used in the previous photolithographic step is used again to expose the AZ9245 layer with four doses of 250 mJ/cm^2 UV light. Then the exposed AZ9245 is developed in a 4:1 solution of DI water and AZ400 developer (AZ Electronic Materials). Finally, the wafer is post-baked at 115 ˚C for 150 seconds.

The next part of the process is to etch through the device layer using deep reactive ion etching (DRIE). The patterned oxide and AZ9245 act as hard masks for this DRIE etching. The DRIE (Tegal SDE110) uses a gas mixture of C_4F_8, O_2, and SF_6 with respective flow rates of 300 sccm, 200 sccm, and 700 sccm. The distance from the wafer to the source is 170 mm and the source power is 2700 W. Residual resist is removed with oxygen plasma.

Now that the outline shape of the microcantilevers has been patterned, the back side of the wafer is patterned. First 100 nm of oxide is thermally grown on the wafer. This oxide layer is to protect the etched silicon on the top side during future etching steps. A 1.4 µm thick layer of S1813 is spin coated on the backside and patterned in the shape of the base portion of the microcantilever using the same recipes as before. This pattern is aligned with the patterns on the front side of the wafer. Then the exposed oxide is etched in the RIE. Next a monolayer of HMDS and 10 µm of AZ9245 are deposited on the backside of the wafer. This resist layer is also patterned to outline the base portion of the microcantilever beams. The exposed silicon is etched all the way to the device layer in a DRIE step. However, due to non-uniform gas distribution, the DRIE does not etch all the way through the handle layer. Therefore, a TMAH etch is used to release the beams. The final step in the process is a hydrofluoric acid dip to remove the oxide layers from the beam.

3.2.3 Comparison of the LFB and HFB

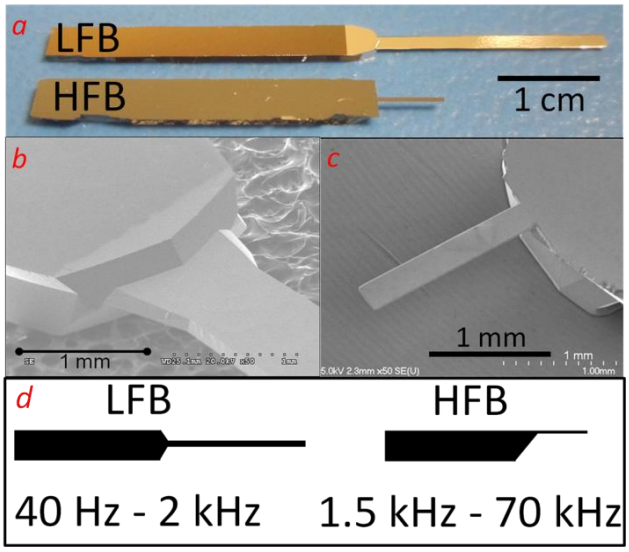

Figure 3.4: A comparison of the LFB and HFB designs. (a) A photograph shows the relative size difference between the two classes of microcantilever beams. The LFB has been coated with an aluminum film, thus increasing its reflectivity compared to the pure single-crystal silicon HFB. (b) An SEM image shows the angled step transition from the microcantilever beam to the base portion of the LFB. (c) An SEM image shows how the top surface is planar at the junction of the cantilever and base of the HFB. (d) The frequency range and profile of the two designs are compared.

Both the LFB and the HFB have been designed to reduce the clamping loss by incorporation of a filet at the junction between the beam and the base. The size of the base section is the same for both types, thus anchor loss is assumed to be approximately the same for both designs [17, 106]. As illustrated in Figure 3.4, the main difference is that the cross-section of the microcantilever beam specimens is slightly different, though functionally the same. Due to the overhanging edge of the top clamping plate, the EES cannot be used with the HFB microcantilevers.

3.3 Principles of electrostatic actuation

Electrostatic actuation is coupled to the dynamics of the microcantilever beam; the electrostatic force is a function of the distance between the beam and a grounded counterelectrode [181, 182]. For a bending beam, the intensity of the electrostatic force is not evenly distributed and, when coupled to the elastic restoring force and damping, a pull-in force instability occurs [179, 183]. Thus, the response of the beam may not be linear at higher beam deflections [124]. Understanding the principle of operation is essential for the implementation and operation of the EES.

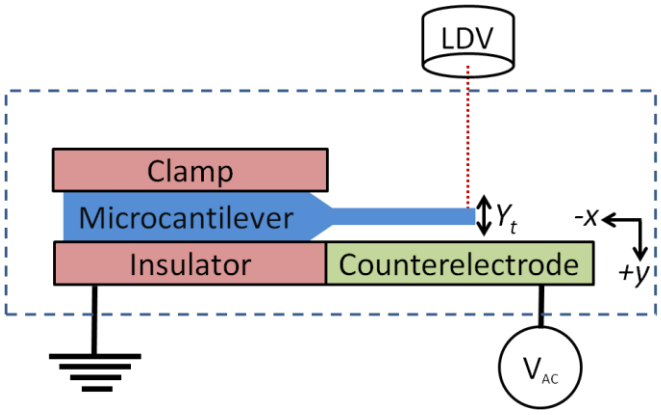

Figure 3.5: A cartoon of the electrostatic excitation system. The blue dashed line represents the vacuum environment and the red dotted line represents the laser. The cantilever displacement is denoted as Y_t and the coordinate system defines the direction of positive displacement.

To explain the principles of electrostatic excitation, consider the illustration, Figure 3.5, of the relationship of the EES to the other parts of the damping measurement system. The microcantilever beam is in a vacuum environment, represented by the blue dashed lines. The

LDV is shown outside of the vacuum chamber with the interrogation beam (red dotted line) focused on the end of the microcantilever. The microcantilever is electrically grounded and isolated from the counterelectrode. The base of the microcantilever is securely clamped, ensuring that the beam portion has a single degree of freedom.

The microcantilever beam has dimensions defined such that *L*, *w*, and *h*, are the length, width, and thickness respectively. The displacement is an oscillation about the neutral axis of the microcantilever beam, such that positive displacement is towards the counterelectrode plate. When the beam is at rest, the distance between the counterelectrode plate and the beam is defined as $d = d_o$. Since the beam is a continuous system, when the beam bends, the distance *d* is a function of the axial position along the length, $0 < x < L$. In terms of the maximum deflection at the end of the beam, $Y_{x=L}$, the deflection at position *x* is defined by [27]

$$Y_x = B_n \varphi_n. \tag{3.1}$$

where $B_n = \dfrac{Y_{x=L}}{\varphi_{n,x=L}}$ and φ_n is the mode shape function

$$\varphi_n = \left(\cos(\lambda_n x) - \cosh(\lambda_n x) - \psi\left(\sinh(\lambda_n x) - \sin(\lambda_n x)\right)\right). \tag{3.2}$$

In this equation $\lambda_n = \beta_n / L$, where β_n is a constant and ψ is given by

$$\psi = \frac{\cosh(\lambda_n L) + \cos(\lambda_n L)}{\sinh(\lambda_n L) + \sin(\lambda_n L)}. \tag{3.3}$$

Ignoring fringe fields around the beam, the grounded beam and the charged counterelectrode form an ideal capacitor [124]. The beam is pulled towards the counterelectrode by an electrostatic force, *P*, generated by charging the counterelectrode plate with a sinusoidal AC voltage, [124]

$$V_{AC} = V \sin(2\pi ft). \tag{3.4}$$

The excitation frequency is half of the microcantilever resonance frequency because of the nature of the electrostatic excitation. The electrostatic force pulls the beam towards the electrode; the electrostatic force does not push the beam. Therefore a difference between the actuation frequency and the resonance frequency of the beam will result in the restorative elastic energy in the beam being countered by the electrostatic force.

The magnitude of the electrostatic force acting on the beam is a function of the applied V_{AC}, the relative dielectric constant of the medium between the beam and the counterelectrode, ε_r, the vacuum permittivity, ε_o, and the distance between the counterelectrode and the beam. The electrostatic force is distributed along the length of the beam. The force per unit length is [184]

$$P(x) = \frac{\varepsilon_o \varepsilon_r w V_{AC}^2}{2(d_o - Y_x)^2}. \tag{3.5}$$

The displacement due to this force is found by solving the bending equation [121]

$$EI \frac{d^4 Y}{dx^4} = -\frac{\varepsilon_o \varepsilon_r w V_{AC}^2}{2(d_o - Y_x)^2}, \tag{3.6}$$

where E is the Young's modulus and I is the area moment of inertia.

The problem is simplified by approximating the electrostatic force as a point load on the beam at a position x. Then, the deflection at the tip of the beam is given as [185]

$$dY_{x=L} = \frac{x^2}{6EI}(3L - x)P(x)dx. \tag{3.7}$$

Taking into account the distribution of the force along the entire length of the beam, Equation 3.7 is integrated,

$$Y_{x=L} = \int_0^L \frac{(3L - x)}{6EI} x^2 P(x) dx. \tag{3.8}$$

The beam deflection at any point x along the length is approximated by assuming a square law curvature so that [185]

$$Y_x = \left(\frac{x}{L}\right)^2 Y_{x=L} \int_0^L \frac{(3L - x)}{6EI} x^2 P(x) dx \tag{3.9}$$

The integral in Equation 3.8 is then solved for a normalized electrostatic load, H, [185]

$$H = 4\Delta^2 \left(\frac{2}{3(1-\Delta)} - \frac{\tanh^{-1}\left(\sqrt{\Delta}\right)}{\sqrt{\Delta}} - \frac{\ln(1-\Delta)}{3\Delta} \right)^{-1}, \tag{3.10}$$

where $\Delta = (Y_{x=L} / d)$ is the normalized deflection at the tip and [185]

$$H = \frac{\varepsilon_o \varepsilon_r w L^4 V_{AC}^2}{2EId^3}. \tag{3.11}$$

Equations 3.10 and 3.11 can be combined to solve for the voltage,

$$V_{AC} = \sqrt{\frac{2EId^3}{\varepsilon_o \varepsilon_r w L^4} 4\Delta^2 \left(\frac{2}{3(1-\Delta)} - \frac{\tanh^{-1}\left(\sqrt{\Delta}\right)}{\sqrt{\Delta}} - \frac{\ln(1-\Delta)}{3\Delta} \right)^{-1}}, \tag{3.12}$$

that is necessary to excite the beam to a desired amplitude, $Y_{x=L}$.

When applying an excitation voltage, three limiting criteria are taken into account to achieve a stable, linear vibration that satisfies the Euler-Bernoulli beam theory assumption of low amplitude, low strain displacements:

1. The applied voltage should not exceed the pull-in voltage of the electrostatic actuation.
2. The amplitude of the beam should be in the linear regime; the amplitude at the end of the beam should not exceed the thickness of the beam.
3. The strain at the root of the beam should not exceed $\varepsilon_{xx,max} = 10^{-5}$.

For the possible dimensions of the microcantilever beams, The pull-in voltage, [186]

$$V_{PI} = \sqrt{\frac{18EId^3}{5wL^4\varepsilon_o}}, \tag{3.13}$$

is greater than the maximum voltage that the function generator can supply. The maximum strain in the microcantilever exceeds the defined tolerance before the amplitude at the end of the beam is greater than the thickness. Therefore, the excitation voltage is controlled to limit the strain in the beam.

The maximum strain occurs at the root of the cantilever so that [121]

$$\varepsilon_{xx,\max} = \frac{h}{2}\frac{\partial^2 Y_{x=0}}{\partial x^2} = B_n \frac{h}{2}\ddot{\varphi}_{x=0}, \tag{3.14}$$

where $\ddot{\varphi}_{x=0} = 2\lambda_n^2$. For a defined $\varepsilon_{xx,max}$, Equation 3.14 can be rearranged to define the maximum amplitude at the end of the microcantilever beam,

$$Y_{\max,x=L} = \frac{\varphi_{x=L}\varepsilon_{xx,\max}}{h\lambda_n^2}. \tag{3.15}$$

Theoretically, Equation 3.15 can be combined with Equation 3.12 to precisely control the applied voltage and achieve a deflection according to a given maximum strain. However, the lack of cross-section symmetry and difficulty of measuring *d* for each specimen makes this a cumbersome strategy. Instead, the dynamics of the microcantilever beam are monitored in real time with the LDV and the excitation voltage is terminated before the vibration amplitude reaches the strain limit defined in Equation 3.14.

The OFV-5000 LDV measures the velocity of the vibration in units of volts, V_{LDV}, where [178]

$$V_{LDV} = \frac{v}{\Theta} = \frac{Y\omega_n}{\Theta} \tag{3.16}$$

and Θ is a conversion factor of 5 mm/s/V. In Equation 3.16, the natural frequency ω_n is defined as [123]

$$\omega_n = \frac{\beta_n^2}{L^2}\sqrt{\frac{EI}{\rho A}} = 2\pi f_n, \tag{3.17}$$

where ρ is the density and *A* is the cross-section area. Placing Equation 3.16 into Equation 3.15, the maximum tolerable voltage of the LDV is

$$V_{LDV,\max} = \frac{\omega_n\varphi_{x=L}\varepsilon_{xx,\max}}{h\lambda_n^2\Theta}. \tag{3.18}$$

The actuation voltage can then be terminated when the amplitude of the beam, as measured at the LDV, approaches the limit defined in Equation 3.18. This formulation is also applicable to the operation of the BES as well. The limitation of this method is that the measurement location is assumed to be the approximate end of the microcantilever beam. If the interrogation spot is further from the end, the strain will be underestimated.

3.4 Measuring the damping by the logarithmic decrement of free-decay

The logarithmic decrement is calculated from the relative amplitude of consecutive peaks in a sinusoidal oscillation that is allowed to freely decay. To understand this consider the equation of motion of a simple harmonic oscillator,

$$y'' + 2\zeta y' + \omega_n^2 y = 0, \tag{3.19}$$

where y(t) is the displacement as a function of time. Consider that the oscillator is given an initial displacement that is allowed to freely decay. The displacement of this free decay follows the form of

$$y(t) = y_{t=0} \exp(-\zeta\omega_n t)\sin(\omega_d t) \tag{3.20}$$

where the damped natural frequency is

$$\omega_d = \omega_n \sqrt{1-\zeta^2}. \tag{3.21}$$

Now if the decay is described in terms of vibration cycles, the time advances according to r cycles by

$$t = t_o + \frac{2\pi r}{\omega_d}. \tag{3.22}$$

Substituting this into Equation 3.21, the amplitude per cycle becomes

$$y_r = y_0 \exp\left(- 2\pi r \frac{\zeta}{\sqrt{1-\zeta^2}} \right). \tag{3.23}$$

The logarithmic decrement is defined as [27]

$$\delta = 2\pi \frac{\zeta}{\sqrt{1-\zeta^2}}. \tag{3.24}$$

Substituting Equation 3.24 into Equation 3.23 and solving for δ, the logarithmic decrement can be calculated according to

$$\delta = \frac{1}{r} \ln\left(\frac{y_o}{y_r} \right). \tag{3.25}$$

3.4.1 Calculation of the logarithmic decrement from experimental data

For the experimentally collected data, the measurement of the logarithmic decrement from the free-decay data has several steps. First, the voltage time series data is selected from the point where the actuation is cut to when the vibration approaches the noise floor, as seen in Figure 3.6. Including the noise floor will skew the logarithmic decrement and resonance frequency measurements that are extracted from this data. Next, a custom peak picking algorithm searches the free-decay time series for data points that are greater than their ten nearest neighboring peaks. Finally, the isolated peaks are analyzed to extract the resonance frequency and logarithmic decrement.

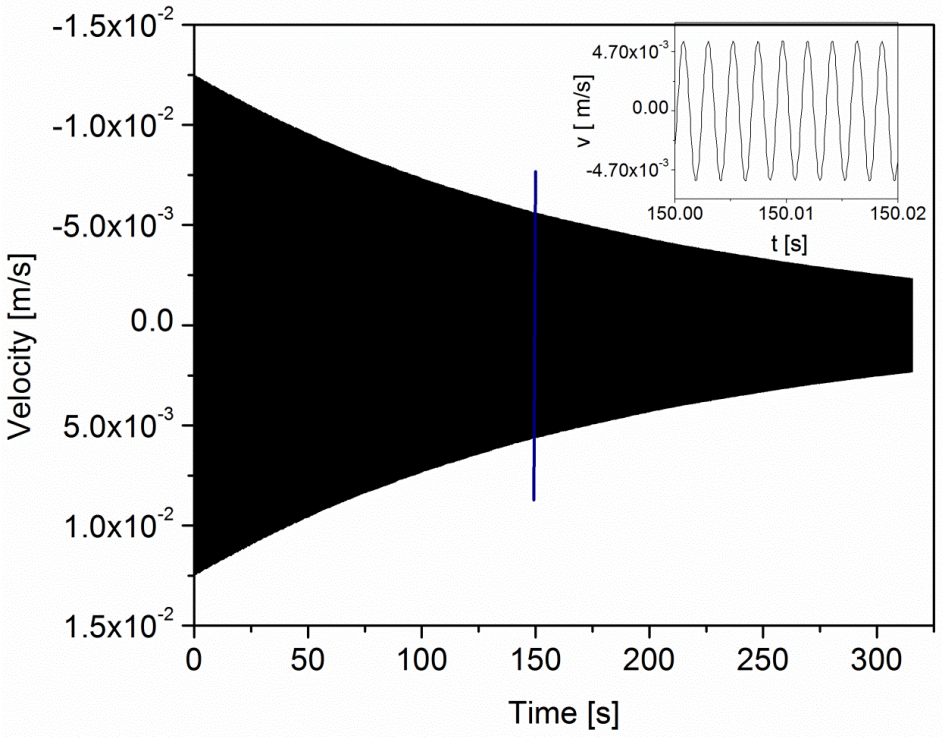

Figure 3.6: The characteristic velocity time series of the free-decay is shown for a microcantilever resonator. The vertical line through the data indicates the position of the inset.

Theoretically, only two cycles of vibration are needed to calculate the logarithmic decrement. In practice, many cycles of vibration are taken into account to improve the accuracy of this method. Noise and the finite sampling rate add uncertainty to both the amplitude and the time stamp of each peak. Therefore, the amplitude of each peak relative to every other peak in the free-decay data set should be evaluated and averaged. For large data sets, the evaluation of ${}_rC_2$ number of calculations is cumbersome. Instead, the relative amplitude of every peak is evaluated in one approximation.

Assuming an exponential decay, the log of the peak data should have a linear slope. A linear best fit line is fit to log of the peak data. Then the logarithmic decrement for the entire free-decay data set is

$$\delta = \frac{t_r J}{r} \tag{3.26}$$

where J is the slope of the best fit line.

The free-decay peak data is also analyzed to measure the resonance frequency. As a consistency check, the resonance frequency is measured by two independent methods. The PSD of the time series is computed and analyzed to find the frequency of the resonance peak, distinguished from noise peaks by its characteristic Lorentzian curve and high amplitude [187]. The second method is to measure the time between consecutive peaks. However, the discrete time sampling and noise cause a fluctuation so the time must be averaged by

$$\frac{1}{f} = \frac{\sum t_m - t_{m+r}}{r}. \tag{3.27}$$

Noise, recording duration, and finite sampling frequency also affect the measurement of the logarithmic decrement. A simple check on the quality of the data is to visually inspect the fit of the free-decay data and check that the "goodness of fit" R^2 residual is at least 0.98. Non-linear damping would easily be detected if the best fit line strayed from the center of the extracted peak data. However, the presence of noise can cause artificially high R^2 and mislead the experimenter. For instance, the variance of the selected peaks in Figure 3.7 is wide enough that a poor fit may go undetected.

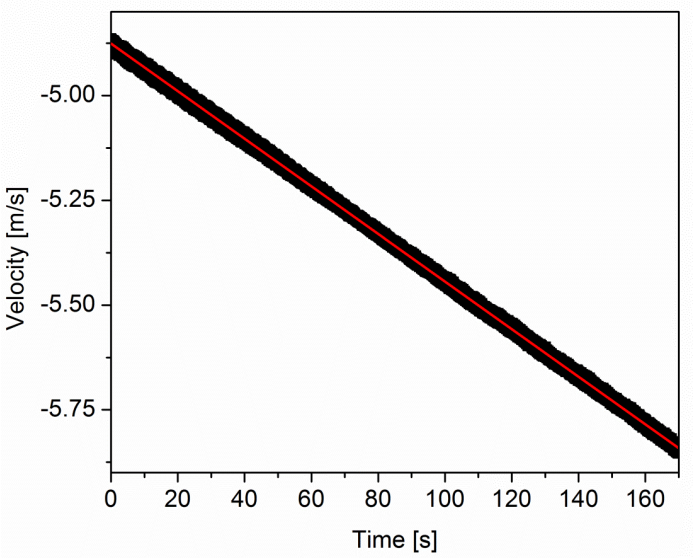

Figure 3.7: The extracted peaks from a free-decay are fit with a line by a linear regression method. The $\delta = 1.26 \times 10^{-5}$ and $R^2 = 0.99$ for this fit.

Thus, an analysis to determine the effect of the experimental variables on the error of a measurement of the logarithmic decrement is necessary and discussed in the following sections and a strategy to check the quality of the collected free-decay data is outlined.

3.4.2 The effect of the recording duration of the free-decay time series on the calculated logarithmic decrement

According to Equation 3.26, the length of the free-decay time series directly effects the measurement of the logarithmic decrement. To determine the effect, a long recording of the free-decay time series is segmented into pieces and then incrementally reassembled. Each segment is progressively longer than the previous segment. The smallest piece is 10 cycles and the longest is 86000 cycles. From 10 cycles to 20000 cycles, 10 cycles are added to each consecutive segment. From 20000 cycles to 86000 cycles, the incremental addition to each segment is 100 cycles. For each segment, the logarithmic decrement and resonance frequency are measured and the results are displayed in Figure 3.8.

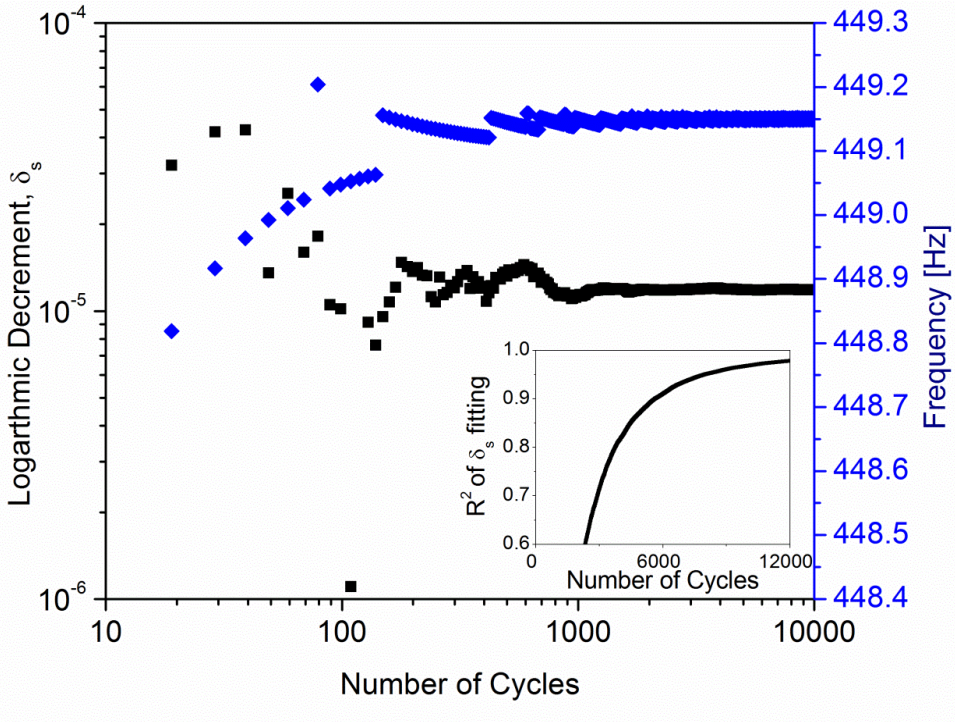

Figure 3.8: The logarithmic decrement (black squares) and resonance frequency (blue diamonds) as a function of the number of cycles in the free-decay data. The inset shows the R^2 of the linear regression as a function of the number of cycles.

At a segment length of 2000 cycles, the logarithmic decrement measured for each segment converges to within 0.1% of the logarithmic decrement measured for the entire data length of 86000 cycles. Above 9000 cycles, the measured resonance frequency is stable. For segments greater than 9000 cycles, the difference between the resonance frequency for each segment and the resonance frequency measured for the full data does not fluctuate more than 0.0001%. From the analysis of the parameters, 9000 would be the minimum number of cycles necessary to accurately measure the frequency and damping from the free-decay time series.

While the calculated logarithmic decrement is considered stable at 2000 cycles, the R^2 is 0.53, which indicates the fit is not representative of the data. The fitting residual reaches the 0.98 threshold at 12000 cycles and 0.99 at 16000 cycles. Thus, the convergence of the R^2 is used to define the minimum necessary number of cycles because it determines when the number of data points overcomes the variance of the selected peak data. Based on this analysis, 12000 cycles is determined to be the minimum required length of the recorded free-decay data. This criterion can be used to calculate the minimum recording time based on the resonance frequency of a given microcantilever specimen.

3.4.3 The effect of the sampling frequency on the measured logarithmic decrement and resonance frequency

The sampling rate affects the clarity of time series; the completeness of the depiction of a continuous sinusoidal wave form by discrete sampling is a function of the sampling rate. For calculating the logarithmic decrement, the accuracy of the amplitude and time information contained in the waveform is important. Ideally, a maximum sampling rate would provide the most detail of the time series. Practical issues, such as data size, computing power, and computational analysis time, limit the maximum sampling rate. Accordingly, the optimal sampling rate is defined according to the required minimum. To find this minimum sampling rate, a simple experiment is conducted.

For a series of increasing data sampling rates, the logarithmic decrement is measured five times and averaged. The measured frequency and logarithmic decrement at each sampling rate are listed in Table 3-1.

Table 3-1: The effect of the sampling rate on the measured resonance frequency and logarithmic decrement is summarized. The given values of the resonance frequency and logarithmic decrement at each sampling rate are extracted from five independent measurements of the free-decay.

Sampling rate	f [Hz]	δ
10 kHz	790.6	2.56×10^{-4}
20 kHz	3069.8	6.60×10^{-5}
30 kHz	3066.7	6.58×10^{-5}
40 kHz	3069.8	6.64×10^{-5}
50 kHz	3069.8	6.66×10^{-5}

Accordingly, a 10 kHz sampling rate does not capture enough information of the time series to accurately measure the resonance frequency or the logarithmic decrement, despite being great enough to satisfy the Nyquist theorem. From this study, it is determined that the sampling rate needs to be at least seven times greater than the resonance frequency of the microcantilever beam resonator.

3.4.4 Method to evaluate the quality of the free-decay data and calculated logarithmic decrement

In Sections 3.4.2 and 3.4.3, the effect of the recording time and sampling frequency is experimentally determined and strategies to minimize the deleterious effects are introduced. However, these strategies do not address the effect that noise may have on the measured logarithmic decrement. Noise here includes the thermal noise floor, spurious electrical noises, and mechanical disturbances. These noises are inherently random, thus there is no strategy to specifically eliminate them beyond working in a quiet atmosphere with adequate electromagnetic shielding. Instead, an active approach is taken to check the quality of the measured free-decay data based its consistency. That is, the data is examined to determine whether the free-decay is being corrupted in some manner. Corrupted data could come in the form of non-linear damping, amplitude excitation, or frequency shifting during the length of a recording.

Checking for an amplitude excitation is performed when optically inspecting the best fit line in comparison to the log of the peak data. A check for non-linear damping and frequency shifting is accomplished by segmenting the data into segments of 12000 cycles. Then the logarithmic decrement and resonance frequency are evaluated for each segment. The mean value of the damping, Figure 3.9, and resonance frequency, Figure 3.10, measured for each segment are checked for convergence to the values measured from the complete data set. For the logarithmic decrement, a 2% standard deviation is the maximum acceptable variance.

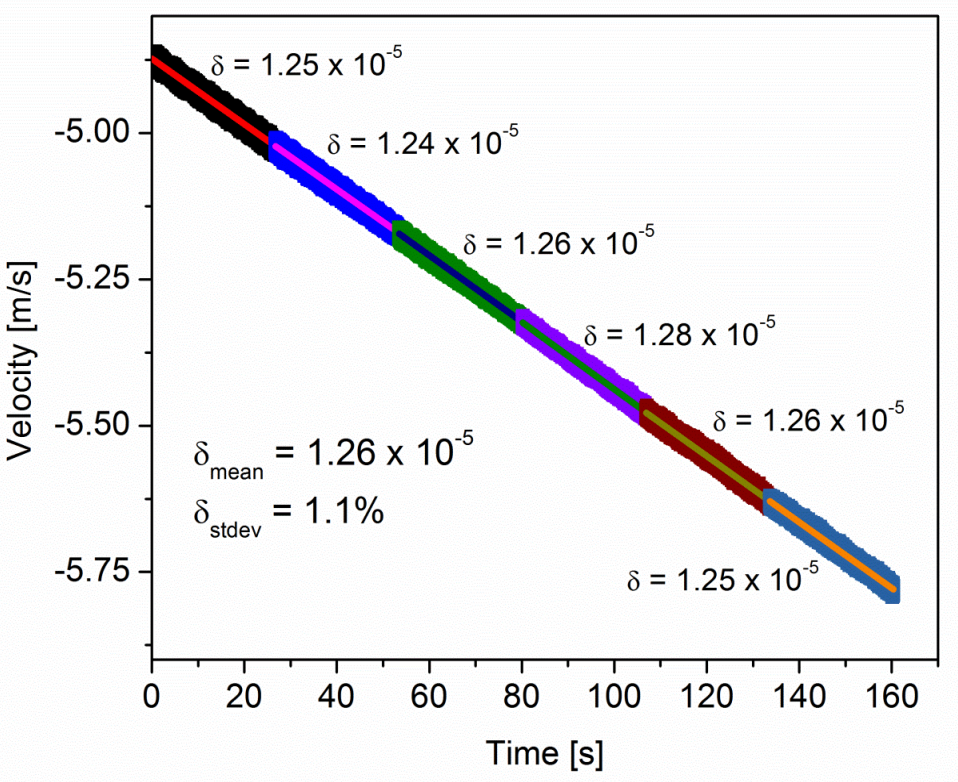

Figure 3.9: A free-decay data set is segmented into sections that are 12000 cycles long and the δ extracted from each segment is compared to the δ measured from the full data set. The variance of the δ measured from the segmented data is 1.1% and the mean is equivalent to the damping measured from the full data set.

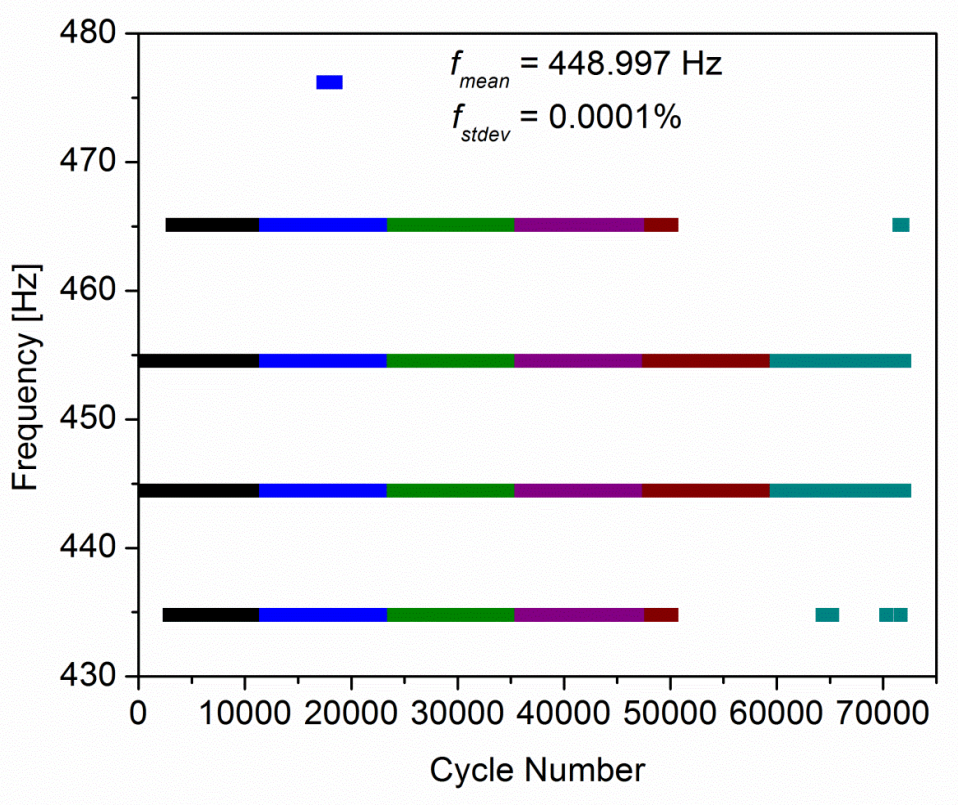

Figure 3.10: The free decay is segmented into lengths of 12000 cycles and the resonance frequency is measured by the time interval between consecutive cycles for each segment. The average frequency for each segment is 448.997 Hz. The standard deviation of the six segment frequencies is 0.0001%.

3.4.5 Summary of the experimental measurement of the logarithmic decrement

In Section 3.4, the method to calculate the logarithmic decrement from the free-decay of vibration is presented. Then the influence of the recording time and sampling frequency on the measured damping is experimentally determined. This study is then extended to propose a method to check the free-decay data for aberrations based on the consistency of the logarithmic decrement and resonance frequency. Based on these results, the procedure for measuring the logarithmic decrement of damping is:

1. A measurement of the free-decay is obtained using a sampling frequency at least 7 times greater than the resonance frequency.

2. The recording time of the measurement is at least 36000 cycles long. The maximum recording time is defined such that the recording is terminated well before the amplitude of the vibration is approaching the thermal noise floor.
3. The collected data is segmented into lengths of 12000 cycles and the logarithmic decrement and resonance frequency are calculated for each segment. The standard deviation for the damping from the segmented data must be less than 2%.
4. Steps 1-4 are repeated to generate 5 measurements of the damping and resonance frequency.
5. The five measurements of the damping and resonance frequency are averaged. The standard deviation should be less than 2%, following the protocol of Sosale [17].

This procedure is employed in the next section to measure the damping of a set of single-crystal silicon microcantilever beams using the EES and BES.

3.5 Experimental measurements of damping and frequency at room temperature

In this section, the instruments and experimental protocols described in the previous sections are implemented to measure the damping in a set of microcantilever beams using the BES and EES. The experimental measurements are compared between each platform in the discussion section. Then the magnitude of the damping is compared to theoretical descriptions of the relevant damping mechanisms. The TED limit is then used to calibrate the measurements according to the residual damping. The residual damping is a measure of all the other damping mechanisms subject to the microcantilever and thus defines the resolution of the damping measurement. The final evaluation is the damping measurement repeatability of the EES.

3.5.1 Results

The damping of a set of 17 single-crystal silicon microcantilever beams at the first and second mode resonance frequency has been measured using the EES and BES. For this set of LFB specimens, the base is ~550 μm thick, 1.5 mm wide and ~5 cm long. The thickness of the beam is measured at three different positions along the length to ensure that the taper is less than 10%. The dimensions of the beam portion range from 24 μm < h < 90 μm thick and from 10 mm < L < 29 mm in length. The width of the beam averages w = 700 μm. The beam dimensions,

listed in Table 3-2, are used to predict the resonance frequencies. The damping measured using the EES and BES platforms are listed in Table 3-3.

Table 3-2: The predicted first and second mode resonance frequency compared to the measured values, $f_{1,\delta}$ and $f_{2,\delta,}$ respectively, using the EES and BES. The reported error is the standard error for five measurements. *The error for the EES measured frequency of Specimens 1, 2, and 3 is 0.28%, 0.26%, and 0.1% respectively. †The error for the measured frequency of Specimens 4, 13, and 16 is 0.006%, 0.002%, and 0.011% respectively.

ID #	L [mm]	h [μm]	Theory		BES	EES		
			f_1 [Hz]	f_2 [Hz]	$f_{1,\delta}$ [Hz] (±.001%)	$f_{1,\delta}$ [Hz] (±.02%)	$f_{2,\delta}$ [Hz] (±.01%)	$f_{2,\delta}/f_{1,\delta}$
1	17.0	24.0	115.0	732	113.5	113.2*	791.8	7.0
2	29.2	91.9	149.0	949	143.1	143.5*	948.8	6.6
3	18.1	42.1	178.3	1135	147.3	147.1*	1216.9	8.3
4	26.5	83.6	164.0	1046	155.0 †	155.1	1065.8	6.9
5	20.8	62.52	199.7	1271	198.8	198.8	1322.5	6.7
6	18.0	58.1	247.8	1577	235.5	235.7	1676.1	7.1
7	16.9	62.51	302.3	1924	276.4	276.4	1878.0	6.8
8	15.3	52.63	312.0	1986	281.6	281.6	1965.4	7.0
9	13.0	40.3	327.9	2087	290.6	290.5	2402.1	8.3
10	16.4	61.8	317.8	2023	301.2	301.2	1995.4	6.6
11	10.0	25.0	360.0	2291	353.4	353.2	2985.9	8.5
12	14.5	57.8	380.7	2423	357.6	357.6	2393.5	6.7
13	10.5	35.1	441.1	2807	387.3 †	387.3	3081.4	8.0
14	13.0	57.5	470.0	2995	420.4	420.4	2812.8	6.7
15	12.5	54.2	478.0	3042	432.6	432.6	2920.7	6.8
16	12.7	56.8	491.1	3125	448.8 †	449.2	3069.8	6.8
17	10.2	54.7	730.0	4646	664.8	664.7	4574.2	6.9

Table 3-3: The measured logarithmic decrement using the BES and EES with the reported standard error. The numeral subscripts denote the damping measured at the first and second mode resonance frequency.

ID #	BES	EES	
	$\delta_{s,1}$	$\delta_{s,1}$	$\delta_{s,2}$
1	6.99×10^{-6} (± 10%)	6.94×10^{-6} (± 67%)	9.93×10^{-6} (± 5%)
2	2.12×10^{-5} (± 0.8 %)	1.01×10^{-5} (± 23%)	4.88×10^{-5} (± 9%)
3	6.21×10^{-6} (± 6%)	4.87×10^{-6} (± 11%)	2.30×10^{-5} (± 2%)
4	1.81×10^{-5} (± 6%)	1.06×10^{-5} (± 8%)	4.92×10^{-5} (± 1%)
5	8.16×10^{-6} (± 2%)	7.16×10^{-6} (± 6%)	3.13×10^{-5} (± 0.2%)
6	9.10×10^{-6} (± 2%)	7.31×10^{-6} (± 5%)	4.06×10^{-5} (± 0.2%)
7	1.02×10^{-5} (± 1%)	7.40×10^{-5} (± 3%)	4.24×10^{-5} (± 0.3%)
8	7.87×10^{-6} (± 1%)	6.49×10^{-6} (± 3%)	3.47×10^{-5} (± 5%)
9	5.68×10^{-6} (± 2%)	3.58×10^{-6} (± 3%)	3.68×10^{-5} (± 0.2%)
10	1.28×10^{-5} (± 1%)	7.98×10^{-6} (± 2%)	4.70×10^{-5} (± 0.3%)
11	5.50×10^{-6} (± 4%)	1.17×10^{-5} (± 0.4%)	2.59×10^{-5} (± 0.3%)
12	1.29×10^{-5} (± 2%)	1.17×10^{-5} (± 0.6%)	4.95×10^{-5} (± 0.1%)
13	7.70×10^{-6} (±1%)	6.65×10^{-6} (±6%)	3.33×10^{-5} (± 0.5%)
14	9.70×10^{-6} (± 1%)	9.77×10^{-6} (± 1%)	5.18×10^{-5}(± 0.3%)
15	1.05×10^{-5} (± 1%)	1.06×10^{-5} (± 1%)	5.69×10^{-5} (± 0.5%)
16	1.42×10^{-5} (± 1%)	1.11×10^{-5} (± 0.4%)	6.60×10^{-5} (± 1%)
17	1.55×10^{-5} (± 0.5%)	1.57×10^{-5} (± 0.3%)	8.24×10^{-5} (± 0.1%)

3.5.2 Discussion

For both frequencies and for both systems, the measured frequencies do not match the estimated values and the difference can be as great as 13%. Concerning the first mode frequency, for the whole set, the standard error of the frequency measured with the BES is lower. For the EES, the error of the measured frequency of Specimens 1, 2, and 3 are an order of magnitude greater than the average. Excepting those three specimens and Specimen 16, the magnitude of the resonance frequency measured using both experimental platforms agree within 0.1 Hz.

Note that the second mode frequency is not increasing sequentially for the data set. The measurement of the second mode frequency is evaluated with respect to the first mode frequency. The ratio of the first and second mode is, theoretically, a constant given by [27, 121, 123]

$$\frac{\omega_2}{\omega_1} = \frac{\lambda_2^2}{\lambda_1^2} = \frac{4.73041}{1.875104} = 6.3642. \tag{3.28}$$

All of the specimens have a ratio greater than the theoretical ratio. Four specimens have a frequency ratio that is greater than 10% of the mean frequency ratio (mean frequency ratio = 7.1). The reason for the trend and outliers is unclear, but are grounds to remove those specimens from future use.

For the specimens with resonance frequency below ~300 Hz, the standard error of the first mode damping is greater for measurements conducted with the EES but is otherwise comparable for both platforms. The damping measured at the second mode and, in general, the magnitude of the damping is best evaluated in terms of the theoretical damping from TED, Akhiezer damping, internal friction, and support loss. With the room temperature properties of single-crystal silicon, Table 3-4, the magnitude of theoretical damping can be estimated.

Table 3-4: The material properties of single-crystal silicon at room temperature [106, 110, 188-193]. The coefficient of linear expansion is α, the thermal conductivity is k, the specific heat per unit volume is C_v, the speed of sound is v_s, the Grüneisen parameter is γ.

E [N/m^2]	ρ [kg/m^3]	α [K^{-1}]	k [W/m/K]	C_v [J/m^3/K]	v_s [m/s]	γ
169×10^9 ± 1%	2333	2.67×10^{-6} ± 2.01%	144.75 ± 3.12%	1.6×10^6 ± 2.75%	8.3×10^3	0.452

For an isotropic, homogenous Euler-Bernoulli beam subjected to an oscillating stress field, the magnitude of TED is given by [63]

$$\delta_{TED} = \pi \frac{E\alpha^2 T_0}{C_v} \frac{\Omega}{1+\Omega^2} \tag{3.29}$$

where T_o is the equilibrium temperature and Ω is the normalized frequency,

$$\Omega = \omega_n \frac{h^2 C_v}{\pi^2 k}. \tag{3.30}$$

The Akhiezer damping is calculated from [84]

$$\delta_{Akhiezer} = \pi \frac{C_v \gamma^2 T_0}{\rho v_s^2} \frac{\omega_n \left(\frac{3k}{C_v v_s^2} \right)}{1+\omega_n^2 \left(\frac{3k}{C_v v_s^2} \right)^2}, \tag{3.31}$$

and is on the order of 10^{-7} for all of the specimens, about an order of magnitude less than the TED.

The single-crystal silicon microcantilever beams are assumed to be free of defects such that the internal friction is caused by the boron doping. Internal friction is interpolated from experimental results tabulated in Hung [106] for the relationship between the resistivity, ion-implantation, and internal friction. The boron doping is ~10^{15}/cm^3 for these single-crystal silicon microcantilevers and the internal friction damping is estimated to be ~10^{-6} [106, 116].

The anchor loss is a combination of support loss and clamping loss. The support loss is estimated from [41, 42]

$$\delta_{\text{support}} = \pi \frac{1}{0.95} \frac{L}{w} \left(\frac{h_b}{h} \right)^2, \tag{3.32}$$

where h_b is the thickness of the support. The thickness of the clamping vice in the EES is 25 mm and the support loss is estimated to be on the order of 10^{-7}. There is no model available to estimate the clamping loss, but it can be inferred based on the theoretical contributions of the support loss, TED, Akhiezer damping, and internal friction.

Thus, TED is the dominant damping mechanism for this set of microcantilever beams. In Figure 3.11, the damping at the first and second mode using the EES is plotted against the TED limit.

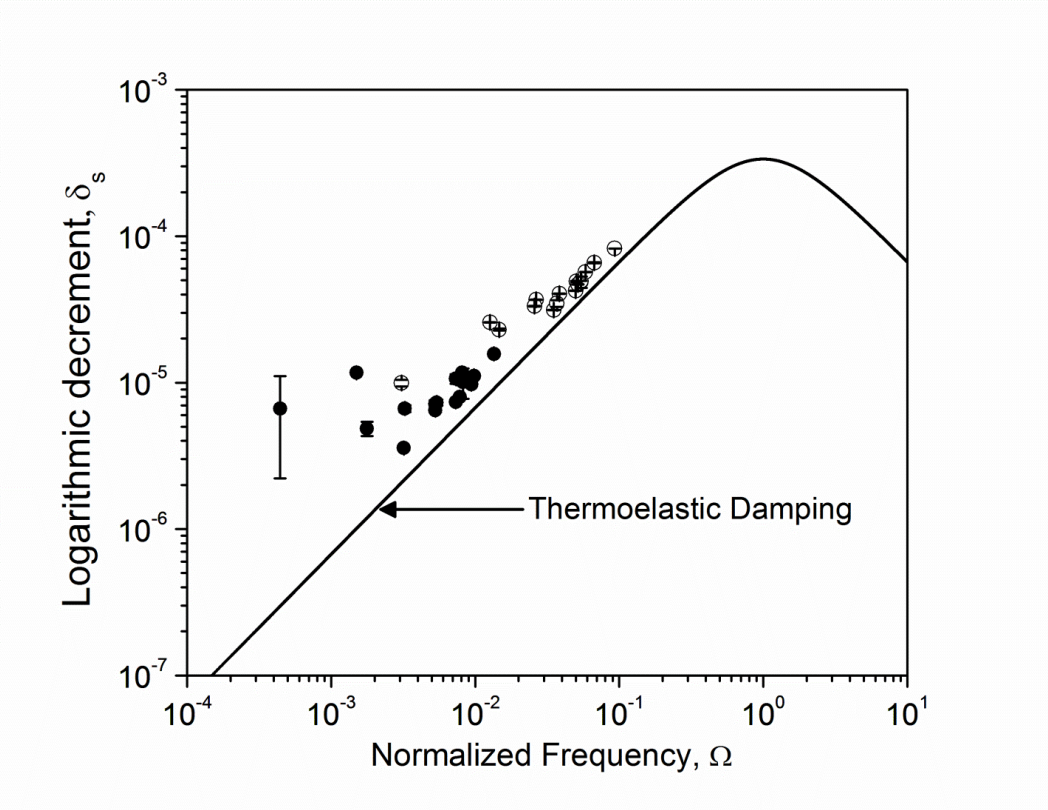

Figure 3.11: The measured damping at the first and second mode frequency using the EES are plotted against the TED limit for a set of 17 single-crystal silicon microcantilevers at room temperature. The error bars denote the standard deviation of five measurements that have been averaged to make one data point.

The difference between the measured damping and the TED limit is consistent for all specimens measured using the EES. This difference has been termed the "residual damping" [17]. If the measured damping in a pure single-crystal silicon cantilever beam is δ_s, then the residual damping is

$$\delta_{residual} = \delta_s - \delta_{TED}. \tag{3.33}$$

The residual damping measured for all specimens and modes for both the EES and BES are compared in Figure 3.12.

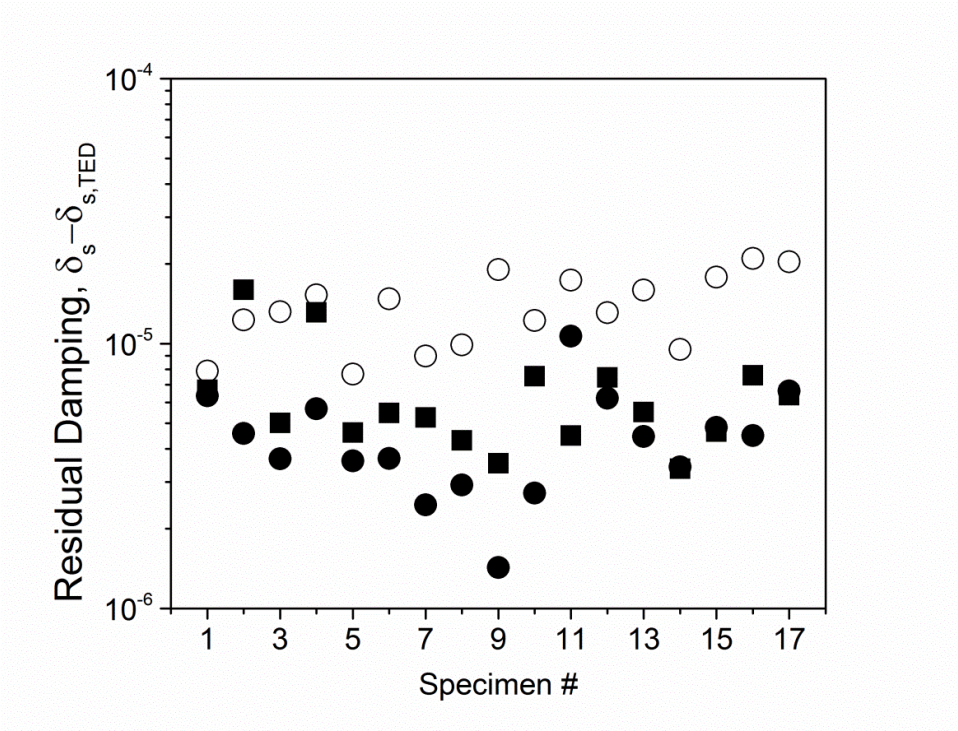

Figure 3.12: The residual damping measured for a set of 17 single-crystal silicon microcantilever beams measured using the BES (squares) and EES (circles). The residual damping for the second mode is plotted in open circles.

Except for Specimen 11, the residual damping measured using the EES is lower than or equal to the BES values. The residual damping for the second mode is greater in magnitude than the first mode. For both modes and both platforms, the residual damping is within expected bounds. Extensive experimental damping measurements on a set of 72 single-crystal silicon microcantilever beams by Sosale revealed that the residual damping is consistently measured at ~10^{-5} [17, 98]. Further, the residual damping was shown to have no correlation to the specimen dimensions [106]. Slight variations that are observed over the specimen set are uncorrelated and random. Therefore, the O(10^{-5}) residual damping level is assumed to be a result of clamping loss and its uniformity is due to the standardized clamping procedure. This agreement indicates that

the design and method of the EES can measure damping to the same minimum level as the BES. However, one other metric of the performance of the EES is the ability to repeat damping measurements.

3.5.3 Evaluating the repeatability of the damping measured with the EES

The repeatability of the damping measurement is a measure of the systematic error. Here, an experimental measurement of the damping is defined as the average of five measurements where the beam has not been unclamped and none of the operating conditions have changed. The standard error of the mean value of five measurements is representative of the effect of random noise on the measured parameters during an experimental session. The repeatability, then, is the precision of an experimental measurement; the repeatability quantifies the effect of the measurement protocol on the damping measurement.

The damping measurement repeatability is experimentally determined for the EES with a set of three specimens chosen at random and measured five times. Each experimental measurement included venting the vacuum chamber and remounting the specimen on the EES. The repeatability for the EES, Table 3-5, is as great as 16% and low as 6%.

Table 3-5: The room temperature repeatability of the EES for three specimens remounted five times on the EES. The error is the range reported as a percentage of the mean.

#			Frequency [Hz]				Logarithmic decrement, δ_s			
	L [mm]	h [μm]	min	mean	max	error	min ($\times 10^{-6}$)	mean ($\times 10^{-6}$)	max ($\times 10^{-6}$)	error
8	15.28	52.63	275.18	280.33	281.64	2.31 %	5.87	6.31	6.87	15.96 %
16	12.65	56.75	449.12	449.16	449.20	0.02 %	10.9	11.4	11.9	8.82 %
17	10.19	54.71	664.63	664.64	664.66	0.01 %	15.7	16.1	16.7	5.94 %

Evaluating the repeatability using eight similar cantilever beam specimens, Sosale reported a precision error as high as 7.05% and as low as 1% for the BES [17]. With respect to this, the repeatability of the EES is poor. However, it must be noted that the operating conditions are not identical. Sosale performed all of the experiments on a vibration isolating optical table

(RP Reliance, Newport Corp, USA) and the experiments using the EES are conducted on a simple wooden table.

Ambient energy from building vibrations and other sources is better able to reach the specimens through the wooden table, thus skewing the measured damping. This effect would also be more pronounced for very high-Q and low frequency resonators because of their increased sensitivity, operating bandwidth, and the increased transmissibility of low-frequency waves. For example, at rest, the high-Q specimens have been observed to be set in motion by noises, such as the door closing. Any evidence of spurious excitation is grounds to eliminate data, but it is hard to detect for a single-shot measurement.

3.6 Summary

The aim of Chapter 3 is to introduce the EES for the measurement of damping and characterize its performance with respect to the well-characterized BES in addition to theoretical measures of damping. First the instrumentation and experimental specimens were explained. Then the method and experimental protocols of electrostatic excitation and the measurement of the logarithmic decrement of free-decay were discussed. This discussion evaluated the effects that the experimental variables (recording time and sampling rate) have on the measurement of damping and introduced a systematic and objective protocol to judge the linearity and consistency of the free-decay data.

The room temperature damping for a set of 17 single-crystal silicon microcantilever beams was measured using the BES and the EES system. Additionally, the damping and resonance frequency was measured at the second mode using the EES. The ratio of the measured first mode resonance frequency to the second mode is not consistent for all specimens. The presence of discrepancies suggests that this measurement can be implemented as a screening tool for damaged specimens or corrupted data.

For the first mode damping, the EES measures a damping level comparable to the BES. Then, in comparison the theoretical TED limit, the residual damping is also proven to be consistent for the set of microcantilever beams. Finally, a study of the measurement repeatability finds that the systematic error due to the clamping causes a precision error as low as 6% and as

high as 16% for the EES, which is greater than the precision error of the BES that is reported by Sosale.

In conclusion, the experimental protocols and the EES instrumentation have been demonstrated to measure the damping with a minimum resolution that is slightly better than the BES system. However, the repeatability study indicates that the EES may suffer from a precision error as high as 16%. Based on a set of three specimens, the precision improves with increasing fundamental resonance frequency. Thus, the specimens that are selected for future studies should have as high a frequency as possible.

CHAPTER 4

Measurement of the effects of temperature on the material damping in silicon based microcantilever resonators

The work in this chapter is an experimental study of the material damping in single-crystal silicon and aluminum coated silicon microcantilevers. The instrumentation, specimens, and experimental protocols described in Chapter 3 are now used to measure the temperature dependence of the material damping. The process starts by calibrating the performance of the EES to the TED limit from room temperature up to 225 ˚C using un-metalized beams. Then a 48 nm thick layer of aluminum is deposited on two different cantilever specimens and the damping is measured from room temperature up to 165 ˚C. The difference between the two measurements is used to calculate the temperature dependence of the internal friction of the aluminum film.

4.1 Measuring damping above room temperature

In this section, the material properties of single-crystal silicon are tabulated in order to estimate the temperature dependence of TED and other damping mechanisms. Then the heating protocol of the clamp is experimentally determined and the damping of a set of single-crystal silicon microcantilever beams is measured and calibrated to the TED limit.

4.1.1 The temperature dependence of the material properties of single-crystal silicon

The mechanical spectroscopy of damping mechanisms is calibrated by using single-crystal silicon microcantilever beam substrates that measure damping close to the TED limit. In theory, for beams satisfying the Euler-Bernoulli beam theory, the accuracy of the theoretical calculation of TED is a few percent [67]. Compared to experimental results, the accuracy of the calibration is contingent on the accuracy of the measured dimensions and material properties.

The literature has been mined for empirically derived formulas and experimental data of the temperature dependence of the material properties of single-crystal silicon. This information

is listed in Table 4-1. When the model does not reflect the experimental measurements of the material properties, the model is re-fit to find new constants.

Table 4-1: Mathematical models for the temperature dependence of the material properties of single-crystal silicon have been fit to experimental data to find optimal values of the constants. All of the constants are from the literature except for the model of C_v, which is from [194] and was independently fit to the data of [189, 194-196].

Model	Constants	Reference
$k = k_0\left[1 - A\left(\frac{T - T_0}{T}\right)^B\right]$, [W/m/K]	A = 1.093, B = 1.56×10^{-3} k_o = 144.19 W/m/K, T_o = 298.25 K	[197]
$C_v = \left(A + BT + \frac{C}{T^2}\right)$, [J/m^3/K]	A = 1.763×10^{6} B = 1247.0, C = -8.425×10^{7}	[189, 194-196]
$\alpha = \mathrm{A} + B\frac{e^x x^2}{(e^x - 1)^2} + C\frac{(y-1)^2}{1 + Dy}$, [1/K]	A = -0.687×10^{-6} B = 5.0×10^{-6} C = 0.22×10^{-6} D = 0.316, x = Θ_E/T, y = Φ_o/T Θ_E = 685 K, Φ_o = 395 K	[198]
$\rho(T) = \rho_o(1 + \dot{\rho}(\Delta T) + \ddot{\rho}(\Delta T)^2 + \dddot{\rho}(\Delta T)^3)$, [kg/m^3]	$\rho = 2333$ kg/m^3 $\dot{\rho} = -8.5 \times 10^{-6}$ $\ddot{\rho} = -25.5 \times 10^{-9}$ $\dddot{\rho} = 95.3 \times 10^{-12}$	[199]
$E_{110} = \left(s_{11} - \frac{1}{2}\left[(s_{11} - s_{12}) - \frac{1}{2}s_{44}\right]\right)^{-1}$, [N/m^2]	At T_o = 298 K s_{11} = 7.68×10^{-12} s_{12} = -2.14×10^{-12} s_{44} = 12.58×10^{-12}	[188, 200]
$s_{ij}(T) = s_{ij}(T_0)\left[1 + \sum_{k\geq 1} TCE(s_{ij})_k (T - T_0)^k\right]$	Temperature Coefficient of Elasticity, TCE(s_{ij})	
	ij: 11 / 12 / 44	
	$\dot{s}_{ij}$: 64.7 × 10^{-6}/°C / 51.4 × 10^{-6}/°C / 60.1 × 10^{-6}/°C	[199]
	$\dot{s}_{ij}$: 52.4 × 10^{-6}/°C / 44.0 × 10^{-6}/°C / 29.4 × 10^{-6}/°C	[201]
	$\ddot{s}_{ij}$: 61.1 × 10^{-6}/°C / 72.2 × 10^{-6}/°C / 54.9 × 10^{-6}/°C	[199]

The temperature dependent material properties are plotted in Figures 4.1 and 4.2 in relation to the experimental data.

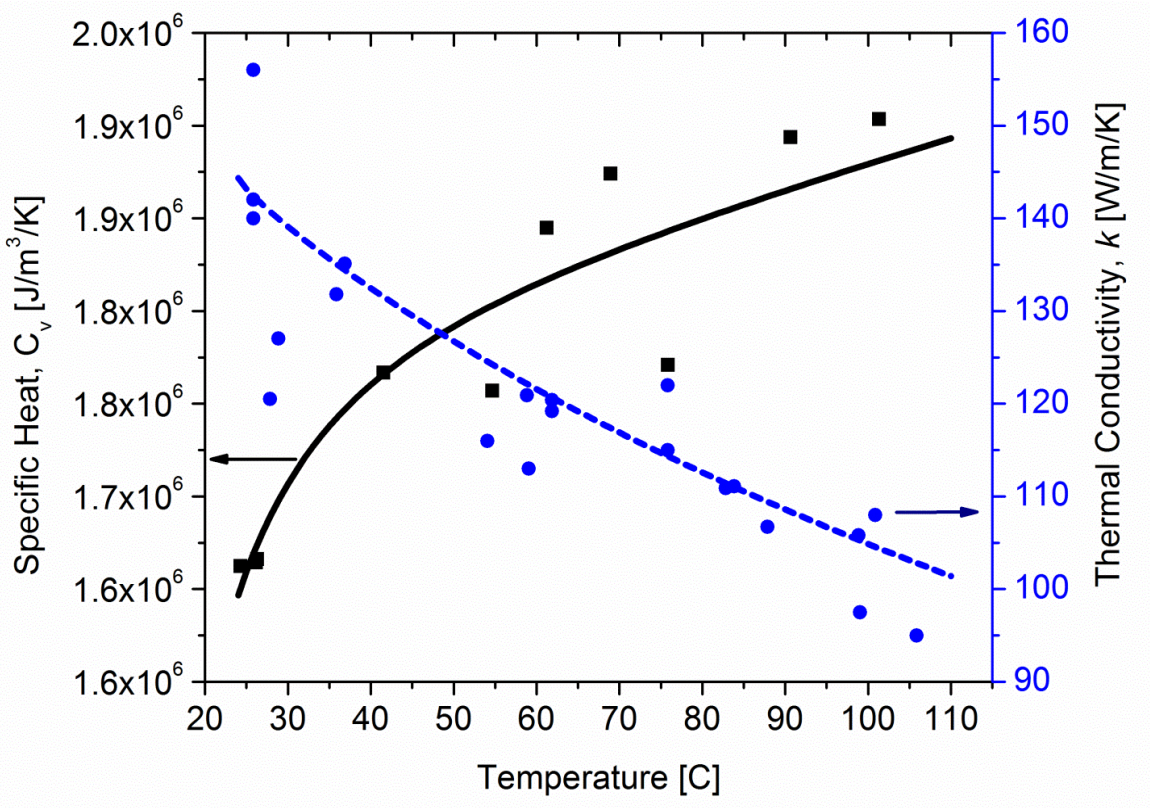

Figure 4.1: The temperature dependence of the specific heat (black line) is compared to experimental data (black squares) of [189, 194, 196] and corresponds to the left vertical axis. The temperature dependence of the thermal conductivity (dashed blue line) is compared to experimental data (blue circles) of [202-207] and corresponds to the right vertical axis.

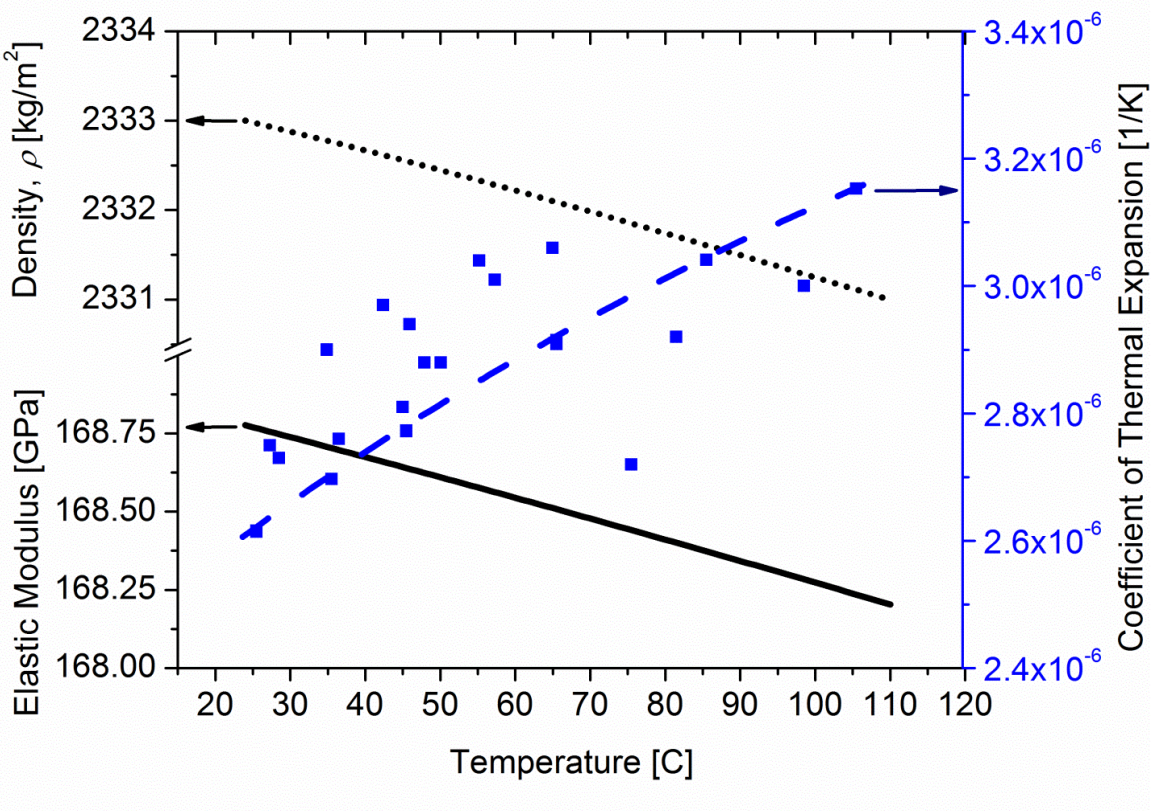

Figure 4.2: The temperature dependence of the elastic modulus (solid black line) corresponds to the left vertical axis below the break. The temperature dependence of the density (dotted black line) corresponds to the left vertical axis above the break. The temperature dependence of the coefficient of thermal expansion (dashed blue line) is compared to experimental data (blue squares) of [189, 208-211] and corresponds to the right vertical axis.

The material damping can now be estimated using the temperature dependent models of the material properties of single-crystal silicon. For all of the specimens and from room temperature to 100 ˚C, the Akhiezer damping is on the order of 10^{-7} and is less than the TED. Theoretically, the support loss has no temperature dependence. However, the thermal expansion of the clamp may affect the clamping loss. By building a library of the temperature dependence of the material properties of single-crystal silicon, the temperature dependence of the residual damping can be determined experimentally.

4.1.2 Heating protocol for the EES

Reaching a specific temperature with accuracy and maintaining stability is difficult. In vacuum, due to large temperature gradients and non-uniform heat loss, automated control by PID

algorithms is not possible. Hence, the heating protocol has been developed experimentally based on observations of heating and cooling behavior.

When heated above 50 ˚C, the temperature measured by the thermocouples at the clamping surface and the clamping plate is offset from the heater temperature due to conduction time and a non-uniform rate of heat loss by radiation. The temperature offset increases linearly with the increasing temperature of the heater. Thus, the EES is effectively separated into three zones (the heater, the base of the beam, and the clamping plate). The control of the temperature at the base of the beam must take into account the offset.

The temperature of the heater is controlled with an on-off thermostat and by matching the power supplied to the heater with the power lost to radiation and conduction. The control of the heating power and thermostat for each temperature increment follows a certain protocol:

1. The on-off thermostat is set at a +3 ˚C offset from the target beam temperature. Above 90 ˚C the heater thermostat set point offset needs to be increased by +1 ˚C for every additional 5 ˚C temperature increment.
2. The heater is "soaked" at a power that is greater than the power necessary to equilibrate the system against the heat lost.
3. The thermostat turns off the heater when the set-point temperature is reached.
4. The power supply is dialed back to a "stabilize level."
5. The heat is allowed to conduct from the heater to the rest of the clamp.
6. A measurement can begin when the temperature of the beam is at the target set-point.
7. The on-off thermostat keeps the temperature stable while a damping measurement is made.

The "soak" and "stabilize" power levels for every heating increment from room temperature up to a temperature of 225 ˚C are given in Figure 4.3. This plot also shows how the measured temperature offset at each location increases as a function of the heating increment.

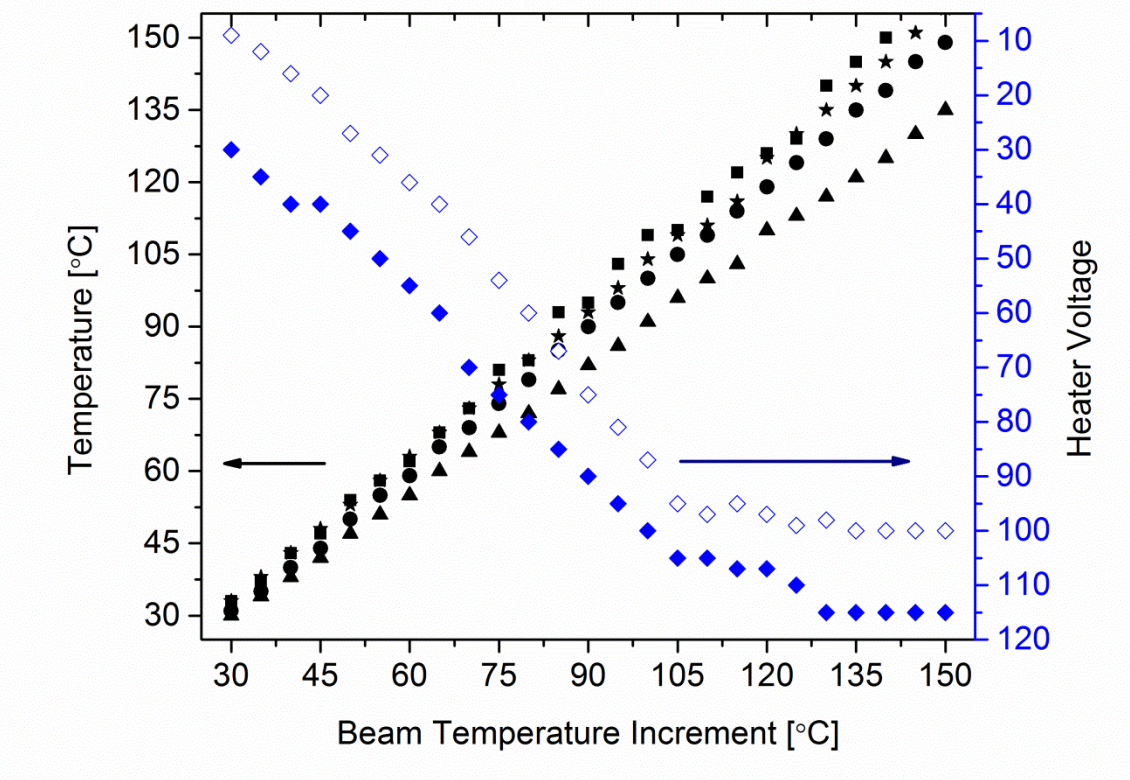

Figure 4.3: The temperature profile of the clamp and voltage settings are plotted as a function of the temperature at the base of the microcantilever beam. The temperature profile of the clamp is measured at the clamping surface (black circles), the heater (black squares), and the top of the clamp (black triangles). The temperature at the beam is determined by the temperature set-point (black stars) of the heater and the voltage supply (blue diamonds). Approaching a given set-point (stars), the heater is supplied with a soak voltage (blue closed diamonds) and is then dialed back to a stabilizing voltage (blue open diamonds) when the heater temperature surpasses the set-point.

Stabilizing the temperature becomes increasingly difficult at higher temperatures. Despite careful operation, the temperature has been observed to change while making five measurements of the damping at a particular temperature increment. Thus, the checks for non-linear damping introduced in Section 3.4.4 are essential to screen for experimental errors. Through the use of the established consistency check, at times, the damping has been observed to fluctuate despite the thermocouple indicating a stable temperature. This indicates that there is an additional unknown heating lag between what the specimen feels and what the thermocouple at the base of the beam measures

4.1.3 The damping of single-crystal silicon microcantilevers above room temperature (25˚C to 225˚C)

Using this heating protocol, the damping and resonance frequency of a pure, single-crystal silicon microcantilever beam is measured from room temperature up to 225 ˚C in 10 ˚C increments. At each temperature increment, the damping is measured five times and then averaged. Specimen 17 has been selected for this study due to its demonstrated low-damping and acceptable repeatability. The measured damping is plotted in Figure 4.4 against the TED limit.

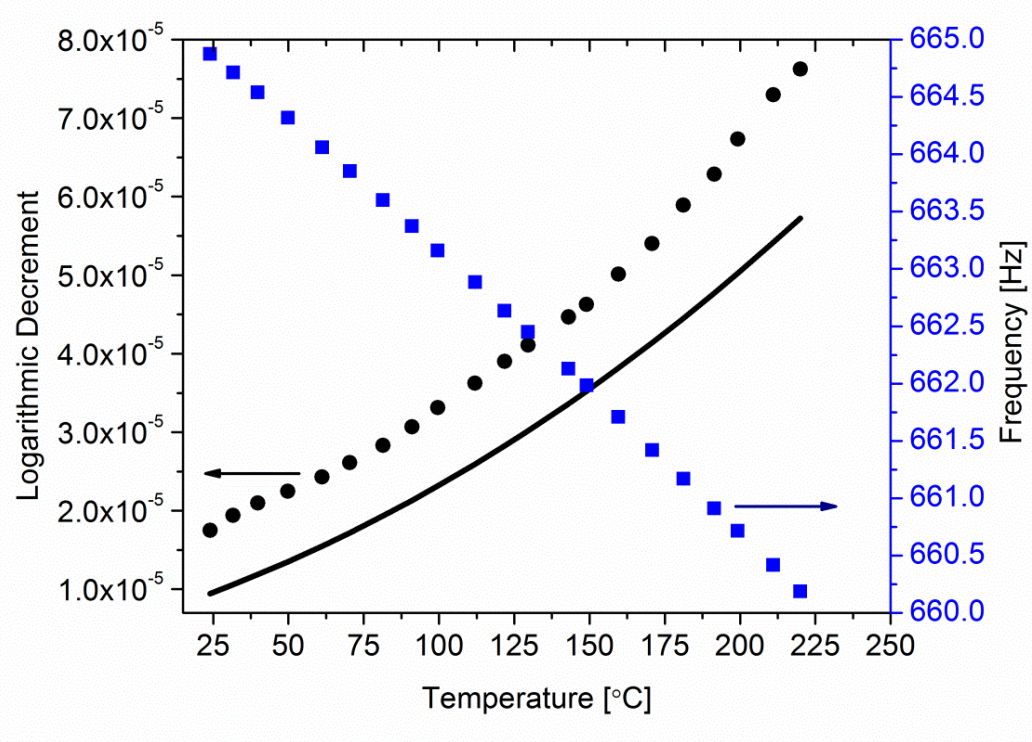

Figure 4.4: The damping (black circles) and resonance frequency (blue squares) of Specimen 17 is measured from room temperature to 225 ˚C in increments of 10 ˚C. The measured damping is plotted against the TED limit (solid black line).

The measured resonance frequency decreases linearly with increasing temperature and the damping increases. The behavior of the measured damping is compared to the temperature dependence of the TED. The residual damping plotted as a function of temperature (Figure 4.5) increases slowly up to 150˚C. Above 150˚C, the magnitude of the residual damping increases at a faster rate.

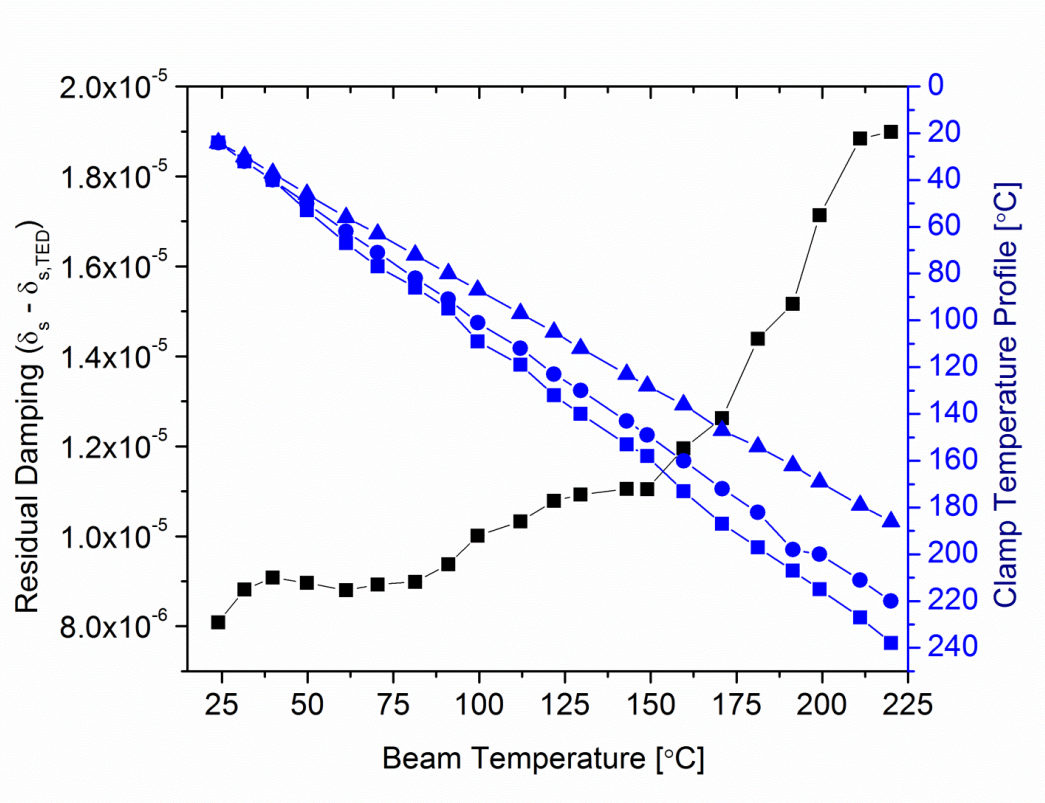

Figure 4.5: On the left vertical axis, the residual damping for Specimen 17 is plotted (black squares) against the temperature measured at the clamping surface. On the right vertical axis, the temperature profile of the clamp is plotted for each temperature increment. The temperature measured at the heater is plotted as blue squares, the base of the beam is blue circles, and the clamping plate is blue triangles.

Over the course of the experiment, the temperature gradient of the clamp is growing. The temperature gradient is assumed to be correlated to the increasing residual damping based on two other observations:

1. The residual damping is sensitive to the clamping pressure [17].
2. The damping has been observed to fluctuate when the temperature shifts during the recording of the free-decay.

This preliminary measurement shows that the resolution of the system erodes at high temperatures. Up to 150˚C the residual damping is still $\delta_{residual} < 1 \times 10^{-5}$, which is within prescribed tolerances. The next step is to probe the repeatability of the measured damping as a function of temperature.

Specimens 16 and 17 are selected for this detailed study of the temperature dependence of damping in single-crystal silicon microcantilever beams. The damping is measured over a range of temperatures in an unbroken series. This protocol was performed five times for both specimens and each experimental session consists of venting the chamber, cooling the system, and remounting the beam. The temperature increment was reduced to 5 ˚C for two sessions to determine if the heating regime affects the damping trend. The measured damping for Specimen 17 and Specimen 16 are plotted against the TED limit in Figures 4.6 and 4.7 respectively.

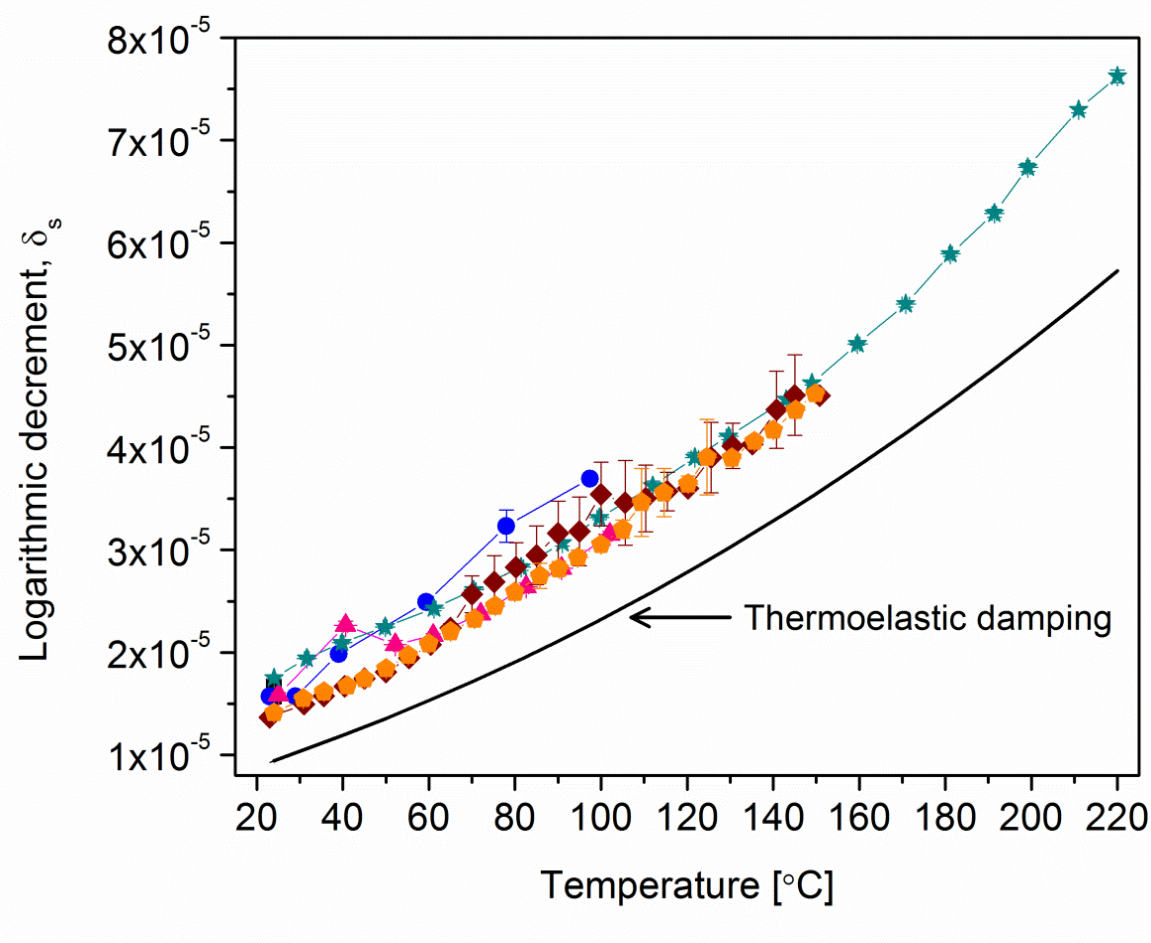

Figure 4.6: The damping of Specimen 17 is measured as a function of temperature in five separate experiments. The error bars represent the standard deviation of five measurements of the damping at each temperature increment. The solid line denotes the TED limit. The solid black squares are the measurements of damping taken at room temperature from preliminary studies.

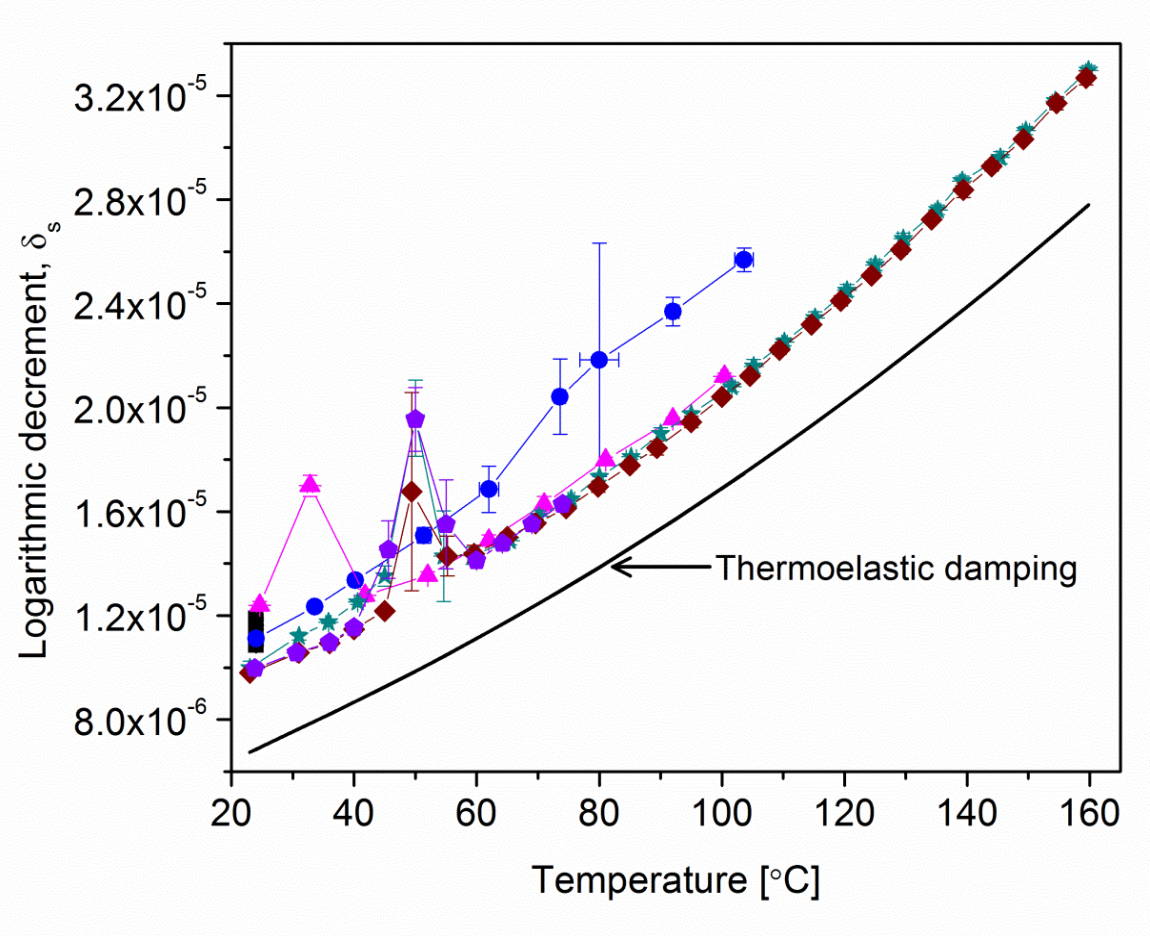

Figure 4.7: The damping of Specimen 16 is measured as a function of temperature in five separate experiments. The error bars represent the standard deviation of five measurements of the damping at each temperature increment. The solid line denotes the TED limit. The solid black squares are the measurements of damping taken at room temperature from preliminary studies.

First, for both specimens, within an experimental session, certain data points depart from a smooth increase in damping as the temperature is increased. These occurrences are random and are accompanied by a greater measurement standard deviation. Second, the standard deviation of five measurements can be great, even though the damping was not observed to change during the recorded free-decay and the temperature did not breach the ± 1 ˚C stability threshold for the measurement at a single temperature increment. Third, the size of the temperature increment does not affect the trend of the residual damping. Fourth, precisely replicating an experiment is difficult due to the manual heating control.

These observations suggest that each experimental session is unique because of the random fluctuation of the clamping loss and the manual heating protocol. Then, to use the single-crystal silicon microcantilever beams as a substrate for the mechanical spectroscopy of material damping, multiple measurements need to be performed to generate an average base-line level for the temperature dependence of the material damping of single-crystal silicon.

4.2 Measuring the material damping in aluminum coated silicon microcantilevers

In the previous section, the temperature dependence of two single-crystal silicon microcantilever beams has been measured up to 160 ˚C. Now Specimen 16 and 17 are coated with 47.8 nm and 47.9 nm of aluminum, respectively, deposited on the cantilever portion of the beam using an electron beam evaporator (Temescal BJD-1800). This is achieved by masking the base of the beam with a custom designed molybdenum clamp. Prior to deposition, the specimen is cleaned using Piranha etchant and DI water. The e-beam deposition is controlled with the electron gun voltage, sweep pattern and amplitude. The deposition rate is automatically measured by the machine and the exposure time is adjusted to deposit the defined film thickness. The deposition rate of aluminum with the voltage at 9 kV, the pressure less than 2×10^{-6} Torr, and the sweep pattern in a figure-8 is 2 Å/s. The target film thickness was 38 nm but the final film thickness measured with a scanning profilometer (Tencor P1 Profilometer) was found to be thicker. The discrepancy is likely caused by opening the crucible shutter for too long while aligning the e-beam. Upon exposure to atmospheric conditions, the aluminum films become covered with a native oxide layer that ranges from 3 nm to 5 nm in thickness.

The damping of the metalized beams is measured as a function of temperature in 5 ˚C increments and is plotted in Figures 4.8 and 4.9 for Specimens 16 and 17 respectively. The addition aluminum on a single-crystal silicon microcantilever increases the damping relative to the bare beam and the TED limit. The temperature dependence of the damping of the metalized beam does not increase at the same rate as the damping of the pure single-crystal silicon microcantilever. This trend suggests that there is a temperature dependent internal friction peak. The next step is to condition the composite damping data. Removing outlier data points will improve the measurement of the material damping in the aluminum film.

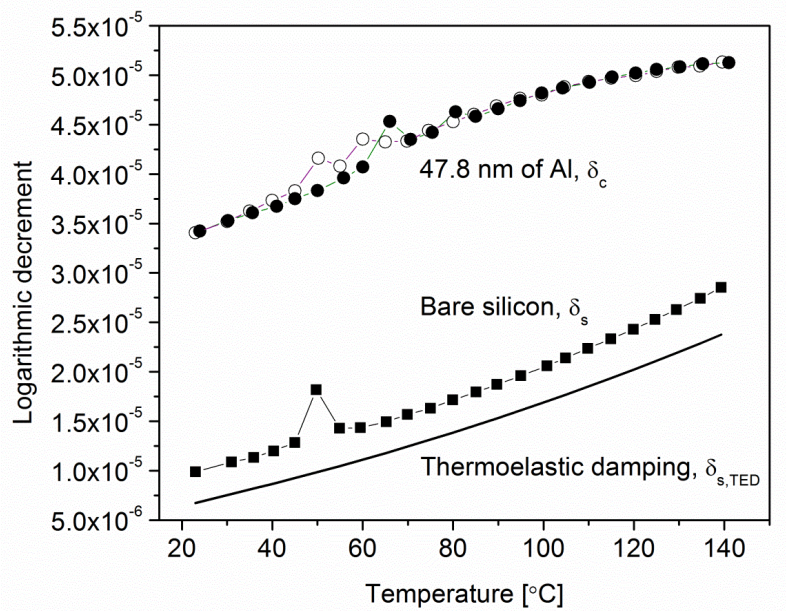

Figure 4.8: The damping of a composite microcantilever beam, Specimen 16 coated with 47.8 nm of aluminum (squares), bare single-crystal silicon beam (black circles), and the TED limit (black line) are plotted against the temperature.

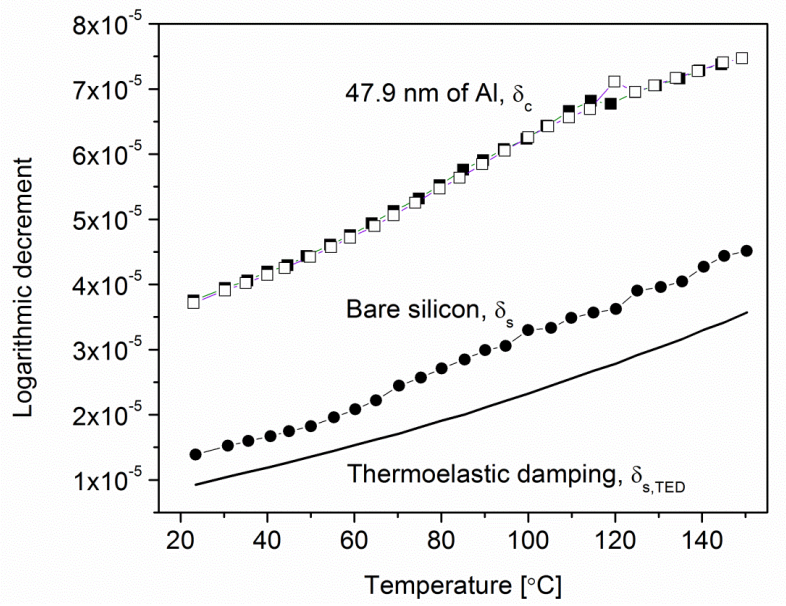

Figure 4.9: The damping of a composite microcantilever beam, Specimen 17 coated with 47.9 nm of aluminum (squares), bare single-crystal silicon beam (black circles), and the TED limit (black line) are plotted against the temperature.

4.2.1 Identification and removal of outlier data points in the measurement series

The damping of the composite microcantilever is assumed to gradually increase with increasing temperature. Yet, contrary to this expectation, some data points measure lower damping values than the preceding points, suggesting that the preceding point is an outlier. These outlier points are more numerous for Specimen 16 between 50 ˚C and 80 ˚C. For Specimen 17, there is an aberration around 110 °C. This poses two questions:

1. As each data point is the average of five measurements of the damping, are the points that deviate from the general trend influenced by outliers within the five measurements that are averaged?
2. Can the points that deviate from the general trend be systematically identified as outliers?

The first question is answered by plotting, in Figure 4.10, the entire damping data sets of the metalized Specimen 16. The full data sets reveal that the averaged data points are displaced by extreme outlier points.

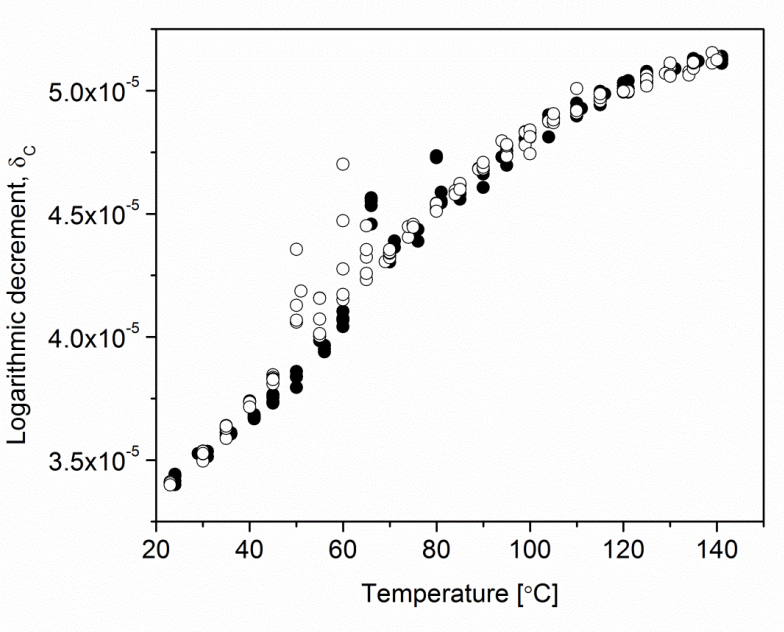

Figure 4.10: The full data sets of the measured damping of Specimen 16 coated with 47.8 nm of aluminum. In this plot, the full five measurements of the damping collected at each temperature increment are shown.

The next question calls for a systematic and objective protocol to identify and remove outlier data points from the data. To begin, the terminology is defined. The term "data set" is referring to all of the measurements of the damping in a single "experimental session". Each "experimental session" is a separate mounting and starts at room temperature and incrementally increases in temperature without interruption. An "averaged data point" will be referring to the average of multiple damping measurements at one temperature increment. Then, "data point" will refer to a single measurement of the logarithmic decrement within a given averaged data point. The objective is to identify individual data points as outliers as opposed to averaged data points in a bid to preserve information.

According to the *NIST e-Handbook of Statistical Methods*, an outlier is defined as "an observation that appears to deviate markedly from other observations in the sample" [212]. Identifying outliers depends on the distribution of the data. Commonly used data analysis tools, such as the Grubb's test (for one outlier) and the Generalized Extreme Studentized Deviate test (for multiple outliers), assume a normal distribution. Normally distributed data has a random orientation about the mean. Such tests cannot be used to answer the first question because, collectively, the mean is a function of the temperature. Alternatively, to analyze the variance of this population, the outliers may be identified based on their deviation from a best fit line to the scatter plot of the full data set. This is a subjective test, though, because the presence of outliers themselves affects the best fit line. To introduce an element of objectivity, a custom procedure based on exploratory data analysis (EDA) will be developed and implemented to identify and eliminate outlier data points.

Exploratory data analysis is the combination of statistical and graphical methods to characterize data. As opposed to purely statistical methods, EDA is not used for hypothesis based testing. EDA is an approach to interpret data and can help expose the structure of the data, uncover biases, detect anomalies, identify proper data modeling functions, and ultimately improve one's insight into the nature of experimental data [212]. From this perspective, EDA methods will be implemented to find the outlier data points in the damping data for the metalized microcantilever beams.

The aim is to develop an approach that can be applied to any data set to verify presence of random measurement errors. The subjective tools of the EDA methods will be deployed in tandem with an objective systematic procedure to eliminate outlier data points. The EDA will be applied to the full data sets instead of using the averaged data points in each data set. Next, some assumptions regarding the nature of the underlying process must be made. This is a necessary exercise because there is no empirically derived model to predict the damping in aluminized microcantilever beams as a function of temperature to which the experimental data can be compared.

The damping of a bare single-crystal silicon microcantilever beam is a combination of several processes. The most dominant damping mechanisms for the microcantilever beams, determined experimentally at room temperature, are TED and clamping losses. According to the temperature dependence of the material properties, the TED increases as a function of temperature. A model of the clamping loss contribution is not available, but it is experimentally determined , at room temperature, to be relatively constant at $O(10^{-5})$ for the clamp that is used in this experiment [106].

Initial studies of the damping of pure single-crystal silicon microcantilever beams revealed that the residual damping slowly increases with temperature up to 150˚C, suggesting that the clamping loss is weakly temperature dependent. This hypothesis is supported by the fact that the temperature gradients of the clamp become greater at higher temperatures, slowly changing the clamping pressure exerted on the base of the microcantilever. Further, it is assumed that the clamping loss is inherently random, the increase with temperature is slight, and the overall magnitude is small with respect to the TED and the material damping contribution of the bi-layer beam. While the temperature dependant increase in the residual damping does factor in as a source of measurement inaccuracy, it is assumed not to contribute to outlier data points. It is also assumed that, given a stable temperature at each measurement increment, the change in the clamping loss is small with respect to the previous temperature increment and proportional. But if the temperature fluctuates and the clamping pressure is changing during one measurement, then the standard deviation of an averaged data point will be affected. Then, based on the position of a single data point relative to the rest of the data set, an outlier can be identified.

This proposed outlier identification scheme relies on some key assumptions. The first assumption is that, for a perfect heating regime, the clamp is at a stable temperature for each temperature increment and the standard deviation for every averaged data point is 1%. Thus, the damping of the composite microcantilever beam is assumed to have a gradual temperature dependency where the standard deviation of any averaged data point from the overall trend would ideally be 1% also. That is, the damping at one temperature can be estimated from the damping measured at the previous temperatures.

With the assumption that one data point depends on the other (strong autocorrelation) and the assumption that the errors are random (error ~1% for an experimental session), the data can be analyzed for outliers by applying a simple model to the data set. Regression analysis will be used to evaluate the model in terms of the presence of outliers. The quality of the fit and the identification of outliers are determined by the six-plot method, which is a graphical EDA method for process modeling. The 6-plot is a collection of six graphical techniques that help one assess the fitting function by an examination of the residuals. The graphs and their interpretation are explained as follows:

1. The scatter plot of the data points with the overlay of the fitting function is a simple tool to visually assess the goodness of the fit.
2. A plot of the residuals versus the independent variable can indicate if the residuals are random or correlated.
3. The lag-lag plot of the residuals can reveal outliers as well as the randomness of the residuals.
4. The histogram of the residuals can show outliers as well as whether the residuals distribution is normal.
5. The normal probability plot shows the probability distribution of the residuals.

The fit is determined to be good if the scatter plots of the residuals do not have a trend and the residuals are evenly distributed. Further, the residuals should be randomly distributed in the lag-lag plot and have a normal probability distribution. At this point, the six-plot method is still a subjective tool. To remove the element of interpretation, automation is introduced by

associating outlier points with their fitting residual. The systematic regression analysis routine will follow these steps:

1. Fit a polynomial function and use the 6-plot EDA technique to evaluate the residuals and identify the outliers.
2. Eliminate the outliers and repeat.

This routine is continued until the standard error of the residuals is less than one percent. The outliers of the first fit are eliminated if the fitting error exceeds 2%. The error threshold for the second fit is 1.5% and all subsequent fits use a 1% fitting error threshold. At each step, the 6-plot results are used to ensure that the fitted function well represents the data.

An example of the final 6-plot regression analysis, after four fitting iterations of a cubic polynomial, is plotted in Figure 4.11. The lag-lag plot shows a weak correlation and the distribution of the residuals is normal. The application of this analysis removed some averaged data points entirely and left others with one or two data points. The culled data set, S16HF5, is plotted in Figure 4.12 and the number of data points in each averaged data point is given if it is not five. The culled data sets are then used to analyze the material damping of the composite specimens.

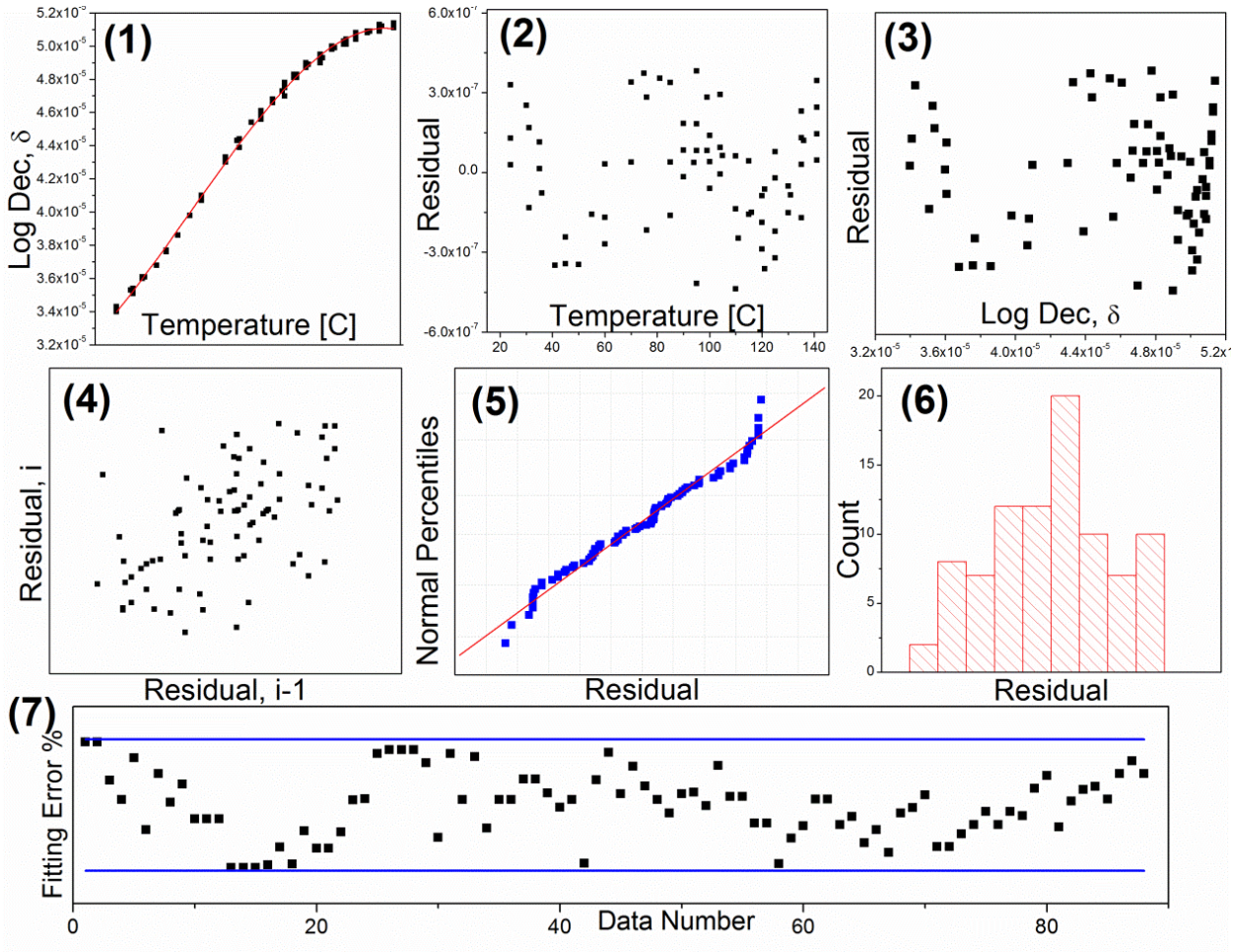

Figure 4.11: The 6-plot analysis of a cubic polynomial fit to the S16HF5 data set is graphed in the top six windows. Clockwise from the top left corner is the scatter plot of the data with the fitted line, the residuals plotted against the independent variable, the residuals plotted against the dependent variable, the lag-lag plot of the residuals, and the histogram of the residuals. The bottom plot is the standard error of the residuals where the horizontal solid blue lines are the ± 1% threshold for the residuals that is used to cull outlier data points.

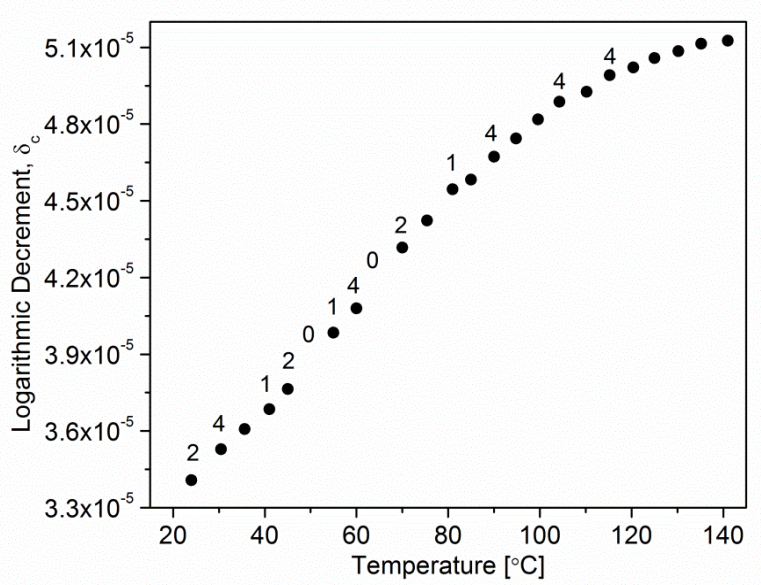

Figure 4.12: The data set S16HF5 of the composite microcantilever Specimen 16 has been culled of outliers. The remaining data points for each averaged data point are labeled. Averaged data points with no label have retained all five damping measurements.

4.2.2 Material damping of the aluminum film

The material damping in the aluminum film is a contribution of TED, Akhiezer damping, and internal friction. For very thin films, it has been shown that the contribution of the first two mechanisms is negligible with respect to the internal friction [18, 98]. The internal friction of the aluminum film is calculated by comparing the damping of the bi-layer beam, δ_c, to the TED. When the film thickness, h_f, is significantly less than the thickness of the microcantilever beam substrate, h_s, ($h_f \leq 0.01 h_s$), the TED of the composite beam is essentially equal to the TED of the non-metalized beam [98]. Therefore, the internal friction is [17]

$$\delta_{IF} = \frac{E_{Si} h_s}{3 E_{Al} h_f} \left(\delta_c - \delta_{s,TED} - \delta_{residual} \right). \tag{4.2}$$

Alternatively, the experimentally measured substrate damping, δ_s, can be used and the internal friction may be calculated by [97]

$$\delta_{IF} = \frac{E_{Si} h_s}{3 E_{Al} h_f} (\delta_c - \delta_s). \tag{4.3}$$

The composite damping cannot be directly compared to the damping of the bare specimen due to the discrete temperature increments. Therefore, the substrate damping is approximated with a model function to create seamless representations of the EES system level damping for Specimens 16 and 17 as a function of temperature.

This is accomplished by fitting quadratic equations to the damping of the bare single-crystal silicon microcantilever beams. For Specimens 16 and 17, the data sets with the greatest temperature resolution are chosen. Two temperature sets for Specimen 16 and three temperature sets for Specimen 17 are selected and fit in Figures 4.13 and 4.14 respectively. Outlier data points in the data for Specimen 17 have been removed due to an anomalous peak in damping around 50 ˚C.

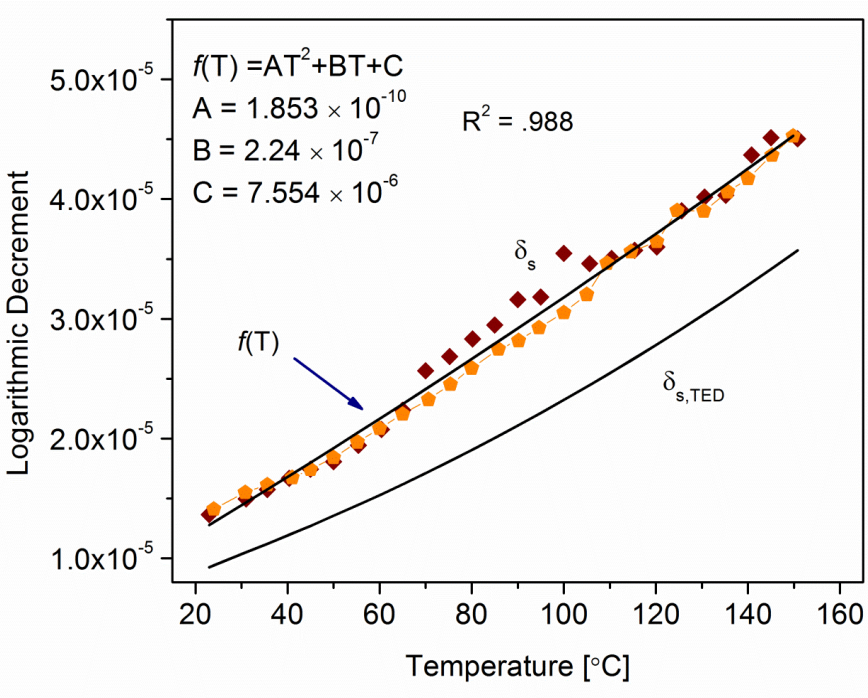

Figure 4.13: The damping of the bare Specimen 17 is fit with a quadratic equation.

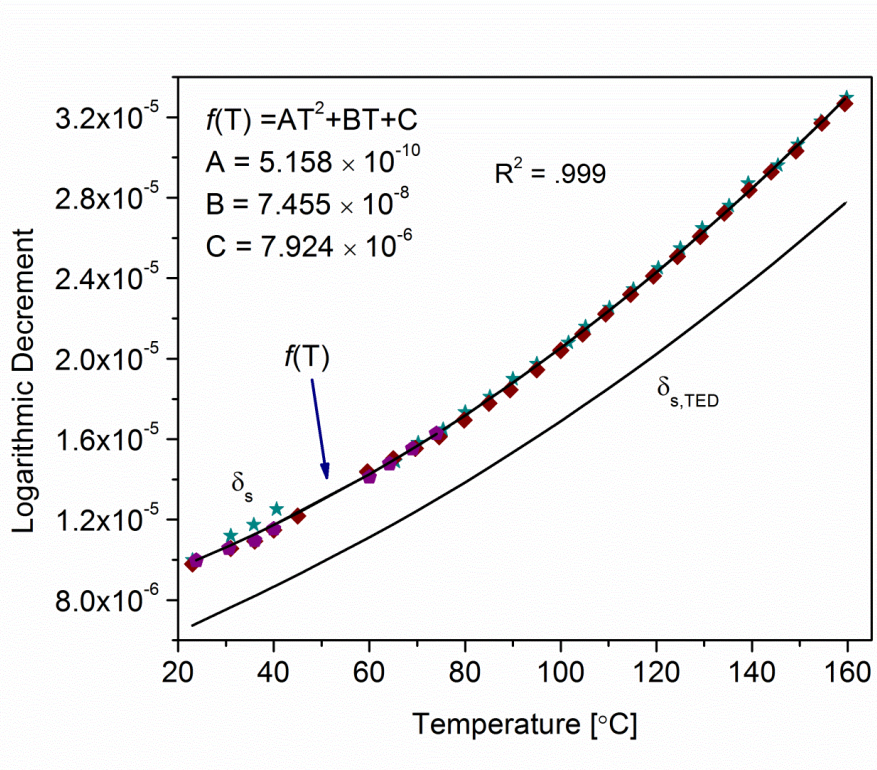

Figure 4.14: The damping of the bare Specimen 16 is fit with a quadratic equation. The data points at 50 ˚C and 55 ˚C where identified as outliers and removed before the fitting.

These quadratic functions are a better approximation than simply adding an offset to the TED limit to account for the clamping loss; the functions reflect the temperature dependence of the damping of single-crystal silicon substrate and also captures the temperature dependence of the clamping loss of the EES. Using these functions and Equation 4.3, the internal friction of the aluminum films is extracted and plotted in Figure 4.15 and 4.16.

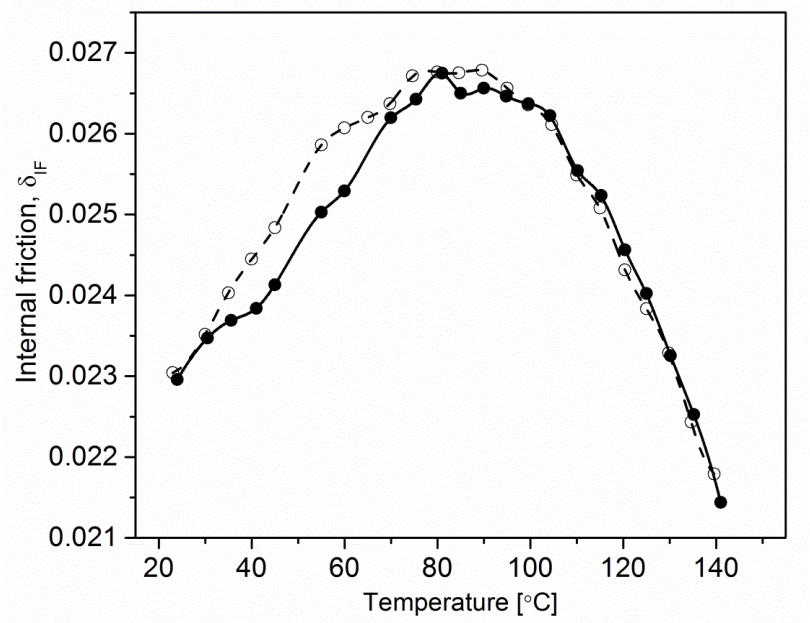

Figure 4.15: The temperature dependence of the internal friction of 47.8 nm of aluminum coated onto Specimen 16.

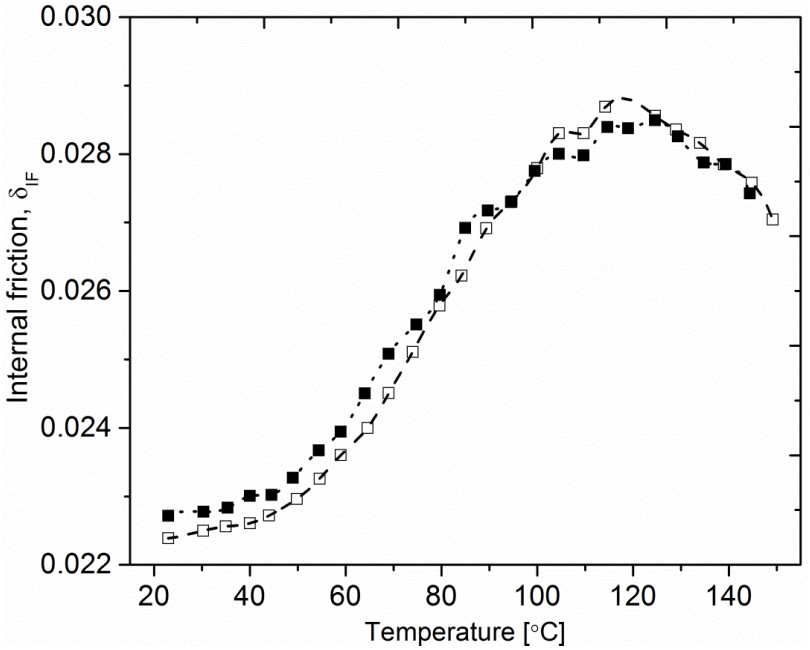

Figure 4.16: The temperature dependence of the internal friction of 47.9 nm of aluminum coated on Specimen 17.

The internal friction increases, peaks, and then decreases. The temperature at which the peak occurs is not the same for both samples, but the magnitude is in good agreement. Future work entails finding the mechanical origins of the internal friction peak by extending the frequency range of the microcantilever substrates.

4.3 Summary

The framework for measuring the damping of microcantilever beams, presented in Chapter 3, has been extended to measure the damping as a function of temperature. Specimens 16 and 17 are used to characterize the temperature dependence of damping for single-crystal silicon microcantilever beam resonators. A literature survey and compilation of the temperature dependence of the material properties of silicon have been compiled in order to calibrate the damping measurements to the TED limit. The comparison of the experimentally measured damping to the TED shows that the EES system exhibits a slight temperature dependent clamping loss. The residual damping is still $O(10^{-5})$ for temperatures up to 150˚C, which is within acceptable bounds.

The next achievement was to measure the temperature dependence of the internal friction of thin films of aluminum. This is accomplished by coating Specimens 16 and 17 with ~48 nm of aluminum using e-beam evaporation. Then the damping of the composite beam is measured from room temperature up to 150 ˚C. A systematic and objective method is introduced to remove single data point outliers from the full data sets. Then, by comparing the damping measured for the bare single-crystal silicon microcantilever beam to the composite beam, the internal friction of the aluminum film is calculated. The internal friction of aluminum exhibits a temperature dependant peak. Future work is necessary to understand the mechanisms that cause the internal friction peak.

CHAPTER 5

Measuring the damping of microcantilever beams using the thermomechanical noise[1]

This chapter evaluates the method by which the TMN is measured using a laser Doppler vibrometer and the damping is extracted. First, the theoretical foundations of the TMN are presented. Then the systematic methodology to measure the TMN and extract the damping is explained. The measured damping by this method is compared to the damping measured using the free-decay technique. The comparison allows for an objective critique of the accuracy and precision of this damping measurement method.

5.1 Theoretical foundations of the thermomechanical noise

The TMN can be understood by considering the process of energy dissipation. When vibration energy is converted into heat due to dissipation, the thermal energy is transferred to the microscopic degrees-of-freedom of the thermal reservoir in order to maintain an equilibrium temperature. Then, in the absence of perturbation, the thermal energy is randomly transferred into the resonator from the thermal reservoir. The path of heat transfer is provided by the dissipative element of the resonator, which is a central tenant of the Fluctuation-Dissipation Theorem [15, 157, 158]. Despite the maintenance of an equilibrium temperature, the thermal energy is non-uniformly distributed [213]. The stochastic transfer and distribution of thermal energy drives the Brownian motion in the molecules of the resonator, which is felt as a white-spectrum force by the aggregate. This thermal noise force is manifest in the random displacement of the aggregate structure. The kinetic energy of the displacement is described by the Equipartition Theorem, which states that each energy storage mode has a mean energy equal to $\frac{1}{2}k_B T_o$ [15]. The expression of the induced displacement, the thermomechanical noise, is stipulated by the form of damping [14].

[1] This chapter is an expanded version of the work published in the following article: O. Kuter-Arnebeck, A. Labuda, S. Joshi, K. Das, and S. Vengallatore, "Estimating damping in microresonators by measuring thermomechanical noise using laser Doppler vibrometry," *Journal of Micromechanical Systems*, vol. 23, pp. 592-599, 2013.

There are several equivalent ways to express the displacement of a resonator due to TMN [187, 213]. For a derivation from first principles see Joshi [213]. Here, the approach of Saulson [14] and Levin [214] is followed. The resonator is considered to be a cantilever that is well approximated as a simple harmonic oscillator with one degree of freedom. The dynamics are described by the equation of motion

$$M\ddot{y} + c\dot{y} + Kx = F_{th} \tag{5.1}$$

where *y(t)* is the displacement at time *t*, *K* is the spring constant, *M* is the mass, *c* is the damping of the structure or medium, and F_{th} is the thermal force. In this case, the damping is independent of frequency, a characteristic of viscous damping, so that $Q = \sqrt{MK}/c = 2\pi M f_n/c$ [94]. The resonance frequency is related to the stiffness and the mass by $f_n = (1/2\pi)\sqrt{K/M}$.

Alternatively, the second term can be removed from Equation 5.1 and the damping included as a complex spring with stiffness $K^* = K[1+i\varphi(f)]$. The real and imaginary parts of K^* represent the elastic and dissipative response, respectively. Accordingly, two cases are of particular interest for MEMS: (1) the *Kimball-Lovell solid* with φ independent of frequency [94], which is a good approximation over many decades of frequency for certain types of attachment losses, internal friction due to defect-induced anelasticity [87, 97]; and (2) the *Zener solid* (also called the *standard anelastic solid*) with a single relaxation peak of the form [94]

$$\varphi(f) = \Xi \frac{2\pi f\tau}{1 + (2\pi f\tau)^2} \tag{5.2}$$

where Ξ and τ are the characteristic relaxation strength and relaxation time, respectively. Examples of damping mechanisms that exhibit a relaxation peak include thermoelastic damping in monolithic beams [94], Akhiezer damping [84], and Gorsky damping [99].

The solution of Equation 5.1 for the displacement is characterized in the frequency domain using the power spectrum for mathematical convenience and because the thermal force is a stationary stochastic process [148]. Thus, the Fourier transform of *y(t)* to *Y(f)* is used to denote the one-sided PSD of the displacement as $S_y(f) = 2|Y(f)|^2$ in units of m^2/Hz. The PSD of the TMN is

$$S_y(f) = \frac{k_B T}{\pi^2 f^2} |\Re[G(f)]|, \tag{5.3}$$

where *G(f)* is the mechanical admittance and $\Re$ denotes the real part of a complex function. The admittance is obtained from Equation 5.1 converted to the frequency domain, so that

$$G(f) = i2\pi f \frac{Y(f)}{F_{th}}. \tag{5.4}$$

For the condition of viscous damping the solution of Equation 5.3 is

$$S_y(f) = \frac{2k_B T}{\pi K f_n} \frac{\left(1/Q\right)}{(1-\Omega^2)^2 + \left(\frac{\Omega}{Q}\right)^2} \tag{5.5}$$

And for the complex spring model the solution is

$$S_y(f) = \frac{2k_B T}{\pi K f_n} \frac{\left(\frac{\varphi(f)}{\Omega}\right)}{(1-\Omega^2)^2 + (\varphi(f))^2} \tag{5.6}$$

Assuming that the damping is constant over the range where the non-dimensional frequency ratio, $\Omega = (f/f_n)$, is $\Omega \approx 1$, then both forms of the PSD of the TMN reduce to simple Lorentzian functions and are given by

$$S_y(f) = \frac{k_B T}{\pi K} \frac{\left(\frac{f_n}{2Q}\right)}{\left(f - f_n^2\right)^2 + \left(\frac{f_n}{2Q}\right)^2} = \frac{k_B T}{\pi K} \frac{\left(\frac{f_n \varphi}{2}\right)}{\left(f - f_n^2\right)^2 + \left(\frac{f_n \varphi}{2}\right)^2} \tag{5.7}$$

To illustrate this, consider the effects of damping on TMN for a representative microcantilever with a stiffness of 10 N/m and natural frequency of 20 kHz (Figure 5.1). The damping was set as $Q = \varphi^{-1} = 3 \times 10^4$ in Equations 5.5 and 5.6 for viscous damping and the Kimball-Lovell solid; for the Zener solid, the values of Ξ and τ were chosen to obtain $\varphi^{-1} = 3 \times 10^4$ at 20 kHz. Far from resonance, $\Omega < 1$ (*pre-resonance*) and $\Omega > 1$ (*post-resonance*), and the frequency dependence of the various mechanisms is significantly different. In the vicinity of the

resonance peak ($\Omega \approx 1$), however, all three curves reduce to the simple Lorentzian given by Equation 5.7

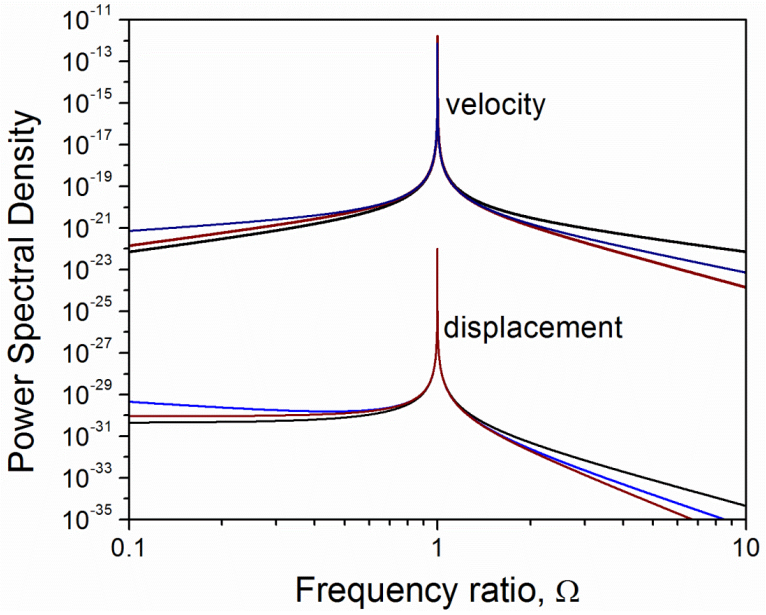

Figure 5.1: Graph of the power spectral density of displacement noise as a function of the normalized frequency for a representative structure with stiffness of 10 N/m and natural frequency of 20 kHz. The three curves represent viscous damping (black); Kimball-Lovell solid (blue); and Zener solid (red).

If the mechanism of damping is known, the appropriate form of the TMN PSD can be fit to the experimentally measured noise to extract the damping. The reverse is true as well; a broad-band observation of the TMN PSD can reveal the form of damping. In practice though, as will be shown, the amplitude of the TMN falls below the measureable threshold away from resonance. The strategies to apply the theoretical descriptions to the measured TMN for a set of single-crystal silicon microcantilever specimens are presented in the next sections.

5.2 Materials and microcantilever beam specimens

A set of six microcantilever beams were selected for the measurement and analysis of TMN. The specimens were manufactured by Das, who also obtained the raw free-decay data using the BES, and were featured in [97, 215]. This set of microcantilever specimens are manufactured according to the process described in Section 3.3.2 for the HFB microfabrication process. The dimensions, resonance frequency, and damping measured by the logarithmic

decrement for each specimen are listed in Table 5-1. The logarithmic decrement has been re-calculated using the improved analysis methods detailed in Chapter 3.

Specimen 1 is a bare silicon microcantilever, and all other devices feature aluminum nanowires. The nanowire array is patterned at the root of the microcantilever with the nanowires oriented along the axis of the silicon beam. The length of each nanowire is 20% that of the silicon beam. The thickness of the nanowires ranges from 50 to 100 nm, the width from 100 to 400 nm, and the center-to-center spacing between adjacent nanowires is 1 μm. The nanowires are constructed by first spray-coating the microcantilever with a 390 nm thick layer of a copolymer (MMA-MAA EL11 (Microchem, Inc.) that was diluted with methyl isobutyl ketone, and then baked at 150 ^{o}C for 90 seconds. Subsequently, the structures were spray coated with 200 nm of electron beam resist (PMMA A2, Microchem, Inc.) and baked at 180 ^{o}C for 90 seconds. The bilayer resist coated microcantilevers were patterned using electron beam lithography (Hitachi FEGSEM SU-70) operating at 30 kV with beam current of 357 pA and electron doses in the range of 6-8 nC/cm. After development, the lift-off process was implemented by depositing thin films of aluminum using electron-beam evaporation at a rate of 0.2 nm/s.

Table 5-1: Geometry, natural frequency, and damping of the microcantilever devices. Specimen 1 is a bare silicon microcantilever. Specimens 2 to 4 are composite structures consisting of an array of aluminum nanowires patterned at the root of silicon microcantilevers. The dimensions of the nanowires are not shown in the table and for more details see [147].

	Dimensions of microcantilevers			Natural frequency	Log decrement, δ ($\pm 7\%$)	$Q = \pi \delta^{-1}$ ($\pm 7\%$)
	Length	Width	Thickness			
Specimen 1	630 μm	300 μm	8.0 μm	26,749 Hz	1.63×10^{-5}	19.3×10^{4}
Specimen 2	750 μm	300 μm	8.5 μm	21,046 Hz	5.8×10^{-5}	5.40×10^{4}
Specimen 3	765 μm	300 μm	8.0 μm	19,160 Hz	2.7×10^{-5}	11.6×10^{4}
Specimen 4	750 μm	300 μm	7.5 μm	17,664 Hz	1.3×10^{-4}	2.40×10^{4}

5.3 Experimental methodology

The procedure to measure the damping from the TMN has two parts: (1) the measurement and (2) the analysis of the noise. The protocol is designed to reduce the impact of

random noise and remove any element of subjectivity that may be introduced in the analysis. Both parts of this process are discussed in turn.

5.3.1 Measuring the noise

Essentially, the experimental procedures used to measure the noise follow the established protocols used to measure the free-decay. The clamp that is used to hold the microcantilever specimens is the same clamp that is used with the BES but now it is removed from the piezoelectric shaker and is placed on a large stainless steel block in the vacuum chamber. The vacuum chamber is bolted to an optical table with pneumatic suspension to isolate the system from ground vibrations. However, the vacuum pumping elements remain on the floor and act as a conduit for building vibrations to reach the specimen. To reduce the impact of environmental noises, all experiments are conducted during building quiet hours from the late evening to early morning hours.

The noise measurement is made using the OFV-5000 LDV and VD09 velocity decoder and a 100 Hz high pass analog filter is applied. The laser spot is aimed onto the approximate end of the microcantilever beam and the ambient vibration is recorded at a sampling rate of 100 kHz. The sampling rate is chosen so that the Nyquist frequency is sufficiently greater than the first mode resonance frequency and the frequency spectrum is de-cluttered of spurious noises.

The recording time is determined based on the following trade-off. The recording time is directly proportional to the frequency resolution of the computed PSD. Hence, the longer the recording time, the larger the number of data points that are available for fitting the resonance peak. However, as the recording time increases, the measurement becomes more susceptible to sporadic extrinsic noise and temperature fluctuations and the data set becomes computationally unwieldy. By conducting several full cycles of measurement and analysis, a recording time of 90 seconds was determined to be optimal. Five measurements of the noise are performed on each specimen. In addition, for one device (Specimen 5), noise was acquired for 100, 110, 120 and 130 seconds to study the effects of recording time on the estimate of damping.

5.3.2 Analysis of the noise spectrum

The velocity time series data is imported into MATLAB and is conditioned to remove any offset and drift and scaled to units of velocity using the decoder sensitivity. The data is also numerically integrated using MATLAB to obtain the displacement time series. The next step is to obtain the PSD of the displacement time series.

Two popular methods for the computation of the PSD are Bartlett's method [216] and Welch's method [217]. Both methods segment the time series, compute the Fourier transform of each segment, and then appropriately reassembling the transforms, but Welch's method applies a windowing function to each segment. The window function serves to reduce, but not eliminate, the time-segment edge discontinuities [148]. These approaches are computationally efficient but suffer from spectral leakage due to the segmentation, biasing the estimation of the quality factor [218, 219]. The latter effect, in particular, is a major concern because the bias increases as damping decreases. Therefore, the PSD is calculated by a direct method (also called the Daniell method) that eliminates spectral leakage by avoiding segmenting the time series and re-assembling in the frequency domain. The underlying statistical concepts and numerical implementation of the Daniell method are discussed in detail in [218]. Briefly, a single Fourier transform of the entire time series is performed using a Hanning windowing function; then, the squared magnitude is computed and, to reduce variance, the PSD is averaged by grouping adjacent frequency bins [220]. The number of adjacent frequency bins that are averaged together is henceforth referred to as the *averaging factor* (Λ).

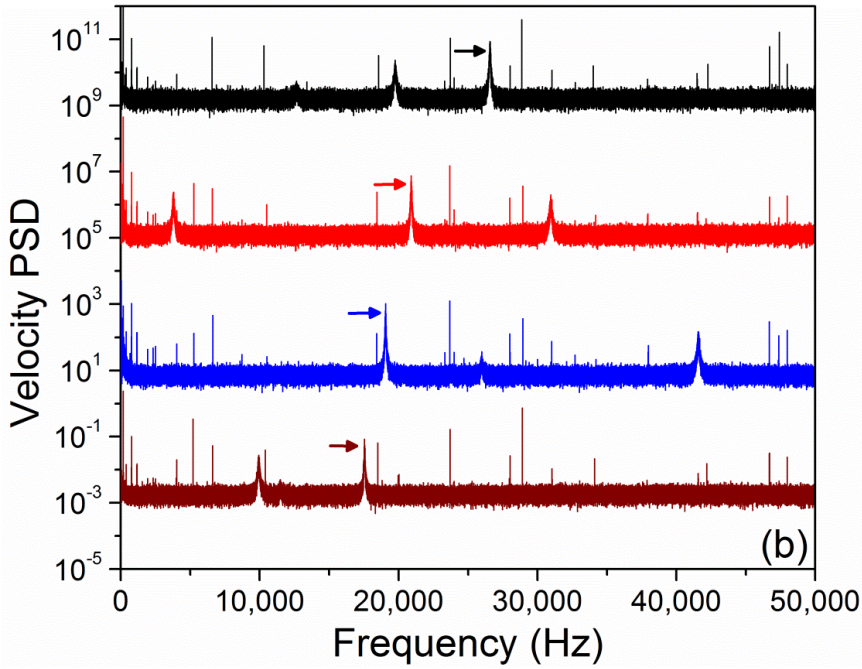

Figure 5.2: The PSD of the noise measured at atmospheric pressure is shown for each specimen. An offset has been applied to improve the clarity of the information. The first mode resonance frequencies are noted by the arrows for Specimen 1 (black), Specimen 2 (red), Specimens 3 (blue), Specimen 4 (brown).

A representative example of the power spectrum of the displacement noise is shown in Figure 5.2. The graph exhibits sharp peaks that are associated with very high Q electrical noises and broad peaks associated with a damped mechanical vibration. Thus, a measurement of the noise when the system is at atmospheric pressure is instrumental to differentiate the thermomechanical noise from spurious system noises. However, more than one thermomechanical noise peak is identified. The question, then, is: which peak is the first mode?

The first mode resonance may be found with respect to an estimation using standard Euler-Bernoulli beam theory and the measured beam dimensions. Supposing that the dimensions are unknown, the modes may be distinguished by their respective amplitude. For a simply supported beam undergoing flexural vibrations, the damping increases with increasing mode number, so it follows, then, that the first mode thermomechanical noise response has the highest amplitude.

Another method to distinguish the modes is to use the aliasing effect. A frequency source above the Nyquist frequency is folded over to a lower frequency according to the relation

$$f_{alias}(N) = |f - Nf_s|, \tag{5.8}$$

where f_s is the sampling frequency and N is an integer. Due to the nature of the aliasing effect, there are in fact an infinite number of frequencies above the Nyquist frequency that can be folded down. The sampling frequency may be continually reduced until all but one of the observed TMN peaks moves. By comparing the location of the translated peaks, the frequency of origin can be backtracked using Equation 5.8 assuming N = 1. The movement of the second and third mode TMN peaks according to the sampling frequency is demonstrated in Figure 5.3.

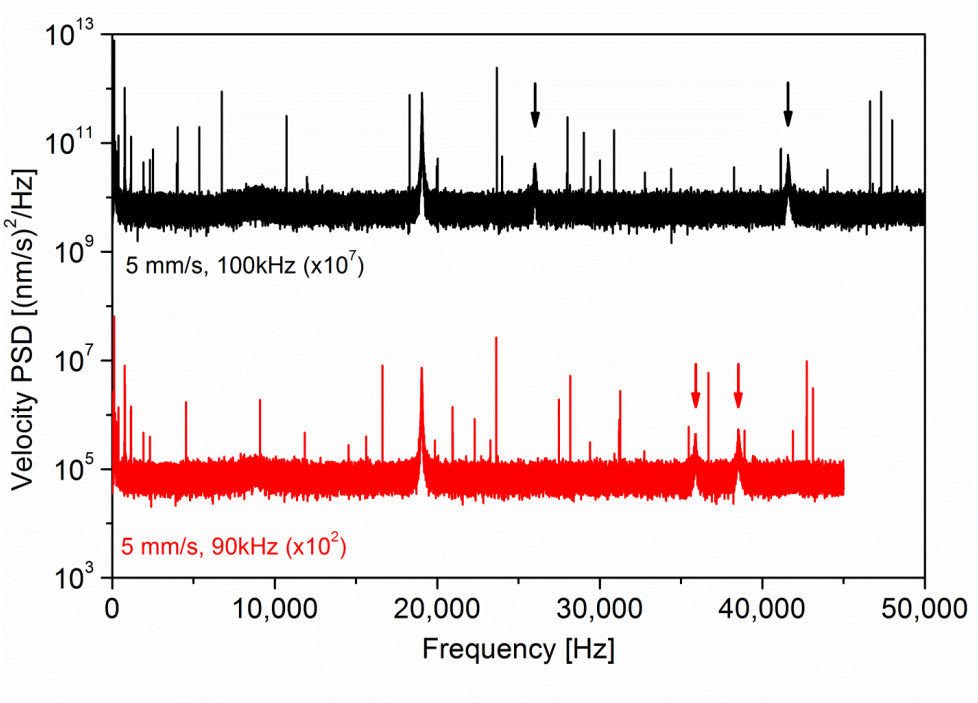

Figure 5.3: The power spectral density of the thermomechanical noise of Specimen 3 measured at two different sampling frequencies that have been plotted with the indicated offset. The upper plot shows the noise measured at a sampling rate of 100 kHz and the lower plot was measured at 90 kHz. The location of the second and third mode resonance frequencies are noted with arrows. The actual frequencies for the second and third mode occur at 118 kHz and 332 kHz, respectively. Note that some of the very sharp peaks associated with electronic noises have also moved due to the aliasing effect.

After applying this strategy to all of the microcantilever beam specimens, aliased peaks are found at the following frequencies in Figure 5.2: 12.8 kHz and 19.8 kHz for Specimen 1; 3.7 kHz and 30.9 kHz for Specimen 2; 25.9 kHz and 41.6 kHz for Specimen 3; 9.9 kHz and 11.5 kHz for Specimen 4. The instrument noise peaks are also observed to translate, which demonstrates that the aliasing effect can be utilized to remove extrinsic noises should they interfere with the on-resonance response of the TMN. However, for a low damped resonator operating in a vacuum condition, the PSD of the TMN response features a very sharp peak and it is unlikely that other noises overlap. The PSD of the measured noise in vacuum for all the specimens is plotted in Figure 5.4.

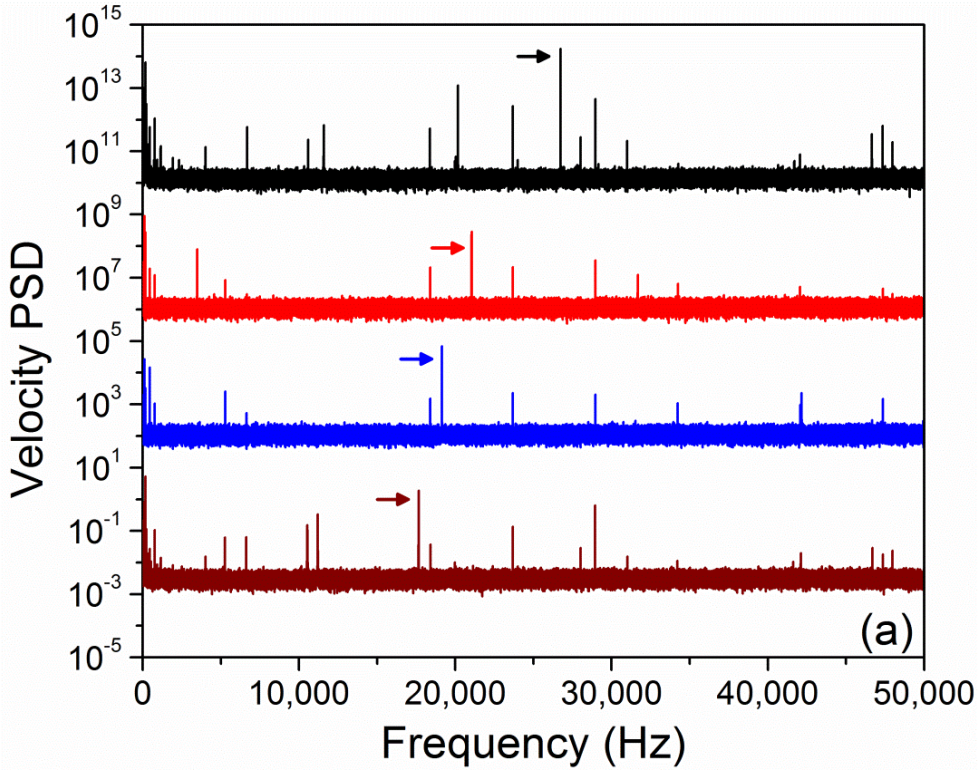

Figure 5.4: The velocity PSD of the measured noise for each specimen is plotted with an offset for clarity. The first mode resonance frequencies are noted by the arrows for Specimen 1 (black), Specimen 2 (red), Specimens 3 (blue), Specimen 4 (brown).

For the low damped resonators, the resonance peaks are narrow (full width at half maximum ~ 3 Hz) and separated by more than 750 Hz from any other noise peak. If the dominant mechanism of dissipation is known, then damping can be estimated by fitting the appropriate form of Equation 5.5 or 5.6 to the first mode resonance peak. In most cases, though,

damping is a sum of several mechanisms. Furthermore, other sources of noise may be present in the measurement and obscure the features of the TMN away from resonance. Away from resonance, the amplitude of the TMN is lower than the measurement resolution of the LDV. Some have proposed that the background noise that is due to the instrumentation can be subtracted to reveal the broad spectrum characteristics of the mechanical noise [103]. This strategy is not implemented here because it depends on the assumption that the background noise is constant, which is not the case due to the unique reflectivity of each specimen. All of these problems are circumvented by only analyzing the TMN response on resonance with a model that is not necessarily damping specific. For the displacement PSD or the velocity PSD of the noise, the resonance peak is fit with a Lorentzian curve, respectively,

$$S_y(f) = A_1 + A_2 \frac{\left(\frac{f_n}{\mathrm{Q}}\right)}{\left({f_n}^2 - f^2\right)^2 + \left(\frac{f^2 f_n^2}{\mathrm{Q}^2}\right)}; S_v(f) = B_1 + B_2 \frac{\left(\frac{f_n}{\mathrm{Q}}\right) f^2}{\left({f_n}^2 - f^2\right)^2 + \left(\frac{f^2 f_n^2}{\mathrm{Q}^2}\right)} \tag{5.9}$$

where the parameters capture the white-noise baseline (A_1, B_1) and peak amplitude (A_2, B_2).

At this point, the two key decisions that must be made are the selection and treatment of the data. Choosing the averaging factor that is used to condition the PSD data introduces an element of subjectivity that may affect the measurement. The application of an averaging factor inherently influences the measured Q and resonance frequency because it alters the amplitude and the frequency resolution of the data [218]. Thus, a systematic protocol is introduced to reduce the influence of human subjectivity on the analysis.

Unless there is interfering signals, the noise PSD data that comprises the resonance peak is manually selected at the shoulders, where the Lorentzian curve meets the baseline. Then the PSD is re-calculated for this selected data using a series of averaging factors (Λ = 5:31). Notably, there is no systematic bias in the estimate of the Q over this range, which is the primary motivation for using the Daniell method to estimate the PSD of the noise. For each Λ, Equation 5.9 is fit using the Levenberg-Marquardt weighted least-squares method [221]. The fitted curve is plotted over the data to visually check that the fit captures the baseline, the peak shape, the peak height, and that the residuals are uncorrelated [219, 222, 223]. Figure 5.5 shows the

resonance peak and fitted Lorentzian curves for one representative measurement of the noise of Specimen 4.

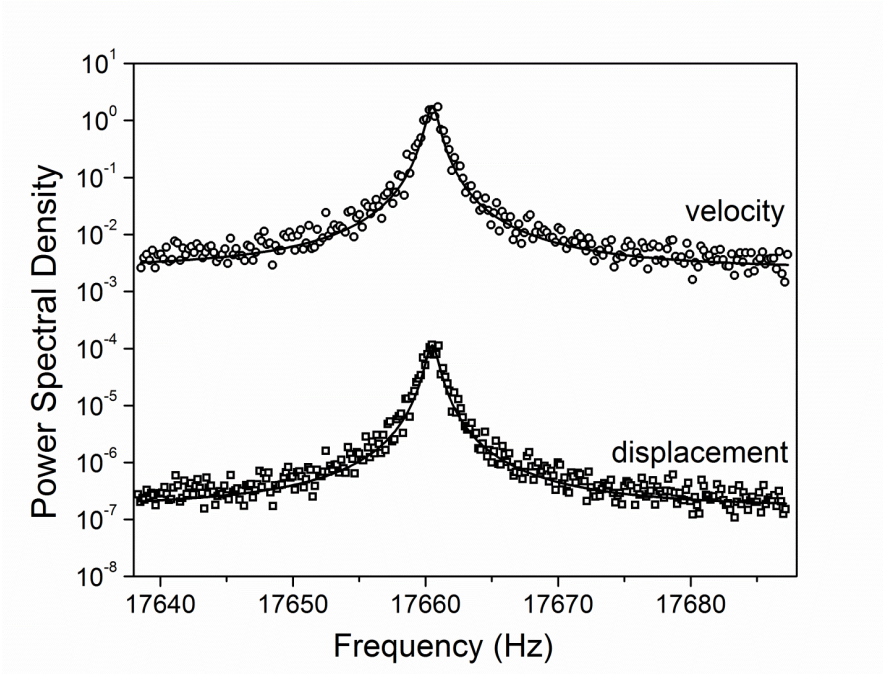

Figure 5.5: The velocity PSD (in units of $(\mu m/s)^2/Hz$) and the displacement PSD (in units of nm^2/Hz) of the resonance peak of Specimen 4 is fit with a Lorentzian function (solid line).

The fitting results for each Λ are examined and the extracted properties are binned if the fitting conditions are met. Thus, for a single-shot measurement of the noise, there may be a range of Q values extracted. Ultimately just one of the binned measurements of the *Q* is selected according to an objective metric: the *Q* that falls within one standard deviation of the mean with the lowest Λ is selected as the final value.

5.4 Results

The fitting routine is repeated for five independent measurements of the noise each of 90 seconds in duration, measured in vacuum for each specimen and the average is taken to be the final value of the damping. The number of measurements of the noise is chosen for consistency with respect to the measurement of the logarithmic decrement of decay. Table 5-2 presents the main results of the study. The relative uncertainty of the mean *Q* is the standard deviation taken

as a percentage of the mean. The relative error of the natural frequency is less than 1 Hz (one part in 10^5).

Table 5-2: Estimates for natural frequency and quality factor obtained by analyzing the velocity PSD, $S_v(f)$, and displacement PSD, $S_y(f)$.

	Velocity PSD		Displacement PSD	
	f_1 [Hz]	Q	f_1 [Hz]	Q
Specimen 1	26,743	20.3×10^4 (±6%)	26,743	24.5×10^4 (±18%)
Specimen 2	21,045	6.0×10^4 (±18%)	21,045	5.8×10^4 (±19%)
Specimen 3	19,150	10.9×10^4 (±26%)	19,150	9.5×10^4 (±15%)
Specimen 4	17,660	1.8×10^4 (±6%)	17,660	1.8×10^4 (±8%)

The values in Table 5-2 can be compared with those from the method of free decay in Table 5-1 because the same specimens and experimental infrastructure were used for both sets of measurements. The noise-based measurements are as accurate, but less precise, than the logarithmic decrement of the free decay for these high-Q microcantilever beam resonators.

5.5 Analysis of limitations

The precision of the measurements of damping extracted from the TMN is influenced by errors inherent in the estimation of the PSD of a finite length time-series measurement of stochastic fluctuations and their effects on uncertainties associated with fit parameters obtained using a least-squares analysis [148, 219, 221, 224]. Indeed, it has been noted that the goodness-of-fit of a single measurement may not provide an estimate of the uncertainty of the extracted parameters even when the analysis results in an excellent fit, so multiple independent measurements are required [219]. Accordingly, the precision of the measurements presented in Table 5-2 is defined by the estimate of the relative uncertainty, which ranges from 6% to 26 % for five measurements of the TMN.

Errors for noise-based estimates of damping arise from five factors of measurement and analysis:

(1) The finite recording time.
(2) The estimation of the PSD.
(3) The treatment of the PSD by averaging.
(4) The sharpness of the resonance peak for high-Q resonators.
(5) The random noise.

Each of these factors will be discussed in turn.

5.5.1 Effects of the recording time

The first source of error, the finite recording time is unavoidable. As noted earlier, the recording time of 90 seconds is chosen so that a sufficient number (100 to 200) of data points could be collected for fitting the resonance peak while avoiding errors due to random excitations and thermal drift. To check the effect of the recording time, the noise of Specimen 3 was measured at recording times of 90 seconds up to 130 seconds. Table 5-3 shows the effect of the recording time, where each measurement is the average of five noise measurements. Over this range of recording times, the mean value of Q varied by about 4% and the measured frequency varied by less than one percent. The standard error of the measured Q does not show any dependence on the recording time.

Table 5-3: The effect of the recording time on the measured resonance frequency and quality factor of Specimen 3. Five measurements of the noise are made for each recording length, and then the parameters are extracted and averaged.

Recording time [s]	f_1 [Hz]	Quality factor	
		Mean	Error
90	19150	10.8×10^4	28 %
100	19150	10.3×10^4	24 %
110	19150	11.0×10^4	26 %
120	19150	10.3×10^4	14 %
130	19150	11.1×10^4	25 %

5.5.2 Effect of the PSD estimation

The estimation of the PSD inherently affects measurement of the quality factor and the Daniell method was chosen to reduce the effects of spectral leakage that may occur for other PSD calculations such as Bartlett's or Welch's method. The Daniell method is now evaluated in comparison to Welch's method in Table 5-4. Welch's method is calculated using a Hanning window and the appropriate segment re-combination to achieve the same averaging and number of points in the resonance peak as the PSD calculated using the Daniell method.

The comparative analysis was performed on five measurements of the noise, using Specimens 1 and 4, with the same fitting bounds of the TMN peak. The measured Q and f_1 using Welch's method are given in Table 5-4. The resonance frequency measured from the Welch's PSD agrees with the results in Table 5-2. The measured *Q* from Welch's PSD of the TMN has a precision that is comparable to the range of precisions for the damping measured from the PSD estimated using Daniell's method. This analysis demonstrates that the method of PSD estimation does not affect the precision or accuracy, at least for these specimens.

Table 5-4: Measurements of the frequency and quality factor obtained by analyzing the displacement PSD, $S_y(f)$, estimated using Welch's method. The reported value is the average of five measurements of the TMN.

	Displacement PSD	
	f_1 [Hz]	Q
Specimen 1	26743	20.3×10^4 ($\pm$ 25%)
Specimen 4	17660	19.4×10^4 ($\pm$ 7%)

Another factor that influences the data is the inherent noise that is introduced by the PSD of a finite time series. The noise has been demonstrated by Sader *et. al*. to affect the fitting parameters of a least-squares analysis [219]. Their analysis of the uncertainty resulted in a close-form expression for the standard deviation of the *Q*,

$$SD(Q) = \frac{f_T}{Q_T}\sqrt{\frac{6Q_T}{\pi f_T \mathcal{T}}} \tag{5.10}$$

and resonance frequency,

$$SD(f) = \frac{f_T}{Q_T}\sqrt{\frac{7Q_T}{8\pi f_T \mathcal{T}}} \tag{5.11}$$

where f_T and Q_T are the "true" values and $\mathcal{T}$ is the duration of the measurement of the noise. To use these equations, the true values are taken to be the parameters measured from the logarithmic decrement of free decay. The theoretical standard deviation of the measurements from the TMN is listed in Table 5-5, reported as the standard error.

Table 5-5: The theoretical estimate of the standard error for the resonance frequency and damping measured from the TMN.

	f_1 error	Q error
Specimen 1	3×10^{-5} %	17 %
Specimen 2	7×10^{-5} %	10 %
Specimen 3	5×10^{-5} %	16 %
Specimen 4	12×10^{-5} %	8 %

This analysis demonstrates that the inherent variance of the PSD causes a large error for the measured Q for these specimens. The values listed in Table 5-5 are comparable to the errors reported in Table 5-2. However, in some instances, such as those reported in Table 5-3, the measured Q has a greater error. This indicates that it is not simply the calculation of the PSD that is the cause of the poor precision.

5.5.3 Effects of the PSD averaging

The third factor that affects the measured resonance frequency and quality factor is the averaging factor. While the PSD contains more than 10^6 data points, between 100 and 300 points comprise the resonance peak. When fitting Equation 5.9, the estimate of Q is most influenced by ~10 points that lie between the half-power points and the peak. The treatment of the PSD with the averaging factor reduces the number of data points by more than half and also skews the amplitude of the peak data points.

Table 5-6 shows the effect of Λ for one measurement performed on Specimen 5. For $\Lambda < 9$, the peak is not sufficiently smooth to achieve a good fit of Equation 5.9 using the weighted least-squares method. As Λ increases from 9 to 17, the number of fit points and frequency resolution reduce in proportion and the quality factor varies by ~7%.

Table 5-6: Effects of the averaging factor (Λ) on fitting and estimation of the quality factor for Specimen 5.

Λ	# of fit points	Frequency resolution	Q
9	234	0.10 Hz	9.50×10^4
11	191	0.12 Hz	8.87×10^4
13	163	0.14 Hz	9.43×10^4
15	141	0.17 Hz	8.95×10^4
17	124	0.19 Hz	9.07×10^4

5.5.4 Effect of the sharpness of the resonance peak

The third factor that influences the measurements is the sharpness of the TMN resonance peak. For a low-loss device with $Q > 10^5$, the sharpness and magnitude of the peak above the noise floor makes the fitting dependent on only a small fraction of the points; the higher the Q, the sharper the resonance peak and the fewer the number of data points that influence the fit parameters. The finite frequency resolution of the PSD also distorts the shape of the resonance peak [224].

To quantify these effects, then, the results obtained by fitting the displacement PSD and the velocity PSD are compared in Table 5-2. Since the displacement data is derived from the velocity data, both time series have the same contribution from extrinsic noise and the overall impact of the sharpness of the peak can be judged independently. For Specimens 2 to 4, the estimate of the Q is in good agreement, suggesting that it is sufficient to fit either the velocity PSD or the displacement PSD for resonators with $Q < 10^5$. However, for Specimen 1, the fitting to the velocity PSD required higher averaging factors than the displacement PSD, resulting in a degraded frequency resolution and different fit parameters. Thus, when reporting a definitive

quality factor, the estimate obtained from the velocity PSD and displacement PSD should be averaged.

5.5.5 Effect of random noise on the fitting

A high Q resonator is sensitive to disturbances in the environment. Excitation by extrinsic noise elevates the magnitude of the resonance peak, an event that, when subtle, is difficult to distinguish or separate from the TMN. The increase in amplitude and sharpness of the resonance peak translates to the measurement of higher Q. The tendency to measure quality factors that are greater than the "true" value of the damping measured by the logarithmic decrement, Q_δ, of the free-decay is demonstrated in Figure 5.6.

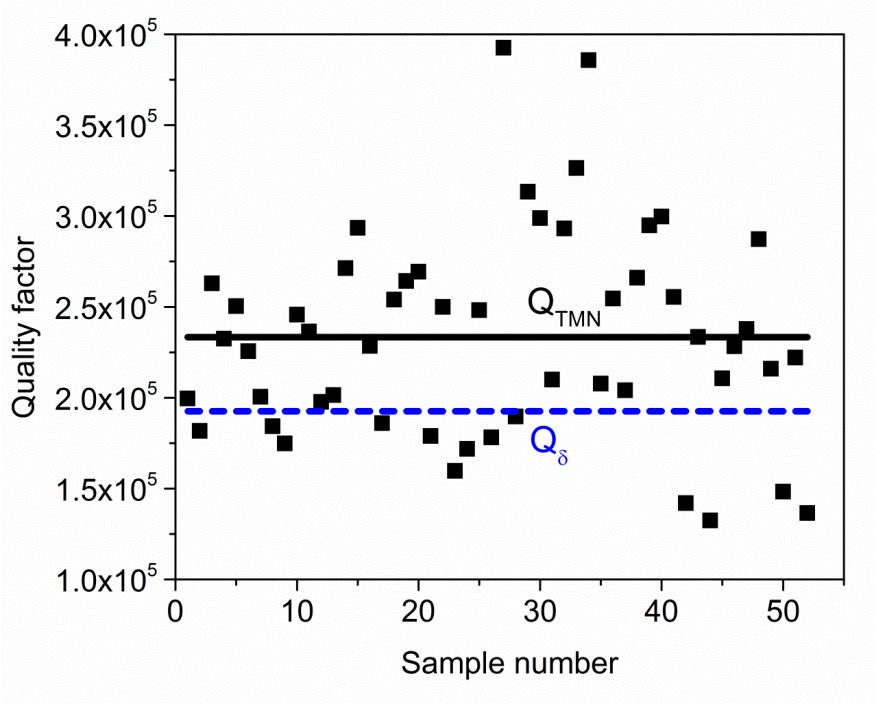

Figure 5.6: Fifty-two measurements of the Q from independent measurements of the TMN for Specimen 1 with an average value of 23.3×10^4 (±24%). The dashed line is the damping measured by the logarithmic decrement of free-decay.

5.6 Summary

This chapter qualitatively asses the damping of silicon based microcantilever beam resonators measured from the TMN. This represents one of the first detailed comparisons of

damping in well-characterized resonators using two different measurement techniques. The comparison is possible because the two sets of measurements use the same specimens, experimental environment, instrumentation, and the measurement with the same LDV.

A systematic methodology for measuring and analyzing the TMN has been presented and implemented for a set of four single-crystal silicon based microcantilever beam resonators. The specimens have resonance frequencies ranging from 17.6 kHz to 26.7 kHz and quality factors ranging from 2×10^4 to 2×10^5. The accuracy of the values of the quality factor measured from the TMN is evaluated relative to the well-established logarithmic decrement of the free-decay. The damping extracted from the TMN overestimates the logarithmic decrement by 16% for Specimen 1 and 7% for Specimen 2, and underestimates by 18% for Specimens 3 and 25% for Specimen 4. With respect to the logarithmic decrement, the noise-based measurements of the damping suffer a greater systematic error and relative error.

The uncertainties are primarily due to (1) the estimation of the power spectral density of the TMN from a finite time series of stochastic fluctuations and (2) the fitting of a resonance peak. For $Q > 10^5$, the fit is sensitive to the number and distribution of data points in the vicinity of the peak, which is defined by the recording time, averaging, and the estimation of the PSD. Variations in experimental conditions, such as the clamping and influence of mechanical noise, can also account for the discrepancy, but measurements over a larger set of materials, structures, frequencies, and quality factors are required to establish whether there are fundamental limits to the accuracy of noise-based estimates of the damping. Regardless, approaches for quantifying the absolute accuracy of the damping of high-Q microresonators is not yet available [187].

Using the TMN, however, has certain advantages over the measurement of the logarithmic decrement. TMN is ubiquitous in resonators and can be measured with a commercially available LDV and analyzed with a computer and does not require the precision actuators and controllers for measuring the free-decay or other force-excitation methods. Measuring the damping from the TMN is especially ideal for fragile or geometrically intricate resonators.

CHAPTER 6

Measuring the damping of a thin film membrane resonator using thermomechanical noise

Thin film membrane resonators are receiving attention due to their commercial availability, ease of manufacture, high quality factors, ultra-high frequency range, and interesting properties [139, 225]. Such devices have measured damping with quality factors approaching 10^7, however, the damping has been demonstrated to be sensitive to boundary conditions, mode number, material properties, stress state, and interaction with the environment [226, 227]. Consequentially, there is a growing body of literature dedicated to investigating the dependence of damping on these variables. To date, the experimental methods used to study the damping of thin film membrane resonators include harmonic forced-excitation [100, 138, 139, 227-234] and free-decay techniques [139, 230].

There are several factors that make the study of damping difficult: membrane resonators typically have resonance frequencies in the hundreds of kHz to MHz range; the vibration modes are closely spaced; the frequency is sensitive to the stress state and thermal effects; the damping is sensitive to the boundary conditions [139, 225, 235]. Therefore, the experimental methods require actuators and detectors that are linear and accurate over MHz bandwidths with fine frequency resolution. Further complicating experiments, the vibration of the membrane can be measured in the frame and vice-versa [138, 139, 233]. The use of TMN noise to measure the damping has the potential to reduce complications of the mechanical spectroscopy of damping in nanomembrane resonators. Specifically, the ability to measure all of the vibration modes in a one shot measurement simplifies the process and initial knowledge of the stress state to estimate the resonance frequency is not required.

Chakram *et. al.* used the TMN to measure the damping of a membrane resonator and reported good agreement with the free-decay approach [227]. However, the details published on their methods and results are minimal. Therefore, the aim of this chapter is to initiate an evaluation of the applicability of the TMN for measuring the damping of membrane resonators.

This work uses the TMN to measure the damping at room temperature and atmospheric pressure of a bi-layer thin film membrane resonator using the UHF-120 LDV.

6.1 Introduction to membrane resonators

Thin film membrane resonators are typically commercially sourced and are used as-is or modified. These batch fabricated structures are referred to as TEM "windows" and are constructed to form a thin SiN film membrane (50nm < h < 200 nm) on a single-crystal silicon substrate. The membrane is made by depositing a SiN film on one side of a single-crystal silicon substrate [236]. Then the other side of the substrate is selectively and anisotropically etched to form a depression that reaches the SiN layer on the reverse surface. Thus the SiN film is suspended over a hole. For future clarification, the patterned side of the single-crystal silicon substrate will be referred to as the B-side. The A-side is planar and materially homogonous. In Figure 6.1, the membrane can be seen as a dark square in the middle of the frame on the A-side. The coloration is an artifact of the SEM imaging; a pure SiN window is semi-transparent to light in the visible spectrum [230]. This effect can be used to locate the membrane on the A-side. Though when metalized, the surface becomes more uniformly reflective which makes it difficult to optically differentiate the membrane from the frame.

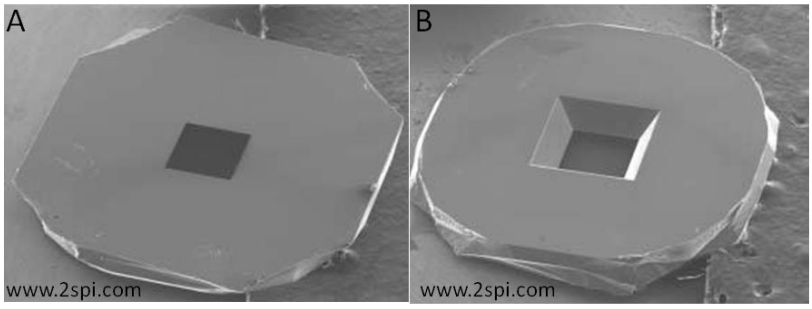

Figure 6.1: A scanning electron microscope image of a commercially produced silicon nitride nanomembrane on a single-crystal silicon frame [236].

For a simply supported thin film, the dynamics may be plate-like or membrane-like. The behavior of the former is a function of the stiffness and the latter is a function of the stress [237]. The threshold for the stress-governed regime is determined when the flexural rigidity satisfies the relation [138, 237]

$$\frac{Eh^2}{12(1-\nu^2)} \ll \frac{\sigma L^2}{\pi^2}, \tag{6.1}$$

where ν is the Poisson ratio. Most commercially available thin film membranes have a stress that is greater than 250 MPa and dimensions which satisfy the condition for membrane-like behavior [236]. The resonance frequency of a stress-governed square membrane may be predicted by [227]

$$f_{m,n} = \frac{1}{2L}\sqrt{\frac{\sigma}{\rho}(m^2+n^2)}, \tag{6.2}$$

where the mode shape indices, m and n, are positive integers. The membrane has symmetric ($m \sim n$) and asymmetric modes and some mode shapes are demonstrated in Figure 6.2 [138].

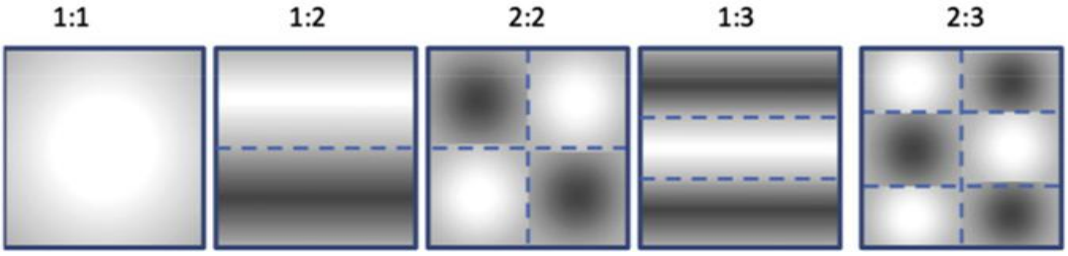

Figure 6.2: Predicted mode shapes of a square membrane resonator. The shading indicates positive and negative displacement [138].

6.2 Materials and experimental methodology

The particular membrane resonator used in this study is commercially sourced from 2SPI and then modified with an additional aluminum layer deposited on the A-side. It is a composite structure with a 100 nm aluminum layer e-beam evaporation deposited onto a 100 nm thick SiN film. The silicon nitride film was grown by CVD at 700 ˚C resulting in a low-stress ($\sigma \sim 250$ MPa) SiN film [227, 236, 238]. The stress of the Al film is unknown, but is assumed to be low. The material properties of the SiN and Al are listed in Table 1. The frame is 200 µm thick and 2.5 mm square, with a side length, L, of 500 µm.

Table 6-1: The material properties of SiN and Al at room temperature [100, 239].

Material Properties	SiN	Al
Density, ρ	2700 kg/m^3	3000 kg/m^3
Poisson ratio, v	0.25	0.33
Young's Modulus, E	126 GPa	75 GPa

According to Equation 6.1, based on the dimensions and material properties, the dynamics of the membrane will be governed by the stress. Interchanging the properties of Al and SiN in Equation 6.2 gives a possible first mode frequency range of 408 kHz to 433 kHz. If we consider that a stoichiometric Si_3N_4 represents the highest stressed commercially available membrane ($\sigma \sim 900$ MPa), the maximum possible (1, 1) frequency for the membrane is 822.15 kHz. This estimation of the resonance frequency provides a range to experimentally study in detail.

The process to find the resonance frequencies and measure the damping in the thin film membrane resonator has two parts: first the membrane is located on the A-side surface and then a set of locations are interrogated via a series of single point time-series measurements. The location of the membrane can be found because the response to actuation is greater in the compliant membrane than in the rigid frame [138]. The first step of this process is to mount the resonator on a large stainless steel block with double sided tape (3M), as shown in Figure 6.3. The block has been precision machined for flatness and the mass of the block (~500g) ensures that the membrane does not move when the nano-positioning stage translates. A piezoelectric bending actuator is placed into contact with the block. It is used to locate the edges of the membrane and is removed for subsequent measurements of the noise.

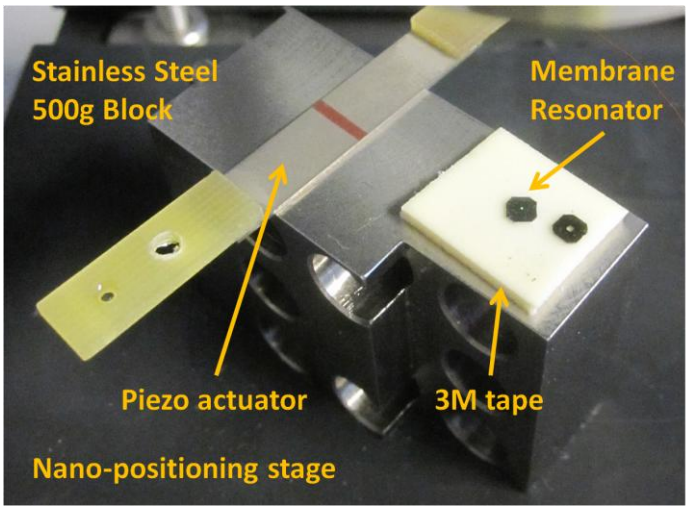

Figure 6.3: The TEM window is mounted on a stainless steel block with double sided tape adhesive. The green dot of the LDV beam is barely visible in the center of the frame where the membrane is located. A second, broken resonator is shown as a reference for the approximate location of the window in the frame. The mounting block is significantly massive compared to the resonator and ensures that the position does not change when the piezo is actuated or the nano-positioning stage is translated.

The piezoelectric actuator is driven at a constant frequency of 100 kHz and the A-side surface is scanned over an area much larger than the membrane dimensions with a scanning grid density of 50 µm. The scanning measurement is made using a 1 MHz bandwidth, with a 6.4 ms sampling time, for a frequency resolution of 156 Hz. The measured amplitudes in the membrane relative to the frame reveal the location of the membrane, as shown in Figure 6.4. This procedure is repeated with a smaller but denser (15 µm) grid at the corners of the membrane.

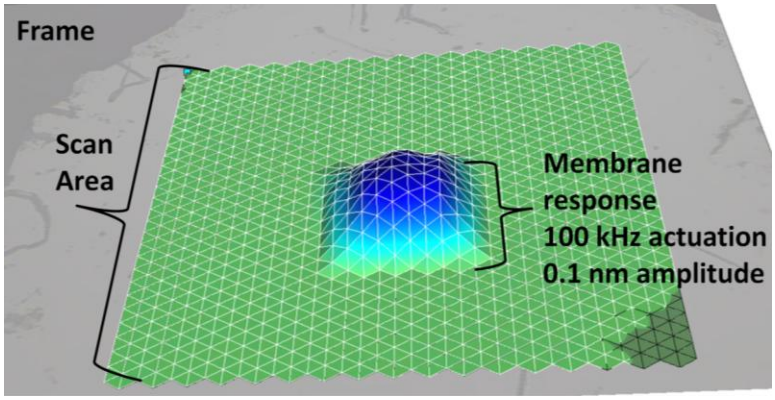

Figure 6.4: The amplitude of the scanned area of the membrane resonator is highlighted relative to the camera image of the resonator frame. The membrane has a higher displacement response than the frame at the 100 kHz actuation frequency.

Having found the approximate location of the membrane, the UH-120 LDV is used to interrogate nine locations on the membrane. Figure 6.5 shows these locations relative to the approximate edges of the membrane. Two points on the frame, away from the membrane, are also interrogated. Measuring the ambient noise on the frame provides a PSD spectrum to cross reference with and find extrinsic and electronic sources of noise in the system.

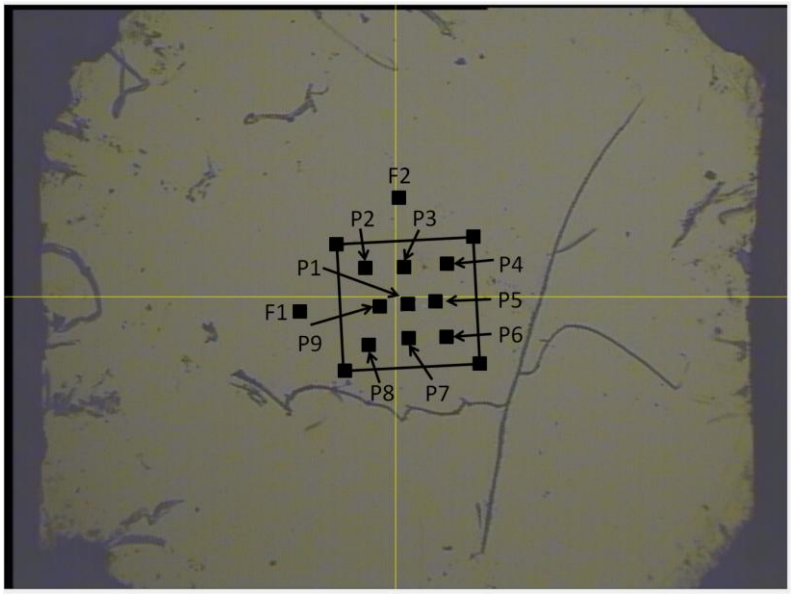

Figure 6.5: The surface of the membrane resonator is interrogated by laser Doppler vibrometry in a number of locations, P1 - P9. The black line represents the approximate edge of the membrane where it meets the frame. The points F1 and F2 are measurement locations on the frame, about 100 μm from the edge of the membrane.

Each point is measured 91 consecutive times at a sampling rate of 5 MHz and a recording time of 6.4 ms. The PSD of each time series is computed in the Polytec data acquisition software and the magnitudes are averaged at each frequency line, in a technique known as 'magnitude averaging,' to reduce the variance without reducing the frequency resolution [168]. An aliasing check is also performed on P1 and P6 by measuring at a 10 MHz sampling rate and a recording time of 5 ms. Finally, the PSD of the noise is computed using the Polytec analysis software. The resonances are identified by comparing the noise measured on the membrane surface to noise measured on the frame. Then the resonance peaks are fit with a generic Lorentzian function using a weighted least-squares Levenberg-Marquardt algorithm.

6.3 Results

Figure 6.6 shows the PSD of the TMN measured at the two locations on the frame. Figure 6.7 and Figure 6.8 are the PSD of the TMN measured at the points P1 and P6 on the membrane. Finally, Figure 6.9 and Figure 6.10 are the aliasing checks for P1 and P6, respectively.

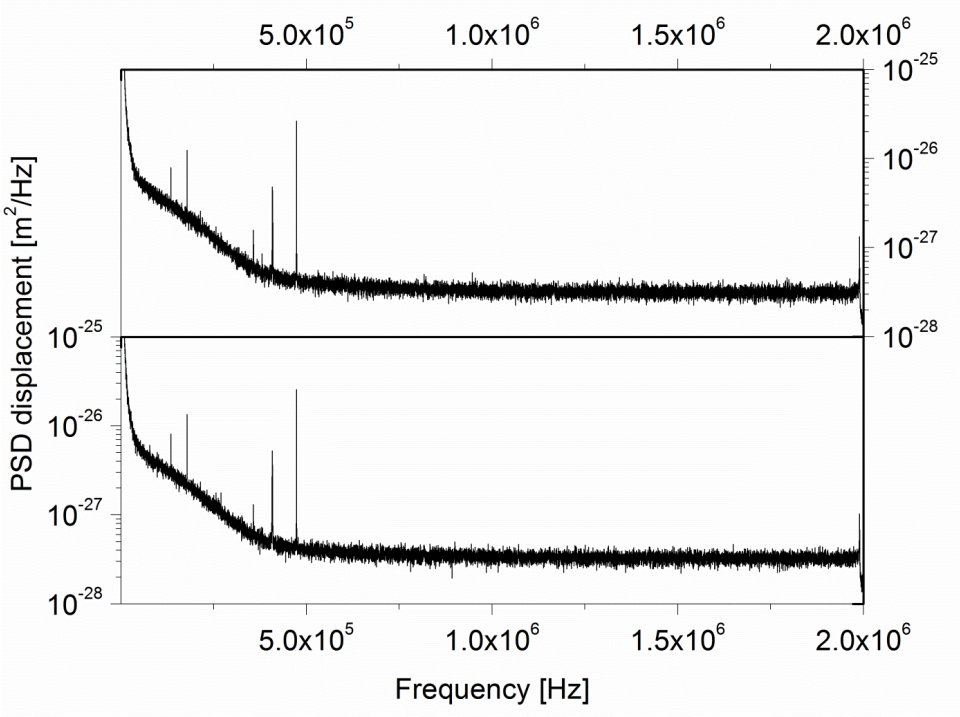

Figure 6.6: The PSD of the displacement noise measured in the frame. The lower and upper plots are the measurements at F1 and F2, respectively.

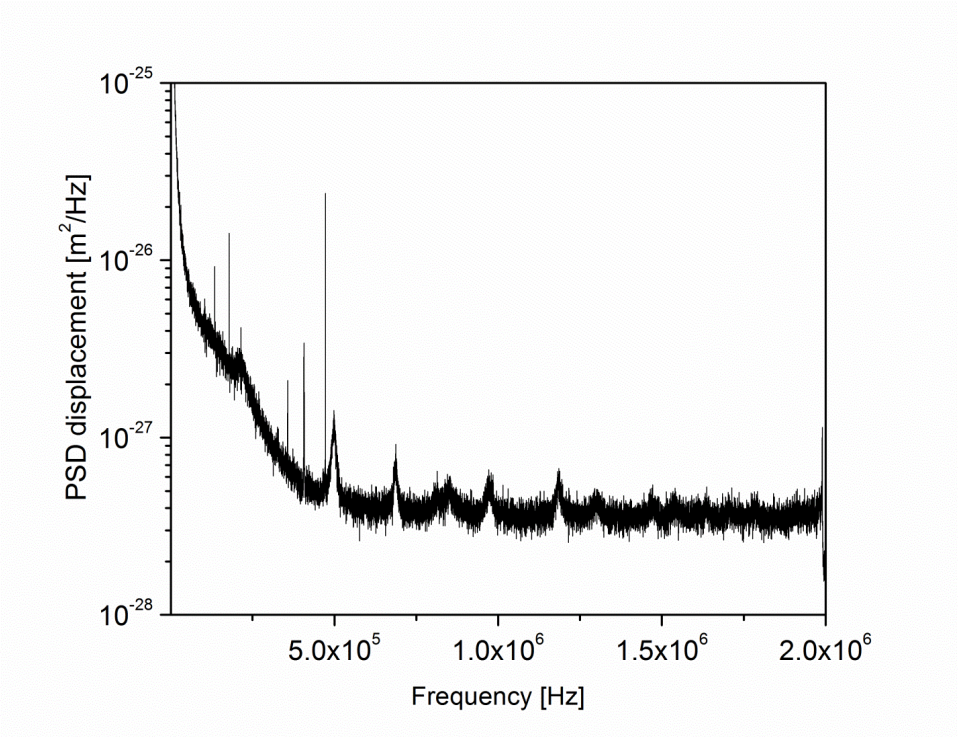

Figure 6.7: The PSD of the displacement noise measured at location P1 on the membrane.

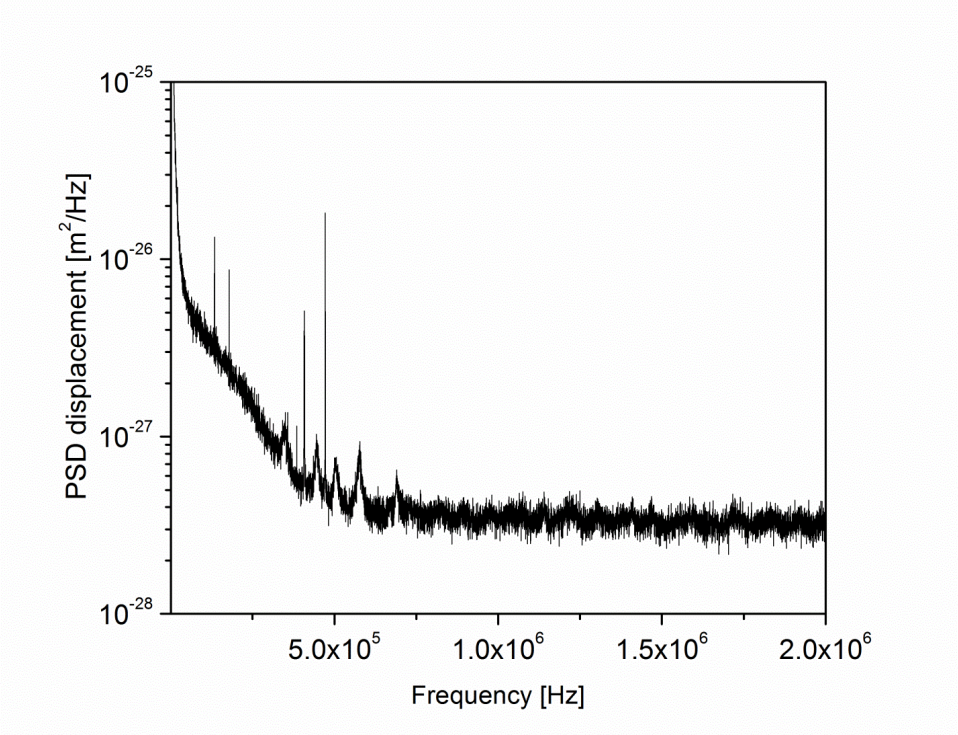

Figure 6.8: The PSD of the displacement noise measured at location P6 on the membrane.

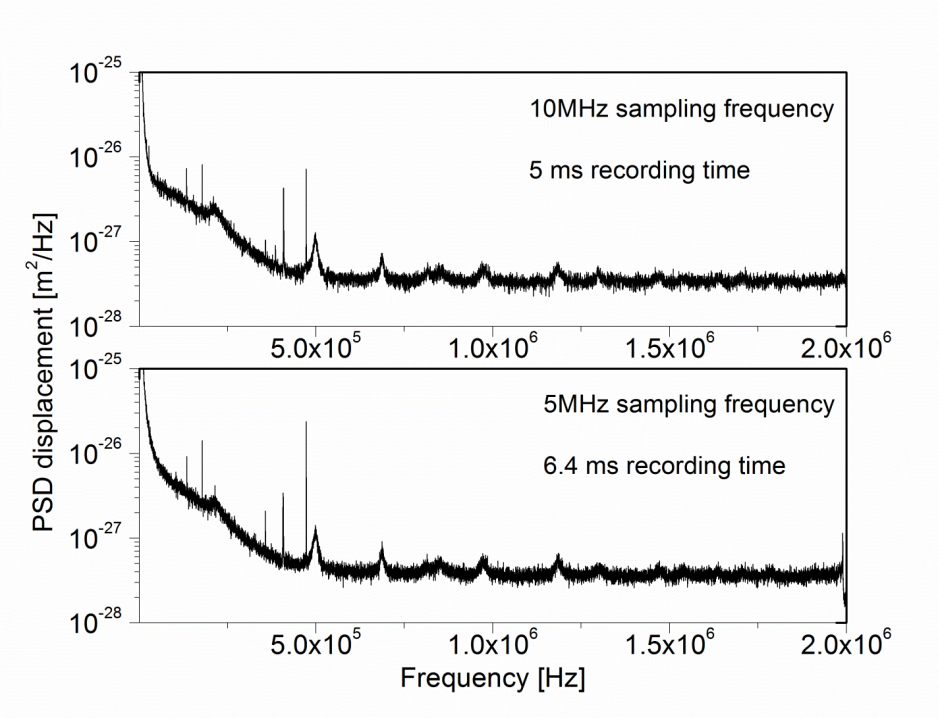

Figure 6.9: Aliasing check for the noise measured at location P1.

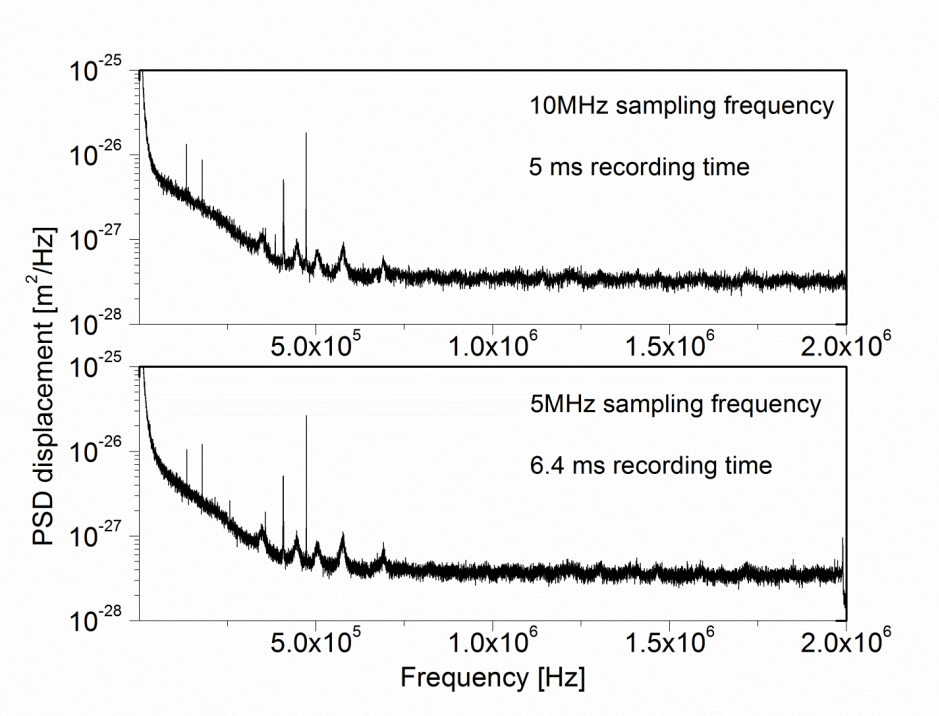

Figure 6.10: Aliasing check of the noise measured at location P6.

A comparison of noise measured at location P1 and P6, Figures 6.7 and 6.8 respectively, shows that not all of the resonance peaks are observed at each measurement location. Therefore, the first five most prominent TMN peaks are fit to extract the *Q* and the results are listed in Table 6-2. Each measurement in Table 6-2 is the average of the damping values extracted from the TMN observed at five different locations on the membrane. The measured damping and resonance frequency are discussed in the next section.

Table 6-2: The estimate of the resonance frequency and *Q* obtained from a measurement of the TMN of a nanomembrane resonator. Each measurement is the average of five values where each value corresponds to a unique interrogated location, which is noted. The error is the standard deviation as a percentage of the mean.

Interrogated location	P5-P9	P2-P6, P8	P1,P2,P4,P6,P8	P2-P6	P1-P4, P6
Frequency	346 kHz (±0.3%)	451.3 kHz (±3%)	503 kHz (±0.5%)	575.5 kHz (±0.2%)	688.5 kHz (±0.2%)
Q	27 (±38%)	38 (±15 %)	33 (±7%)	45 (±9%)	63 (±9%)

6.4 Discussion

The magnitude of the damping for this specimen is in agreement with damping values reported in [138] for a similar thin-film nanomembrane resonator measured in air. In that reference, there is no quote for the precision of the damping measurements. Therefore, the precision is evaluated with respect to the damping extracted from the TMN of a microcantilever beam resonator, Specimen 4, measured at atmospheric pressure. The PSD of the analyzed TMN resonance peaks for both resonators have comparable numbers of data points. However, the frequency resolution of the measured noise for the microcantilever beam is significantly greater, allowing for more data averaging.

The damping measured from the TMN of microcantilever Specimen 4 is $Q = 327$ (± 2%). The better precision can be attributed to the reduced variance of the noise due to high averaging factors and, also, to the low magnitude of the LDV noise floor with respect to the TMN. For the nanomembrane, the 346 kHz resonance peak occurs where the $1/f$ noise is still dominant and the Lorentzian function does not include a fitting term for the $1/f$ noise floor. This noise is still present up to ~475 kHz. The *Q* measured at the higher frequency peaks, where the $1/f$ noise is

absent, has a better precision. Still, the noise data that is analyzed for the nanomembrane has a greater variance than the noise of the microcantilever beam. The variance of the noise affects the precision of the estimate of the *Q*.

An analysis of the measured resonance frequencies suggests that the conditions of the membrane are not ideal. The first mode resonance frequency is assigned to the lowest frequency resonance peak, at 213 kHz. For this resonance frequency, the higher modes are estimated using Equation 6.2 and are listed in Table 6-3 up to the (4, 4) mode.

Table 6-3: The estimated resonance frequencies of the nanomembrane resonator based on 213 kHz as the (1, 1) mode.

Resonance frequencies [kHz]		*m*			
		1	2	3	4
n	1	213	337	476	621
	2	337	426	543	674
	3	476	543	639	753
	4	621	674	753	852

The estimated higher mode resonances do not match any of the TMN resonance peaks at the interrogated locations. There are also a greater number of expected resonance peaks in the measurement bandwidth than what is experimentally measured. The latter observation may be an artifact of the number of interrogated spots. The laser spot may fall at or near nodes where the amplitude of certain vibration modes is below the noise floor. Additionally, the preferential damping of certain modes is caused by the coupling of radiative losses to the frame [44, 139, 226].

No comment can be made on the mismatch between the calculated and measured resonances because the measured frequencies cannot be associated with a certain mode number. This is one of the draw-backs of using the TMN. The definitive method to identify certain modes is typically accomplished by an observation of the mode shape [138, 227, 233]. The TMN is a white-noise and contains no phase information, thus the scanning feature of the UHF-

120 will not reveal a mode shape [168]. That being so, the mismatch between the estimated and measured frequencies is consistent with the behavior of nanomembrane resonators reported in the literature.

Additionally, the coupling of closely spaced modes distorts and shifts the resonance peaks [138, 227, 240]. Also, states of anisotropic stress disrupt the normal sequence of resonances [241]. This effect has been linked to the absorption of laser light from the LDV and local heating that changes the stress state and thus the damping and resonance frequencies [139, 230].

6.4 Summary

The UHF-120 LDV has been used to measure the noise of a composite thin film membrane resonator. The magnitude of the damping values, O(10), agrees with reports in the literature. However, the variance is as high as 38% and as low as 7%, which is greater than the precision of the Q measured for a microcantilever beam at atmospheric pressure. The comparison between these two experiments suggests that the variance of the noise PSD and presence of $1/f$ noise cause a greater error for the estimate of damping from the TMN of the nanomembrane resonator.

The analysis of the resonance frequencies suggests that the behaviour of the nanomembrane is not ideal. The (1, 1) resonance frequency is assigned to the TMN peak at 213 kHz and is used to predict the expected higher modes. However, the estimated higher mode resonances do not match the measured TMN noise peaks.

This mismatch of the theoretical and measured frequencies also highlights the challenges of using an LDV to measure the TMN and extract the damping. The laser spot size of the LDV is small with respect to the surface of the resonator and it is possible for measurement locations to fall at the nodes for lower mode resonances. Therefore, many single-point measurements are required to generate a complete picture of the TMN spectrum. A survey of the literature suggests that local laser heating also has the potential to bias the measured damping and resonance frequencies based on the interrogated location. Further work is necessary to determine

the impact of measurement location on the accuracy and precision of the damping and resonance frequencies measured from the TMN of nanomembrane resonators.

CHAPTER 7

Conclusions and future work

The thesis started with an introduction to MEMS based sensors and detectors. It demonstrated that damping is important for measurement sensitivity and resolution. Not only does damping contribute directly to the sensitivity, but it contributes to the characteristics of the noise floor. The large number of variables that control damping (frequency, amplitude, mode shape, etc) translates into many open areas of research. These open questions also concern the evaluation of the spectroscopic tools and methods. With respect to the host of previous work, this thesis presents an effort to objectively evaluate certain techniques that are used to measure the damping and resonance frequency and also contribute to the understanding of certain damping mechanisms.

The work in this thesis is a continuation of the work of my predecessors, Sosale and Das. Some of their materials, structures, methods, tools, and even damping measurement data have been re-cycled, improved, and extended. Based on their findings, new studies and analysis of damping mechanisms and measurement techniques are developed and introduced in this thesis. Specifically, the temperature dependence of material damping in single-crystal silicon microcantilever beams and thin aluminum films was studied and a method whereby the damping is measured from a measurement of the intrinsic thermomechanical noise was characterized. Naturally, the scope of the thesis is limited by time and resources. The accomplishments and conclusions that merit future study are detailed in the next sections

7.1 Original contributions

The thesis describes new and refined experimental methods for the measurement of damping of microresonator devices. The details are useful for precision damping measurement. The more important findings are now listed:

7.1.1 Measurement of the temperature dependence of the material damping of single-crystal silicon

A clamp and actuator that are capable of heating microcantilever beam resonators have been used to measure the temperature dependence of the damping in a set of two well characterized single-crystal silicon microcantilever beam resonators. The damping was measured at 5 ˚C increments from 20 ˚C up to 150 ˚C and calibrated with respect to the TED limit. This measured damping increased proportionally to the TED with a consistent $O(10^5)$ level of residual damping. The magnitude of the residual damping is consistent with the established clamping loss for this system. Therefore, the experiment indicates that material damping of single-crystal silicon is dominated by TED over the measured temperature range.

7.1.2 Measurement of the temperature dependence of the material damping of thin aluminum films

The two microcantilever beam specimens used to measure the temperature dependence of the material damping of single-crystal silicon were coated in ~48 nm of aluminum by e-beam evaporation. The damping of the bi-layer specimens measured at 5 ˚C increments from 20 ˚C up to 150 ˚C increased non-linearly as a function of temperature. The damping of the single-crystal silicon substrate that was previously calibrated to the TED limit was then used to calculate the internal friction of the aluminum film from the damping of the bi-layer beam. The temperature dependence of the internal friction is non-monotonic with a temperature dependent peak damping. The respective aluminum internal friction peaks are measured at 80 ˚C and 100 ˚C and the magnitude is $\delta_{IF} = 0.027$ for each specimen.

7.1.3 Characterization of the method by which damping is measured from the thermomechanical noise

A systematic routine to measure and analyze the noise of silicon based microcantilever beam resonators and to extract the damping from the TMN resonance peak has been developed. The accuracy and precision of this damping measurement technique are evaluated by comparison to the well-established logarithmic decrement of free-decay. This analysis is the first comparison of the damping of a set of well-characterized microresonators measured using two different

methods. Comparatively, measurements of damping from the TMN are as accurate but the precision is as much as 25% error. An analysis of the measurement protocols on the sources of error indicates that the estimate of the *Q* is sensitive to the number of data points in the resonance peak. Therefore, precision is lost for measurements of very low damped resonators ($Q > 10^5$) that have sharp TMN resonance peaks.

7.1.4 The measurement of the damping of a nanomembrane resonator using thermomechanical noise

The noise of a bi-layer, SiN and Al, thin-film membrane resonator has been measured using a scanning LDV. The most prominent TMN noise peaks measured at nine locations on the surface are selected and fit with a Lorentzian function to extract the damping and resonance frequency. The magnitude of the measured damping, O(10), agrees with damping values at atmospheric pressure in the literature. However, the standard error for the TMN based measurement is as low as 7% and as high 38% for five measurements at unique locations on the surface of the membrane.

7.2 Future work

Based on the work presented in this thesis, many opportunities to extend and strengthen the key findings are within reach. Accordingly, the most interesting work is described in the following sub-sections.

7.2.1 Extending the mechanical spectroscopy of the material damping of aluminum films

The temperature dependence of the material damping of ~48 nm thick nanocrystalline aluminum films was measured using two different microcantilever beam substrates. The operating frequencies of the microcantilever substrates are ~200 Hz different. Even so, the internal friction of the aluminum film coated on each beam peaked at slightly different frequencies, suggesting a temperature and frequency dependence. Extending the measurements over a greater range of substrate frequencies, metal film grain sizes, and film thicknesses can help reveal the nature of the mechanisms that are responsible for the internal friction.

7.2.2 Improving the measurement of damping from the thermomechanical noise

The factors that influence the precision of the damping measured from the TMN needs to be better understood. The systematic effects on the estimate of the Q due to the measurement protocols and analysis of the TMN were investigated, but did not show a particular bias for any specific resonator. The one major factor left unstudied is the interaction of the specimens with the environment. The specimens that are used in this study operate in a frequency range that is acoustically cluttered. During experiments, it was noted that high-Q resonators can be excited by the noise of a conversation across the room. However, the transmission of noise through solids decreases with increasing frequency [242]. A larger set of resonators spanning a greater frequency range can be used to reveal a frequency bias for the estimate of the Q from the TMN.

Additionally, the influence that the interrogated location on the microcantilever has on the measurement of the Q from the TMN is unknown. Measurements of the stiffness from the TMN for AFM cantilevers have demonstrated a strong dependence on the location of the measurement [155]. As the measurement location moves further from the end of the cantilever, the amplitude decreases and more of the noise floor will be included in the resonance peak and the impact that this has on the estimate of the Q is yet to be systematically studied.

7.2.3 Systematic study of the limitations of using thermomechanical noise to measure the damping in nanomembrane resonators

The measurement of the damping of a nanomembrane at atmospheric pressure from the TMN has a poor precision compared to a microcantilever beam. It is suggested that $1/f$ noise and the greater variance of the data contribute to the error. Repeating this experiment for a higher frequency membrane where the first mode resonance is away from the $1/f$ noise can provide further insights.

Additionally, the measured resonance frequencies do not match the expected frequencies. A review of the literature finds reports that the absorption of laser light causes local states of anisotropic stress that skew the sequence of resonance frequencies and changes the damping. This effect could be studied by systematically applying a spectrum of laser powers. Observing a

shift in the measured resonance frequencies would confirm some departure of an ideal stress state due to the absorption of the laser light.

7.3 Conclusion

This thesis continues a long history of the study of damping in micromachined structures and materials. It contributes a data set showing the temperature dependence of damping in aluminum and single-crystal silicon. The data is noteworthy because it was obtained using well-characterized instrumentation, measurement methods, and crucially, silicon microcantilever beam substrates that are calibrated to the TED limit. Thus, the magnitude of the damping values can be directly compared to other experimental data that is also calibrated to TED. The data has practical value to help engineer resonant MEMS devices away from the material damping peak.

The other objective of the thesis, to characterize the accuracy and precision of the damping measured from the TMN, is valuable for the experimentalist. This method of damping measurement is attractive because the analysis routine is simple, there is no actuator, and the measurement is non-contact. The evaluation of this method suggests that its use comes with certain trade-offs. The precision is sensitive to the sharpness of the TMN resonance peak and the number of data points available for fitting the Lorentzian function, which is problematic for high-Q resonators. Data can be "added" by increasing the recording time, but this increases the likelihood of perturbation from mechanical noises in the environment for sensitive, low damped resonators.

The results obtained for these two areas of focus provide simple guidelines for the experimental and industrial applications of resonant MEMS devices. Despite its limited focus, the thesis contains practical methods to further amend or investigate the measures and measurements of damping. The description of the experimental methods and analysis procedures were written with the researcher in mind. For instance, the impact of the measurement and analysis protocols was systematically determined for the damping measured by the logarithmic of free-decay and from the TMN. Often, the nuanced but significant details of experimental practice and analysis are left out of published works.

At its most conceptual, the thesis presents the methods that are used to obtain measurements of damping. At its most tangible, the thesis presents calibrated measurements of the temperature dependence of the material damping of single-crystal silicon and thin films of nanocrystalline aluminum. Both of these aspects of the thesis can be applied by the engineer to advance the applications and performance of resonant MEMS devices.

References

[1] K. E. Petersen, "Silicon as a mechanical material," *Proceedings of the IEEE,* vol. 70, pp. 420-457, 1982.

[2] R. P. Feynman, "There's plenty of room at the bottom [data storage]," *Journal of Microelectromechanical Systems,* vol. 1, pp. 60-66, 1992.

[3] T. Burg and S. Manalis, "Microfluidic packaging of suspended microchannel resonators for biomolecular detection," in *Microtechnology in Medicine and Biology, 2005. 3rd IEE/EMBS Special Topic Conference*, 2005, pp. 264-267.

[4] A.-S. Duwez and N. Willet, *Molecular manipulation with atomic force microscopy*: CRC Press, 2011.

[5] T. P. Burg, M. Godin, S. M. Knudsen, W. Shen, G. Carlson, J. S. Foster, *et al.*, "Weighing of biomolecules, single cells and single nanoparticles in fluid," *Nature,* vol. 446, pp. 1066-1069, 2007.

[6] L. Gross, F. Mohn, N. Moll, P. Liljeroth, and G. Meyer, "The chemical structure of a molecule resolved by atomic force microscopy," *Science,* vol. 325, pp. 1110-1114, 2009.

[7] D. Rugar, R. Budakian, H. Mamin, and B. Chui, "Single spin detection by magnetic resonance force microscopy," *Nature,* vol. 430, pp. 329-332, 2004.

[8] T. A. Roessig, R. T. Howe, A. P. Pisano, and J. H. Smith, "Surface-micromachined resonant accelerometer," in *Solid State Sensors and Actuators, 1997. TRANSDUCERS'97 Chicago., 1997 International Conference on*, 1997, pp. 859-862.

[9] T. Albrecht, P. Grutter, D. Horne, and D. Rugar, "Frequency modulation detection using high-Q cantilevers for enhanced force microscope sensitivity," *Journal of Applied Physics,* vol. 69, pp. 668-673, 1991.

[10] K. Y. Yasumura, T. D. Stowe, E. M. Chow, T. Pfafman, T. W. Kenny, B. C. Stipe, *et al.*, "Quality factors in micron and submicron-thick cantilevers," *Journal of Microelectromechanical Systems,* vol. 9, pp. 117-125, 2000.

[11] J. Yang, T. Ono, and M. Esashi, "Energy dissipation in submicrometer thick single-crystal silicon cantilevers," *Journal of Microelectromechanical Systems,* vol. 11, pp. 775-783, 2002.

[12] K. Ekinci, Y. Yang, and M. Roukes, "Ultimate limits to inertial mass sensing based upon nanoelectromechanical systems," *Journal of Applied Physics,* vol. 95, p. 2682, 2004.

[13] J. Arlett and M. Roukes, "Ultimate and practical limits of fluid-based mass detection with suspended microchannel resonators," *Journal of Applied Physics,* vol. 108, pp. 084701-084701-11, 2010.

[14] P. R. Saulson, "Thermal noise in mechanical experiments," *Physical Review D,* vol. 42, pp. 2437-2445, 1990.

[15] T. B. Gabrielson, "Mechanical-thermal noise in micromachined acoustic and vibration sensors," *IEEE Transactions on Electron Devices,* vol. 40, pp. 903-909, 1993.

[16] W. Osten, *Optical Inspection of Microsystems*: CRC Press, 2006.

[17] G. Sosale, "A microcantilever platform for measuring internal friction in thin films using thermoelastic damping for calibration," McGill University Libraries, Montreal, 2011.

[18] G. Sosale, S. Prabhakar, L. Frechette, and S. Vengallatore, "Effect of thin aluminum coatings on structural damping of silicon microresonators," in *MRS Proceedings,* 2009, pp. 1222-DD01-06.

[19] L. Sekaric, D. Carr, S. Evoy, J. Parpia, and H. Craighead, "Nanomechanical resonant structures in silicon nitride: fabrication, operation and dissipation issues," *Sensors and Actuators A: Physical,* vol. 101, pp. 215-219, 2002.

[20] R. Sandberg, K. Mølhave, A. Boisen, and W. Svendsen, "Effect of gold coating on the Q-factor of a resonant cantilever," *Journal of Micromechanics and Microengineering,* vol. 15, p. 2249, 2005.

[21] A. R. Klempner, R. T. Marinis, P. Hefti, and R. J. Pryputniewicz, "Experimental Determination of the Q-factors of Microcantilevers Coated With Thin Metal Films," *Strain,* vol. 45, pp. 295-300, 2009.

[22] R. Buser and N. De Rooij, "Resonant silicon structures," *Sensors and Actuators,* vol. 17, pp. 145-154, 1989.

[23] B. W. Chui, T. D. Stowe, Y. S. Ju, K. E. Goodson, T. W. Kenny, H. J. Mamin, *et al.*, "Low-stiffness silicon cantilevers with integrated heaters and piezoresistive sensors for high-density AFM thermomechanical data storage," *Journal of Microelectromechanical Systems,* vol. 7, pp. 69-78, 1998.

[24] G. Stemme, "Resonant silicon sensors," *Journal of Micromechanics and Microengineering,* vol. 1, pp. 113-125, 1991.

[25] F. Shen, P. Lu, S. O'Shea, K. Lee, and T. Ng, "Thermal effects on coated resonant microcantilevers," *Sensors and Actuators A: Physical,* vol. 95, pp. 17-23, 2001.

[26] "Introduction to Bruker's ScanAsyst and PeakForce Tapping AFM Technology, Application Note 133," in *www.bruker.com*, ed. Santa Barbara, CA, USA: Bruker Corporation, 2011.

[27] D. J. Inman and R. C. Singh, *Engineering Vibration* vol. 3: Prentice Hall Upper Saddle River, 2001.

[28] U. Gysin, S. Rast, P. Ruff, E. Meyer, D. Lee, P. Vettiger, *et al.*, "Temperature dependence of the force sensitivity of silicon cantilevers," *Physical Review B,* vol. 69, p. 045403, 2004.

[29] M. W. Fairbairn, S. Moheimani, and A. J. Fleming, "Control of an atomic force microscope microcantilever: a sensorless approach," *Journal of Microelectromechanical Systems,* vol. 20, pp. 1372-1381, 2011.

[30] J. R. Lozano, D. Kiracofe, J. Melcher, R. Garcia, and A. Raman, "Calibration of higher eigenmode spring constants of atomic force microscope cantilevers," *Nanotechnology,* vol. 21, p. 465502, 2010.

[31] S. Rast, C. Wattinger, U. Gysin, and E. Meyer, "The noise of cantilevers," *Nanotechnology,* vol. 11, p. 169, 2000.

[32] T. Bagci, A. Simonsen, S. Schmid, L. G. Villanueva, E. Zeuthen, J. Appel, *et al.*, "Optical detection of radio waves through a nanomechanical transducer," *Nature,* vol. 507, pp. 81-85, 2014.

[33] N. Yazdi, F. Ayazi, and K. Najafi, "Micromachined inertial sensors," *Proceedings of the IEEE,* vol. 86, pp. 1640-1659, 1998.

[34] Y. Yang, C. Callegari, X. Feng, K. Ekinci, and M. Roukes, "Zeptogram-scale nanomechanical mass sensing," *Nano Letters,* vol. 6, pp. 583-586, 2006.

[35] J. A. Sidles, J. L. Garbini, K. Bruland, D. Rugar, O. Züger, S. Hoen, *et al.*, "Magnetic resonance force microscopy," *Reviews of Modern Physics,* vol. 67, p. 249, 1995.

[36] S. Joshi, S. Hung, and S. Vengallatore, "Design strategies for controlling damping in micromechanical and nanomechanical resonators," *EPJ Techniques and Instrumentation,* vol. 1, p. 5, 2014.

[37] J. Woodhouse, "Linear damping models for structural vibration," *Journal of Sound and Vibration,* vol. 215, pp. 547-569, 1998.

[38] X. Liu, J. Vignola, H. Simpson, B. Lemon, B. Houston, and D. Photiadis, "A loss mechanism study of a very high Q silicon micromechanical oscillator," *Journal of Applied Physics,* vol. 97, p. 023524, 2005.

[39] Y. Jimbo and K. Itao, "Energy loss of a cantilever vibrator," *Journal of the Horological Institute of Japan,* vol. 47, pp. 1-15, 1968.

[40] Z. Hao, A. Erbil, and F. Ayazi, "An analytical model for support loss in micromachined beam resonators with in-plane flexural vibrations," *Sensors and Actuators A: Physical,* vol. 109, pp. 156-164, 2003.

[41] J. A. Judge, D. M. Photiadis, J. F. Vignola, B. H. Houston, and J. Jarzynski, "Attachment loss of micromechanical and nanomechanical resonators in the limits of thick and thin support structures," *Journal of Applied Physics,* vol. 101, p. 013521, 2007.

[42] D. M. Photiadis and J. A. Judge, "Attachment losses of high Q oscillators," *Applied Physics Letters,* vol. 85, pp. 482-484, 2004.

[43] Y-H. Park and K. C. Park, "High-fidelity modeling of MEMS resonators. Part I. Anchor loss mechanisms through substrate," *Journal of Microelectromechanical Systems,* vol. 13, pp. 238-247, 2004.

[44] I. Wilson-Rae, R. Barton, S. Verbridge, D. Southworth, B. Ilic, H. Craighead, *et al.*, "High-Q nanomechanics via destructive interference of elastic waves," *Physical Review Letters,* vol. 106, p. 047205, 2011.

[45] D. S. Bindel and S. Govindjee, "Elastic PMLs for resonator anchor loss simulation," *International Journal for Numerical Methods in Engineering,* vol. 64, pp. 789-818, 2005.

[46] W-T. Hsu, J. R. Clark, and C. T. Nguyen, "Q-optimized lateral free-free beam micromechanical resonators," in *11th International Conference on Solid-State Sensors and Actuators, Munich, Germany,* 2001, pp. 1110-1113.

[47] P-L. Yu, K. Cicak, N. Kampel, Y. Tsaturyan, T. Purdy, R. Simmonds, *et al.*, "A phononic bandgap shield for high-q membrane microresonators," *Applied Physics Letters,* vol. 104, p. 023510, 2014.

[48] B. Harrington and R. Abdolvand, "In-plane acoustic reflectors for reducing effective anchor loss in lateral–extensional MEMS resonators," *Journal of Micromechanics and Microengineering,* vol. 21, p. 085021, 2011.

[49] K. Wang, A-C. Wong, and C. T. Nguyen, "VHF free-free beam high-Q micromechanical resonators," *Journal of Microelectromechanical Systems,* vol. 9, pp. 347-360, 2000.

[50] A. Ferguson, L. Li, V. Nagaraj, B. Balachandran, B. Piekarski, and D. DeVoe, "Modeling and design of composite free–free beam piezoelectric resonators," *Sensors and Actuators A: Physical,* vol. 118, pp. 63-69, 2005.

[51] M. Pandey, R. B. Reichenbach, A. T. Zehnder, A. Lal, and H. G. Craighead, "Reducing anchor loss in MEMS resonators using mesa isolation," *Journal of Microelectromechanical Systems,* vol. 18, pp. 836-844, 2009.

[52] B. Le Foulgoc, T. Bourouina, O. Le Traon, A. Bosseboeuf, F. Marty, C. Breluzeau, *et al.*, "Highly decoupled single-crystal silicon resonators: an approach for the intrinsic quality factor," *Journal of Micromechanics and Microengineering,* vol. 16, p. S45, 2006.

[53] S. W. Yoon, S. Lee, N. C. Perkins, and K. Najafi, "Analysis and wafer-level design of a high-order silicon vibration isolator for resonating MEMS devices," *Journal of Micromechanics and Microengineering,* vol. 21, p. 015017, 2011.

[54] Y. Tsaturyan, A. Barg, A. Simonsen, L. G. Villanueva, S. Schmid, A. Schliesser, *et al.*, "Demonstration of suppressed phonon tunneling losses in phononic bandgap shielded membrane resonators for high-Q optomechanics," *Optics express,* vol. 22, pp. 6810-6821, 2014.

[55] S. Mohammadi and A. Adibi, "Waveguide-Based Phononic Crystal Micro/Nanomechanical High-Q Resonators," *Journal of Microelectromechanical Systems,* vol. 21, pp. 379-384, 2012.

[56] M. Cross and R. Lifshitz, "Elastic wave transmission at an abrupt junction in a thin plate with application to heat transport and vibrations in mesoscopic systems," *Physical Review B,* vol. 64, p. 085324, 2001.

[57] I. Wilson-Rae, "Intrinsic dissipation in nanomechanical resonators due to phonon tunneling," *Physical Review B,* vol. 77, p. 245418, 2008.

[58] G. D. Cole, I. Wilson-Rae, K. Werbach, M. R. Vanner, and M. Aspelmeyer, "Phonon-tunnelling dissipation in mechanical resonators," *Nature Communications,* vol. 2, p. 231, 2011.

[59] F. Blom, S. Bouwstra, M. Elwenspoek, and J. Fluitman, "Dependence of the quality factor of micromachined silicon beam resonators on pressure and geometry," *Journal of Vacuum Science & Technology B,* vol. 10, pp. 19-26, 1992.

[60] A. Pandey, R. Pratap, and F. Chau, "Effect of pressure on fluid damping in MEMS torsional resonators with flow ranging from continuum to molecular regime," *Experimental Mechanics,* vol. 48, pp. 91-106, 2008.

[61] O. Svitelskiy, V. Sauer, N. Liu, K-M. Cheng, E. Finley, M. R. Freeman, *et al.*, "Pressurized fluid damping of nanoelectromechanical systems," *Physical Review Letters,* vol. 103, p. 244501, 2009.

[62] C. Zener, "Internal friction in solids. I. Theory of internal friction in reeds," *Physical Review,* vol. 52, p. 230, 1937.

[63] C. Zener, "Internal friction in solids II. General theory of thermoelastic internal friction," *Physical Review,* vol. 53, p. 90, 1938.

[64] J. E. Bishop and V. K. Kinra, "Elastothermodynamic damping in laminated composites," *International Journal of Solids and Structures,* vol. 34, pp. 1075-1092, 1997.

[65] V. Kinra and K. Milligan, "A second-law analysis of thermoelastic damping," *Journal of Applied Mechanics,* vol. 61, pp. 71-76, 1994.

[66] K. Milligan and V. Kinra, "On the thermoelastic damping of a one-dimensional inclusion in a uniaxial bar," *Mechanics Research Communications,* vol. 20, pp. 137-142, 1993.

[67] S. Prabhakar and S. Vengallatore, "Theory of thermoelastic damping in micromechanical resonators with two-dimensional heat conduction," *Journal of Microelectromechanical Systems,* vol. 17, pp. 494-502, 2008.

[68] S. Prabhakar and S. Vengallatore, "Thermoelastic damping in bilayered micromechanical beam resonators," *Journal of Micromechanics and Microengineering,* vol. 17, p. 532, 2007.

[69] S. Prabhakar and S. Vengallatore, "Thermoelastic damping in hollow and slotted microresonators," *Journal of Microelectromechanical Systems,* vol. 18, pp. 725-735, 2009.

[70] S. Vengallatore, "Analysis of thermoelastic damping in laminated composite micromechanical beam resonators," *Journal of Micromechanics and Microengineering,* vol. 15, p. 2398, 2005.

[71] Z. Nourmohammadi, S. Mukherjee, S. Joshi, J. Song, and S. Vengallatore, "Methods for Atomistic Simulations of Linear and Nonlinear Damping in Nanomechanical Resonators," *Journal of Microelectromechanical Systems,* vol. 24, pp 1462-1470, 2015.

[72] V. Srikar and S. D. Senturia, "Thermoelastic damping in fine-grained polysilicon flexural beam resonators," *Journal of Microelectromechanical Systems,* vol. 11, pp. 499-504, 2002.

[73] R. Abdolvand, G. K. Ho, A. Erbil, and F. Ayazi, "Thermoelastic damping in trench-refilled polysilicon resonators," in *TRANSDUCERS, 12th International Conference on Solid-State Sensors, Actuators and Microsystems, 2003*, 2003, pp. 324-327.

[74] A. Duwel, R. N. Candler, T. W. Kenny, and M. Varghese, "Engineering MEMS resonators with low thermoelastic damping," *Journal of Microelectromechanical Systems,* vol. 15, pp. 1437-1445, 2006.

[75] S. A. Chandorkar, R. N. Candler, A. Duwel, R. Melamud, M. Agarwal, K. E. Goodson, *et al.*, "Multimode thermoelastic dissipation," *Journal of Applied Physics,* vol. 105, p. 043505, 2009.

[76] A. H. Nayfeh and M. I. Younis, "Modeling and simulations of thermoelastic damping in microplates," *Journal of Micromechanics and Microengineering,* vol. 14, p. 1711, 2004.

[77] A. N. Norris, "Dynamics of thermoelastic thin plates: a comparison of four theories," *Journal of Thermal Stresses,* vol. 29, pp. 169-195, 2006.

[78] J. Baur and A. Kulik, "Optimal sample shape for internal friction measurements using a dual cantilevered beam," *Journal of Applied Physics,* vol. 58, pp. 1489-1492, 1985.

[79] H. Nouira, E. Foltête, B. Ait Brik, L. Hirsinger, and S. Ballandras, "Experimental characterization and modeling of microsliding on a small cantilever quartz beam," *Journal of Sound and Vibration,* vol. 317, pp. 30-49, 2008.

[80] R. Kleiman, G. Kaminsky, J. Reppy, R. Pindak, and D. Bishop, "Single-crystal silicon high-Q torsional oscillators," *Review of scientific instruments,* vol. 56, pp. 2088-2091, 1985.

[81] A. Borrielli, M. Bonaldi, E. Serra, A. Bagolini, and L. Conti, "Wideband mechanical response of a high-Q silicon double-paddle oscillator," *Journal of Micromechanics and Microengineering,* vol. 21, p. 065019, 2011.

[82] M. Bao and H. Yang, "Squeeze film air damping in MEMS," *Sensors and Actuators A: Physical,* vol. 136, pp. 3-27, 2007.

[83] S. D. Senturia, *Microsystem Design*: Springer Science & Business Media, 2007.

[84] K. Kunal and N. Aluru, "Akhiezer damping in nanostructures," *Physical Review B,* vol. 84, p. 245450, 2011.

[85] A. Kiselev and G. Iafrate, "Phonon dynamics and phonon assisted losses in Euler-Bernoulli nanobeams," *Physical Review B,* vol. 77, p. 205436, 2008.

[86] A. N. Cleland, *Foundations of Nanomechanics: From Solid-State Theory to Device Applications*: Springer Science & Business Media, 2013.

[87] R. S. Lakes, *Viscoelastic Materials*: Cambridge University Press, 2009.

[88] S. D. Vishwakarma, A. K. Pandey, J. M. Parpia, D. R. Southworth, H. G. Craighead, and R. Pratap, "Evaluation of mode dependent fluid damping in a high frequency drumhead microresonator," *Journal of Microelectromechanical Systems,* vol. 23, pp. 334-346, 2014 2014.

[89] V. B. Braginsky, V. Mitrofanov, V. I. Panov, and C. Eller, *Systems with Small Dissipation*: University of Chicago Press, 1985.

[90] S. Rinaldi, S. Prabhakar, S. Vengallatore, and M. P. Paidoussis, "Dynamics of microscale pipes containing internal fluid flow: Damping, frequency shift, and stability," *Journal of Sound and Vibration,* vol. 329, pp. 1081-1088, 2010.

[91] J. E. Sader, T. P. Burg, and S. R. Manalis, "Energy dissipation in microfluidic beam resonators," *Journal of Fluid Mechanics,* vol. 1, pp. 1-36, 2006.

[92] C. Zener, *Elasticity and Anelasticity of Metals*: University of Chicago press, 1948.

[93] B. Berry and W. Pritchet, "Vibrating reed internal friction apparatus for films and foils," *IBM Journal of Research and Development,* vol. 19, pp. 334-343, 1975.

[94] A. Nowick and B. Berry, "Anelastic relaxation in crystalline solids, 1972," *Academic, New York*.

[95] M. Prieler, H. Bohn, W. Schilling, and H. Trinkaus, "Grain boundary sliding in thin substrate-bonded Al films," *Journal of Alloys and Compounds,* vol. 211, pp. 424-427, 1994.

[96] D-H. Choi, H. Kim, and W. D. Nix, "Anelasticity and damping of thin aluminum films on silicon substrates," *Journal of Microelectromechanical Systems,* vol. 13, pp. 230-237, 2004.

[97] G. Sosale, D. Almecija, K. Das, and S. Vengallatore, "Mechanical spectroscopy of nanocrystalline aluminum films: effects of frequency and grain size on internal friction," *Nanotechnology,* vol. 23, p. 155701, 2012.

[98] G. Sosale, S. Prabhakar, L. G. Fréchette, and S. Vengallatore, "A microcantilever platform for measuring internal friction in thin films using thermoelastic damping for calibration," *Journal of Microelectromechanical Systems,* vol. 20, pp. 764-773, 2011.

[99] S. Vengallatore, "Gorsky damping in nanomechanical structures," *Scripta materialia,* vol. 52, pp. 1265-1268, 2005.

[100] P.-L. Yu, T. Purdy, and C. Regal, "Control of material damping in high-Q membrane microresonators," *Physical Review Letters,* vol. 108, p. 083603, 2012.

[101] A. Zhu, H. Bohn, and W. Schilling, "Internal friction associated with grain boundary diffusion in thin gold films," *Philosophical Magazine A,* vol. 72, pp. 805-812, 1995.

[102] T. Ono and M. Esashi, "Effect of ion attachment on mechanical dissipation of a resonator," *Applied Physics Letters,* vol. 87, p. 044105, 2005.

[103] P. Paolino and L. Bellon, "Frequency dependence of viscous and viscoelastic dissipation in coated micro-cantilevers from noise measurement," *Nanotechnology,* vol. 20, p. 405705, 2009.

[104] K. Uozumi, H. Honda, and A. Kinbara, "Internal friction of vacuum-deposited silver films," *Journal of Applied Physics,* vol. 49, pp. 249-252, 1978.

[105] X. Liu, E. Thompson, B. White Jr, and R. Pohl, "Low-temperature internal friction in metal films and in plastically deformed bulk aluminum," *Physical Review B,* vol. 59, p. 11767, 1999.

[106] S. Hung, "Damping due to Attachment Losses in Microresonators," Master of Engineering, Department of Mechanical Engineering, McGill University, Montreal, Quebec, 2012.

[107] R. Schwarz and L. Funk, "Internal-friction study of solute segregation to dislocations," *Acta Metallurgica,* vol. 31, pp. 299-315, 1983.

[108] C. Boerner and K.-H. Robrock, "Internal friction studies of heavy interstitial impurity atoms," *Le Journal de Physique Colloques,* vol. 46, pp. C10-55-C10-58, 1985.

[109] S. Yang, R. Gibson, G. Crosbie, and R. Allor, "Measurement of Dynamic Mechanical Properties of Advanced Ceramics and Ceramic Matrix Composites at Temperatures Above 1000 C," *Experimental Techniques,* vol. 20, pp. 20-23, 1996.

[110] S. Reid, G. Cagnoli, D. Crooks, J. Hough, P. Murray, S. Rowan, *et al.*, "Mechanical dissipation in silicon flexures," *Physics Letters A,* vol. 351, pp. 205-211, 2006.

[111] F-C. Hsu, J-C. Hsu, T-C. Huang, C-H. Wang, and P. Chang, "Design of lossless anchors for microacoustic-wave resonators utilizing phononic crystal strips," *Applied Physics Letters,* vol. 98, p. 143505, 2011.

[112] H. Hosaka, K. Itao, and S. Kuroda, "Damping characteristics of beam-shaped micro-oscillators," *Sensors and Actuators A: Physical,* vol. 49, pp. 87-95, 1995.

[113] H. Nouira, E. Foltête, L. Hirsinger, and S. Ballandras, "Investigation of the effects of air on the dynamic behavior of a small cantilever beam," *Journal of Sound and Vibration,* vol. 305, pp. 243-260, 2007.

[114] B. S. Berry, "Damping mechanisms in thin-layer materials," *M3D: Mechanics and Mechanisms of Material Damping,* p. 28, 1992.

[115] S. P. Baker, R. P. Vinci, and T. Arias, "Elastic and anelastic behavior of materials in small dimensions," *MRS bulletin,* vol. 27, pp. 26-29, 2002.

[116] J. C. Irvin, "Resistivity of bulk silicon and of diffused layers in silicon," *Bell System Technical Journal,* vol. 41, pp. 387-410, 1962.

[117] T. V. Roszhart, "The effect of thermoelastic internal friction on the Q of micromachined silicon resonators," in *Solid-State Sensor and Actuator Workshop, 1990. 4th Technical Digest., IEEE,* 1990, pp. 13-16.

[118] R. N. Candler, A. Duwel, M. Varghese, S. A. Chandorkar, M. A. Hopcroft, W.T. Park, *et al.,* "Impact of geometry on thermoelastic dissipation in micromechanical resonant beams," *Journal of Microelectromechanical Systems,* vol. 15, pp. 927-934, 2006.

[119] R. Lifshitz, "Phonon-mediated dissipation in micro- and nano-mechanical systems," *Physica B: Condensed Matter,* vol. 316, pp. 397-399, 2002.

[120] R. Gibson and R. Plunkett, "A forced-vibration technique for measurement of material damping," *Experimental Mechanics,* vol. 17, pp. 297-302, 1977.

[121] C. W. De Silva, *Vibration: Fundamentals and Practice*: CRC press, 2006.

[122] E. J. Graesser and C. R. Wong, "The relationship of traditional damping measures for materials with high damping capacity: a review," in *Symposium on M3D: Mechanics and Mechanisms of Material Damping, VK Kinra, and A. Wolfenden, eds., American Society for Testing Materials, Philadelphia,* 1992, pp. 316-343.

[123] M. L. James, G. M. Smith, J. Wolford, and P. Whaley, *Vibration of Mechanical and Structural Systems: With Microcomputer Applications*: HarperCollins College Publishers, 1994.

[124] N. Shalabi, "Design, assembly and validation of a system for measuring damping in microresonators," McGill University Libraries, Montreal, 2011.

[125] U. Harms, L. Kempen, and H. Neuhäuser, "Vibrating reed apparatus with optical detection and digital signal processing: Application to measurements on thin films," *Review of Scientific Instruments,* vol. 70, pp. 1751-1755, 1999.

[126] M. Tudor, M. Andres, K. Foulds, and J. Naden, "Silicon resonator sensors: interrogation techniques and characteristics," in *IEEE Proceedings D (Control Theory and Applications),* 1988, pp. 364-368.

[127] L. E. Drain, *The Laser Doppler Technique*. Chichester [England]; New York: J. Wiley, 1980.

[128] P. Castellini, M. Martarelli, and E. P. Tomasini, "Laser Doppler Vibrometry: Development of advanced solutions answering to technology's needs," *Mechanical Systems and Signal Processing,* vol. 20, pp. 1265-1285, 2006.

[129] Y. Yeh and H. Cummins, "Localized fluid flow measurements with an He–Ne laser spectrometer," *Applied Physics Letters,* vol. 4, pp. 176-178, 1964.

[130] D. Photiadis, B. Houston, X. Liu, J. Bucaro, and M. Marcus, "Thermoelastic loss observed in a high Q mechanical oscillator," *Physica B: Condensed Matter,* vol. 316, pp. 408-410, 2002.

[131] S. Schmid, K. Jensen, K. Nielsen, and A. Boisen, "Damping mechanisms in high-Q micro and nanomechanical string resonators," *Physical Review B,* vol. 84, p. 165307, 2011.

[132] J. Lu, T. Ikehara, Y. Zhang, T. Mihara, and R. Maeda, "Mechanical quality factor of microcantilevers for mass sensing applications," in *Microelectronics, MEMS, and Nanotechnology,* 2007, pp. 68001Y-68001Y-8.

[133] J. Yang, T. Ono, and M. Esashi, "Investigating surface stress: surface loss in ultrathin single-crystal silicon cantilevers," *Journal of Vacuum Science & Technology B,* vol. 19, pp. 551-556, 2001.

[134] J. Yang, T. Ono, and M. Esashi, "Mechanical behavior of ultrathin microcantilever," *Sensors and Actuators A: Physical,* vol. 82, pp. 102-107, 2000.

[135] M. Belov, N. Quitoriano, S. Sharma, W. Hiebert, T. Kamins, and S. Evoy, "Mechanical resonance of clamped silicon nanowires measured by optical interferometry," *Journal of Applied Physics,* vol. 103, pp. 74304-74304, 2008.

[136] W. Zhang and K. Turner, "Frequency dependent fluid damping of micro/nano flexural resonators: Experiment, model and analysis," *Sensors and Actuators A: Physical,* vol. 134, pp. 594-599, 2007.

[137] D. Southworth, R. Barton, S. Verbridge, B. Ilic, A. Fefferman, H. Craighead, *et al.*, "Stress and silicon nitride: A crack in the universal dissipation of glasses," *Physical Review Letters,* vol. 102, p. 225503, 2009.

[138] O. Trushkevych, V. A. Shah, M. Myronov, J. E. Halpin, S. D. Rhead, M. J. Prest, *et al.*, "Laser-vibrometric ultrasonic characterization of resonant modes and quality factors of Ge membranes," *Science and Technology of Advanced Materials,* vol. 15, p. 025004, 2014.

[139] A. Jöckel, M. T. Rakher, M. Korppi, S. Camerer, D. Hunger, M. Mader, *et al.*, "Spectroscopy of mechanical dissipation in micro-mechanical membranes," *Applied Physics Letters,* vol. 99, p. 143109, 2011.

[140] M. Kajima, N. Kusumi, S. Moriwaki, and N. Mio, "Wide-band measurement of mechanical thermal noise using a laser interferometer," *Physics Letters A,* vol. 263, pp. 21-26, 1999.

[141] E. Serra, A. Borrielli, F. Cataliotti, F. Marin, F. Marino, A. Pontin, *et al.*, "Ultralow-dissipation micro-oscillator for quantum optomechanics," *Physical Review A,* vol. 86, p. 051801, 2012.

[142] J. Yang, T. Ono, and M. Esashi, "Surface effects and high quality factors in ultrathin single-crystal silicon cantilevers," *Applied Physics Letters,* vol. 77, pp. 3860-3862, 2000.

[143] D. F. Wang, T. Ono, and M. Esashi, "Crystallographic influence on nanomechanics of (100)-oriented silicon resonators," *Applied Physics Letters,* vol. 83, pp. 3189-3191, 2003.

[144] T. Ono, X. Li, H. Miyashita, and M. Esashi, "Mass sensing of adsorbed molecules in sub-picogram sample with ultrathin silicon resonator," *Review of Scientific Instruments,* vol. 74, pp. 1240-1243, 2003.

[145] X. Liu, H. Haucke, J. Vignola, H. Simpson, J. Baldwin, B. Houston, *et al.*, "Understanding the internal friction of a silicon micro-mechanical oscillator," *Materials Science and Engineering: A,* vol. 521, pp. 389-392, 2009.

[146] G. Sosale, K. Das, L. Fréchette, and S. Vengallatore, "Controlling damping and quality factors of silicon microcantilevers by selective metallization," *Journal of Micromechanics and Microengineering,* vol. 21, p. 105010, 2011.

[147] K. Das, G. Sosale, and S. Vengallatore, "Design, implementation, and application of a microresonator platform for measuring energy dissipation by internal friction in nanowires," *Nanotechnology,* vol. 23, p. 505703, 2012.

[148] A. Labuda, M. Lysy, W. Paul, Y. Miyahara, P. Grütter, R. Bennewitz, *et al.*, "Stochastic noise in atomic force microscopy," *Physical Review E,* vol. 86, p. 031104, 2012.

[149] D. Kiracofe, M. Yazdanpanah, and A. Raman, "Mass and stiffness calibration of nanowires using thermally driven vibration," *Nanotechnology,* vol. 22, p. 295504, 2011.

[150] N. A. Burnham, X. Chen, C. Hodges, G. Matei, E. Thoreson, C. Roberts, *et al.*, "Comparison of calibration methods for atomic-force microscopy cantilevers," *Nanotechnology,* vol. 14, p. 1, 2003.

[151] G. Matei, E. Thoreson, J. Pratt, D. Newell, and N. Burnham, "Precision and accuracy of thermal calibration of atomic force microscopy cantilevers," *Review of Scientific Instruments,* vol. 77, p. 083703, 2006.

[152] R. S. Gates and J. R. Pratt, "Accurate and precise calibration of AFM cantilever spring constants using laser Doppler vibrometry," *Nanotechnology,* vol. 23, p. 375702, 2012.

[153] R. Levy and M. Maaloum, "Measuring the spring constant of atomic force microscope cantilevers: thermal fluctuations and other methods," *Nanotechnology,* vol. 13, p. 33, 2002.

[154] B. Ohler, "Cantilever spring constant calibration using laser Doppler vibrometry," *Review of Scientific Instruments,* vol. 78, p. 063701, 2007.

[155] R. Proksch, T. Schäffer, J. Cleveland, R. Callahan, and M. Viani, "Finite optical spot size and position corrections in thermal spring constant calibration," *Nanotechnology,* vol. 15, p. 1344, 2004.

[156] M. B. Viani, T. E. Schäffer, A. Chand, M. Rief, H. E. Gaub, and P. K. Hansma, "Small cantilevers for force spectroscopy of single molecules," *Journal of Applied Physics,* vol. 86, p. 2258, 1999.

[157] H. B. Callen and R. F. Greene, "On a theorem of irreversible thermodynamics," *Physical Review,* vol. 86, pp. 702-710, 1952.

[158] R. F. Greene and H. B. Callen, "On a theorem of irreversible thermodynamics. II," *Physical Review,* vol. 88, pp. 1387-1391, 1952.

[159] J. L. Hutter and J. Bechhoefer, "Calibration of atomic-force microscope tips," *Review of Scientific Instruments,* vol. 64, pp. 1868-1873, 1993.

[160] H. J. Butt and M. Jaschke, "Calculation of thermal noise in atomic force microscopy," *Nanotechnology,* vol. 6, p. 1, 1995.

[161] A. Cleland and M. Roukes, "Noise processes in nanomechanical resonators," *Journal of Applied Physics,* vol. 92, pp. 2758-2769, 2002.

[162] D. Walters, J. Cleveland, N. Thomson, P. Hansma, M. Wendman, G. Gurley, *et al.*, "Short cantilevers for atomic force microscopy," *Review of Scientific Instruments,* vol. 67, pp. 3583-3590, 1996.

[163] B. Ohler, "Practical advice on the determination of cantilever spring constants," *Veeco Instruments Inc.,* 2007.

[164] O. Pfeiffer, C. Loppacher, C. Wattinger, M. Bammerlin, U. Gysin, M. Guggisberg, *et al.*, "Using higher flexural modes in non-contact force microscopy," *Applied Surface Science,* vol. 157, pp. 337-342, 2000.

[165] M. Bauer, F. Ritter, and G. Siegmund, "High-precision laser vibrometers based on digital Doppler signal processing," in *Fifth International Conference on Vibration Measurements by Laser Techniques*, 2002, pp. 50-61.

[166] H-E. Albrecht, *Laser Doppler and phase Doppler measurement techniques*: Springer Science & Business Media, 2003.

[167] J. Czarske and O. Dölle, "Quadrature demodulation technique used in laser Doppler velocimetry," *Electronics Letters,* vol. 34, pp. 547-549, 1998.

[168] "Ultra High Frequency Vibrometer UHF-120 User Manual," P. GmbH, Ed., ed. Germany: Polytec GmbH.

[169] M. Johansmann, G. Siegmund, and M. Pineda, "Targeting the limits of laser Doppler vibrometry," *Proc. IDEMA*, pp. 1-12, 2005.

[170] G. Siegmund, "Sources of measurement error in laser Doppler vibrometers and proposal for unified specifications," in *Eighth International Conference on Vibration Measurements by Laser Techniques: Advances and Applications*, 2008, pp. 70980Y-70980Y-13.

[171] K. Itoh, "Analysis of the phase unwrapping algorithm," *Appl. Opt*, vol. 21, p. 2470, 1982.

[172] U. Buehn and H. Nicklich, "Calibration of laser vibrometer standards according to the standardization project ISO 16063-41," in *Seventh International Conference on Vibration Measurements by Laser Techniques: Advances and Applications*, 2006, pp. 63451F-63451F-9.

[173] L. Yarovoi and G. Siegmund, "The effect of three-wave interference in laser Doppler vibrometry," *Measurement Science and Technology*, vol. 15, p. 2150, 2004.

[174] C. Rembe and A. Draebenstedt, "Additional error sources for microscopic laser Doppler measurements," in *Sixth International Conference on Vibration Measurements by Laser Techniques: Advances and Applications*, 2004, pp. 446-457.

[175] M. W. Sracic and M. S. Allen, "Experimental investigation of the effect of speckle noise on continuous scan laser Doppler vibrometer measurements," in *27th International Modal Analysis Conference (IMAC-XXVII), Orlando, FL, February*, 2009, pp. 9-12.

[176] L. T. Gnecco, *The design of shielded enclosures : cost-effective methods to prevent EMI*. Boston: Newnes, 2000.

[177] "OFV-534 Compact Sensor Head," P. GmbH, Ed., ed. www.polytec.com: Polytec, 2008.

[178] "Vibrometer Controller OFV-5000," Polytec, Ed., ed. Haupstsitz, Germany: Polytec GmbH.

[179] A. J. Kaneria, D. Sharma, and R. Trivedi, "Static Analysis of Electrostatically Actuated Micro Cantilever Beam," *Procedia Engineering*, vol. 51, pp. 776-780, 2013.

[180] "MACOR Data Sheet," in *www.corning.com*, C. I. L. Materials, Ed., ed. Houghton Park, Corning, New York: Corning Incorporated.

[181] S. Chowdhury, M. Ahmadi, and W. Miller, "A closed-form model for the pull-in voltage of electrostatically actuated cantilever beams," *Journal of Micromechanics and Microengineering*, vol. 15, p. 756, 2005.

[182] S. Pamidighantam, R. Puers, K. Baert, and H. A. Tilmans, "Pull-in voltage analysis of electrostatically actuated beam structures with fixed–fixed and fixed–free end conditions," *Journal of Micromechanics and Microengineering,* vol. 12, p. 458, 2002.

[183] O. Bochobza-Degani and Y. Nemirovsky, "Modeling the pull-in parameters of electrostatic actuators with a novel lumped two degrees of freedom pull-in model," *Sensors and Actuators A: Physical,* vol. 97, pp. 569-578, 2002.

[184] J. Gaspar, V. Chu, and J. Conde, "Electrostatic actuation of thin-film microelectromechanical structures," *Journal of Applied Physics,* vol. 93, pp. 10018-10029, 2003.

[185] K. E. Petersen, "Dynamic micromechanics on silicon: techniques and devices," *IEEE Transactions on Electron Devices,* vol. 25, pp. 1241-1250, 1978.

[186] M-W. Kim, Y-H. Song, and J-B. Yoon, "Fast and robust cantilever switch with suppressed bouncing for IC applications," in *2011 IEEE 24th International Conference on Micro Electro Mechanical Systems (MEMS)*, 2011, pp. 1229-1232.

[187] O. Kuter-Arnebeck, A. Labuda, S. Joshi, K. Das, and S. Vengallatore, "Estimating damping in microresonators by measuring thermomechanical noise using laser Doppler vibrometry," *Journal of Micromechanical Systems,* vol. 23, pp. 592-599, 2013.

[188] M. A. Hopcroft, W. D. Nix, and T. W. Kenny, "What is the Young's Modulus of Silicon?," *Journal of Microelectromechanical Systems,* vol. 19, pp. 229-238, 2010.

[189] Y. Touloukian, R. Powell, C. Ho, and P. Klemens, "Thermophysical Properties of Matter-The TPRC Data Series. Volume 1. Thermal Conductivity-Metallic Elements and Alloys," DTIC Document1970.

[190] G. A. Slack, "Thermal conductivity of pure and impure silicon, silicon carbide, and diamond," *Journal of Applied Physics,* vol. 35, pp. 3460-3466, 2004.

[191] H. Ibach, "Thermal expansion of silicon and zinc oxide (I)," *Physica Status Solidi (b),* vol. 31, pp. 625-634, 1969.

[192] H. Ibach, "Thermal expansion of silicon and zinc oxide (II)," *Physica Status Solidi (b),* vol. 33, pp. 257-265, 1969.

[193] M. F. Ashby, "Materials Selection in Mechanical Design. 1999," ed: Pergamon Press, Oxford, 2002.

[194] V. Glazov and A. Pashinkin, "The thermophysical properties (heat capacity and thermal expansion) of single-crystal silicon," *High Temperature,* vol. 39, pp. 413-419, 2001.

[195] L. V. Gurvich and I. Veyts, *Thermodynamic Properties of Individual Substances: Elements and Compounds* vol. 2: CRC Press, 1990.

[196] J. P. Dismukes, L. Ekstrom, E. F. Steigmeier, I. Kudman, and D. S. Beers, "Thermal and Electrical Properties of Heavily Doped Ge-Si Alloys up to 1300°K," *Journal of Applied Physics,* vol. 35, pp. 2899-2907, 1964.

[197] C. Prakash, "Thermal conductivity variation of silicon with temperature," *Microelectronics Reliability,* vol. 18, p. 333, 1978.

[198] C. Swenson, "Recommended values for the thermal expansivity of silicon from 0 to 1000 K," *Journal of Physical and Chemical Reference Data,* vol. 12, pp. 179-182, 1983.

[199] C. Bourgeois, E. Steinsland, N. Blanc, and N. De Rooij, "Design of resonators for the determination of the temperature coefficients of elastic constants of monocrystalline silicon," in *Proceedings of the 1997 IEEE International Frequency Control Symposium, 1997.*, 1997, pp. 791-799.

[200] J. J. Hall, "Electronic effects in the elastic constants of n-type silicon," *Physical Review,* vol. 161, p. 756, 1967.

[201] H. McSkimin, W. Bond, E. Buehler, and G. Teal, "Measurement of the elastic constants of silicon single crystals and their thermal coefficients," *Physical Review,* vol. 83, p. 1080, 1951.

[202] A. D. Stuckes, "The thermal conductivity of germanium, silicon and indium arsenide from 40° C to 425° C," *Philosophical Magazine,* vol. 5, pp. 84-99, 1960.

[203] W. Fulkerson, J. Moore, R. Williams, R. Graves, and D. McElroy, "Thermal conductivity, electrical resistivity, and Seebeck coefficient of Silicon from 100 to 1300 K," *Physical Review,* vol. 167, p. 765, 1968.

[204] E. Yamasue, M. Susa, H. Fukuyama, and K. Nagata, "Thermal conductivities of silicon and germanium in solid and liquid states measured by non-stationary hot wire method with silica coated probe," *Journal of Crystal Growth,* vol. 234, pp. 121-131, 2002.

[205] R. G. Morris and J. G. Hust, "Thermal conductivity measurements of silicon from 30 to 425 C," *Physical Review,* vol. 124, p. 1426, 1961.

[206] H. Shanks, P. Maycock, P. Sidles, and G. Danielson, "Thermal conductivity of silicon from 300 to 1400 K," *Physical Review,* vol. 130, p. 1743, 1963.

[207] B. Abeles, D. Beers, G. Cody, and J. Dismukes, "Thermal conductivity of Ge-Si alloys at high temperatures," *Physical Review,* vol. 125, p. 44, 1962.

[208] S. I. Novikova, "Thermal expansion of solids," *Moscow Izdatel Nauka,* vol. 1, 1974.

[209] K. Lyon, G. Salinger, C. Swenson, and G. White, "Linear thermal expansion measurements on silicon from 6 to 340 K," *Journal of Applied Physics,* vol. 48, pp. 865-868, 1977.

[210] M. E. Fine, "Cp–Cv in Silicon and Germanium," *The Journal of Chemical Physics,* vol. 21, pp. 1427-1427, 1953.

[211] R. Roberts, "Thermal expansion reference data: silicon 300-850 K," *Journal of Physics D: Applied Physics,* vol. 14, p. L163, 1981.

[212] (May, 2015). *NIST/SEMATECH e-Handbook of Statistical Methods*. Available: http://www.itl.nist.gov/div898/handbook/

[213] S. Joshi, "Measurement and analysis of damping in microresonators," Masters of Engineering, Mechanical Engineering, McGill University, 2013.

[214] Y. Levin, "Internal thermal noise in the LIGO test masses: A direct approach," *Physical Review D,* vol. 57, p. 659, 1998.

[215] K. Das, "Synthesis and characterization of nanostructured thin films for microsystems," PhD, Mechanical Engineering, McGill University, 2012.

[216] M. S. Bartlett, "Smoothing periodograms from time series with continuous spectra," *Nature,* vol. 161, pp. 686-687, 1948.

[217] P. D. Welch, "The use of fast Fourier transform for the estimation of power spectra: A method based on time averaging over short, modified periodograms," *IEEE Transactions on Audio and Electroacoustics,* vol. 15, pp. 70-73, 1967.

[218] A. Labuda, J. R. Bates, and P. H. Grütter, "The noise of coated cantilevers," *Nanotechnology,* vol. 23, p. 025503, 2012.

[219] J. E. Sader, B. D. Hughes, J. A. Sanelli, and E. J. Bieske, "Effect of multiplicative noise on least-squares parameter estimation with applications to the atomic force microscope," *Review of Scientific Instruments,* vol. 83, p. 055106, 2012.

[220] P. Daniell, "Discussion on symposium on autocorrelation in time series," *Supplement to Journal of the Royal Statistical Society,* vol. 8, pp. 88-90, 1946.

[221] W. H. Press, *Numerical Recipes: The Art of Scientific Computing*. Cambridge [Cambridgeshire]; New York: Cambridge University Press, 1986.

[222] S. F. Nørrelykke and H. Flyvbjerg, "Power spectrum analysis with least-squares fitting: Amplitude bias and its elimination, with application to optical tweezers and atomic force microscope cantilevers," *Review of Scientific Instruments,* vol. 81, p. 075103, 2010.

[223] P. R. Bevington, *Data reduction and error analysis for the physical sciences*. New York: McGraw-Hill, 1969.

[224] J. E. Sader, J. Sanelli, B. D. Hughes, J. P. Monty, and E. J. Bieske, "Distortion in the thermal noise spectrum and quality factor of nanomechanical devices due to finite frequency resolution with applications to the atomic force microscope," *Review of Scientific Instruments,* vol. 82, p. 095104, 2011.

[225] P.-L. Yu, T. P. Purdy, G. D. Cole, and C. A. Regal, "New directions in high-q optomechanical membrane resonators," in *CLEO: Science and Innovations,* 2013, p. CW3F. 8.

[226] V. Adiga, B. Ilic, R. Barton, I. Wilson-Rae, H. Craighead, and J. Parpia, "Modal dependence of dissipation in silicon nitride drum resonators," *Applied Physics Letters,* vol. 99, p. 253103, 2011.

[227] S. Chakram, Y. Patil, L. Chang, and M. Vengalattore, "Dissipation in ultrahigh quality factor SiN membrane resonators," *Physical Review Letters,* vol. 112, p. 127201, 2014.

[228] A. Biswas, T. Weller, and L. P. Katehi, "Stress determination of micromembranes using laser vibrometry," *Review of Scientific Instruments,* vol. 67, pp. 1965-1969, 1996.

[229] J. Dzuba, G. Vanko, M. Držík, I. Rýger, M. Vallo, V. Kutiš, *et al.*, "Stress investigation of the AlGaN/GaN micromachined circular diaphragms of a pressure sensor," *Journal of Micromechanics and Microengineering,* vol. 25, p. 015001, 2015.

[230] D. Friedrich, H. Kaufer, T. Westphal, K. Yamamoto, A. Sawadsky, F. Y. Khalili, *et al.*, "Laser interferometry with translucent and absorbing mechanical oscillators," *New Journal of Physics,* vol. 13, p. 093017, 2011.

[231] C. M. Hernandez, T. W. Murray, and S. Krishnaswamy, "Photoacoustic characterization of the mechanical properties of thin films," *Applied Physics Letters,* vol. 80, pp. 691-693, 2002.

[232] S. Ma, S. Wang, F. Iacopi, and H. Huang, "A resonant method for determining the residual stress and elastic modulus of a thin film," *Applied Physics Letters,* vol. 103, p. 031603, 2013.

[233] M. A. Maden, A. Jagota, S. Mazur, and R. J. Farris, "Vibrational Technique for Stress Measurement in Films: I, Ideal Membrane Behavior," *Journal of the American Ceramic Society,* vol. 77, pp. 625-635, 1994.

[234] L. Villanueva, B. Amato, T. Larsen, and S. Schmid, "Interface losses in multimaterial resonators," in *2014 IEEE 27th International Conference on Micro Electro Mechanical Systems (MEMS),* 2014, pp. 632-635.

[235] D. Wilson, C. Regal, S. Papp, and H. Kimble, "Cavity optomechanics with stoichiometric SiN films," *Physical Review Letters,* vol. 103, p. 207204, 2009.

[236] I. Structure Probe. (May 6th). *Silicon Membrane Window Grids for TEM*.

[237] A. W. Leissa, "Vibration of Plates," NASA, Ed., ed. Washington DC: NASA, 1969, p. 362.

[238] B. M. Zwickl, *Progress Toward Observation of Radiation Pressure Shot Noise*: YALE UNIVERSITY, 2012.

[239] E. A. Avallone, T. Baumeister, and A. Sadegh, "Marks' Standard Handbook For Mechanical Engineers (Standard Handbook for Mechanical Engineers)," 2006.

[240] R. Waitz, S. Nößner, M. Hertkorn, O. Schecker, and E. Scheer, "Mode shape and dispersion relation of bending waves in thin silicon membranes," *Physical Review B,* vol. 85, p. 035324, 2012.

[241] Q. K. Tong, M. A. Maden, A. Jagota, and R. J. Farris, "Vibrational Technique for Stress Measurement in Films: II, Extensions and Complicating Effects," *Journal of the American Ceramic Society,* vol. 77, pp. 636-648, 1994.

[242] L. E. Kinsler and A. R. Frey, *Fundamentals of Acoustics*. New York: Wiley, 1962.